HOLLOW FISSION FRAGMENT TRACKS IN FLUORAPATITE

by

Weixing Li

A dissertation submitted in partial fulfillment
of the requirements for the degree of
Doctor of Philosophy
(Material Science and Engineering)
in The University of Michigan
2010

Doctoral Committee:

Professor Rodney C. Ewing, Co-Chair
Professor Lumin Wang, Co-Chair
Associate Professor Wei Lu
Assistant Professor Anton Van der Ven

DEDICATION

To my wife, Lingxia Liang and my son, Hanlin Li

ACKNOWLEDGEMENTS

I would like to express my gratitude to my advisors, Professor Lumin Wang and Professor Rodney C. Ewing, for giving the chance to study with them at the University of Michigan. I have learnt a lot from them to be a good researcher and I have been really enjoying the process to explore the fields unknown, which are full of fun and surprises. I am thankful for their expertise and insights in the fields of radiation effects and microstructural characterization, and their support and patience, and their valuable comments during the entire efforts with the research. This research would not have been possible without their guidance, support and encouragement. I would also like to thank the committee members Professor Wei Lu and Professor Anton Van der Ven for reading my dissertation and offering valuable comments.

I would like to thank Dr. Kai Sun and Dr. Sha Zhu for teaching me all the TEM experiments and sample preparation, passing on to me their expertise in materials nano-structure and composition characterization. The assistance of Dr. Christina Trautmann at GSI Helmholtz Centre for Heavy Ion Research, Germany, Dr. Vladimir A. Skuratov at Joint institute for nuclear Research, Russia, and Dr. Maik Lang in the swift-ion-irradiation experiments on my samples is greatly appreciated. My special thanks go to Edward Ryan, Peter M. Baldo, Marquis A. Kirk and Amelia. Liu at HVEM (IVEM)-Tandem Facility at Argonne National Laboratory for the support during the ion

beam irradiation experiments. I am also grateful to the insightful comments and intense discussion on the structure and annealing behaviors of tracks in apatite from Dr. Christina Trautmann, Dr. Maik Lang, Dr. Kai Sun, Professor Kundar Li, Dr. Qiangmin Wei and Professor Jie Lian.

I would also like to thank my colleagues and friends, Professor Haiyan Xiao, Professor Xia Xiang, Professor Rongsheng Zhou, Professor Yanbin Chen, Dr. Haiping Sun, Dr. Zhijie Jiao, Dr. Jiaming Zhang, Dr. Tianhua Ding, Alex Perez-Bergquist, Por Pavenayotin, Michaela Eddy and Pantip Ampornrat, Liang Chen, Efrain Hernandez and Jon Wierschke. I appreciate their friendship and support during this period.

I thank my parents for teaching me the value of hard work, for their encouragement and support. Finally, I would like to express my greatest appreciation to my wife, Lingxia. Without her love and willingness to let me push myself in work, I would not have made it through.

TABLE OF CONTENTS

LIST OF FIGURES

LIST OF TABLES

CHAPTER I

INTRODUCTION

1.1. Fission tracks

Fission tracks are damaged trails created by a pair of highly energetic spontaneous fission fragments of heavy elements, mainly ^{238}U impurities embedded in the mineral. Artificial fission of ^{235}U induced by thermal neutrons can also produce similar tracks. A typical fission track in fluorapatite is only 5~10 nm in diameter but can be as long as 16~21 μm. In addition to spontaneous fission tracks created in nature and neutron-induced fission tracks, a variety of highly energetic nuclear particles are used in laboratories to produce parallel tracks in solids, which are usually called swift ion tracks. The latent (or unetched) tracks can be directly observed under the Transmission Electron Microscope (TEM) (Figure1.1A). However, due to the orientation of the track and the limit of the sample size, the visible portion of a track is usually less than 1 μm long. In contrast, after chemical etching to enlarge fission tracks to several μm in width, the whole etchable length (~16 μm) of fission tracks can be seen under a conventional optical microscope (Figure1.1B) [1].

Etched fission tracks have been widely used in age-dating of minerals. Fission tracks embedded the mineral are believed to shrink gradually over a relatively low temperature range (90~140 ^{o}C) at a geological timescale of millions of years. Therefore,

the average lengths of the tracks can be used to infer the thermal history of the mineral. However, the models of fission track annealing have simply fitted curves to data without any considerations of physical mechanism of annealing because there are no systematic studies on the structure of tracks and the annealing behavior of a track at the atomic scale. The structural information of fission tracks is lost due to the chemical etching. Although annealing studies of latent tracks at the atomic scale or nanoscale provide the basis for an improved understanding of the fading of etched tracks, only a very limited number of TEM investigations have been conducted up to now [2-3]. This dissertation is focused on the TEM investigations of the internal structure and annealing behavior and corresponding annealing mechanisms of latent fission tracks in fluorapatite.

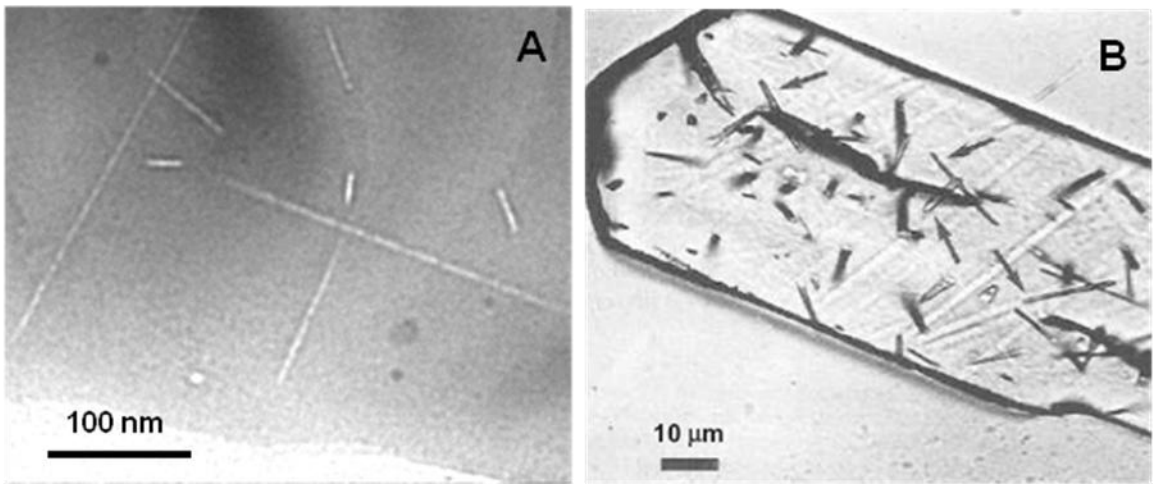

Figure 1.1 Revelation of fission tracks. (A) Latent fission tracks in fluorapatite can be directly observed under TEM. (B) The entire length of etched fission tracks can be seen under conventional optical microscope (B is modified from the Figure 10 in Ref. [1]).

1.1.1. Nature of fission

Fission is a process during which a heavy, unstable nucleus splits into a pair of fragments that represent most of the original nuclear mass. This reaction takes place both spontaneously in nature and artificially during bombardment by neutrons and other high-energy particles or γ-rays. Each reaction is accompanied by the release of a few neutrons and ~210 MeV of energy, of which the majority (~170 MeV on average) is the kinetic energy of the fission fragments. As a result of this energetic disintegration, the fission fragments with massive positive charges are propelled from the reaction site in opposite directions. If the nucleus is located within a dielectric solid, the reaction will create a damage trail along the trajectories of the two fragments. When ^{238}U spontaneously fissions, the mass is divided slightly asymmetrically in the ratio of 1.4 to 1. Correspondingly the kinetic energies of the two fragments are typically 100 MeV for the lighter fragment and 70 MeV for the heavier one, which consequently has a shorter range. As an example, these energies correspond to a damaged range of ~ 12 μm and ~9 μm in fluorapatite, respectively. However, the etchable length of each track is somewhat shorter than the combined range as there is a small range deficit of up to several micrometers at each end of the track where the damage intensity is not sufficient to produce a continuous etchable track [4-5].

Spontaneous fission occurs in very heavy nuclides that belong to the actinide series of elements. Of those nuclides, ^{232}Th and three U isotopes (^{234}U, ^{235}U and ^{238}U) are the typical candidates that produce a significant number of spontaneous fission tracks in solids. However, in regards to the relative abundances and spontaneous fission half-lives,

^{238}U is the only source of spontaneous tracks in terrestrial materials including natural apatite and zircon. Neutron induced fission of the other major isotope ^{235}U gives marginally lower energies, but the lengths of the etched tracks are not measurably different from those for ^{238}U. A two-order greater track density can be generated in thermal-neutron-induced fission track of ^{235}U (~10^7 tracks/cm^2) while the density for spontaneous tracks (~10^5 tracks/cm^2) is too low to observe under TEM.

1.1.2. Swift- ion irradiations

Swift heavy ion irradiations can be used to simulate the damage from spontaneous fission events in solids. The "swift heavy ions" usually have energies in the range of a few tens of MeV to several GeV. In this research, parallel tracks have been produced by various swift ion irradiations in different target materials, such as zircon and fluorapatite. Swift heavy ions create much longer tracks (*e.g.*, 2.2 GeV Au ions: ~90 μm in fluorapatite) as compared with typical fission fragments (*e.g.*, 100 MeV Xe ions: ~ 10 μm in fluorapatite). The electronic energy loss per unit path length of ions, dE/dx, is determined by the mass and kinetic energy of the projectiles being 16 keV/nm in fluorapatite for 100 MeV Xe ions, and 26 keV/nm for 2.2 GeV Au ions. However, this difference in energy loss per unit of depth does not result in significant differences in the track morphology.

1.1.3. Formation of tracks

The structure and final morphology of radiation induced tracks by fission fragments or swift heavy ions depend on the target material, as well as the energy and mass of the projectile ions. We can assume the usual partition of energy loss processes:

$$(-\frac{dE}{dx})_{total} = (-\frac{dE}{dx})_{electronic} + (-\frac{dE}{dx})_{nuclear} + (-\frac{dE}{dx})_{radiation} \quad (1.1)$$

As shown by a Monte Carlo simulation using the TRIM code (Figure1.2) [6], the electronic stopping power of heavy ion with high energy is significantly greater than other contributions therefore electronic energy loss is the most important consideration. The electronic stopping power of an energetic ion has generally been considered more a property of the projectile than the target. The simple Bethe/Bloch formula is applied to describe the electronic stopping power:

$$(-\frac{dE}{dx})_{electronic} = \frac{4\pi z_{eff}^2 e^4}{m_e v^2} Z n_0 \ln \frac{2 m_e v^2}{\bar{I}}, \quad (1.2)$$

where the symbols have their usual meaning. Note, the targets have mostly been assumed in the TRIM simulation to be amorphous instead of crystalline.

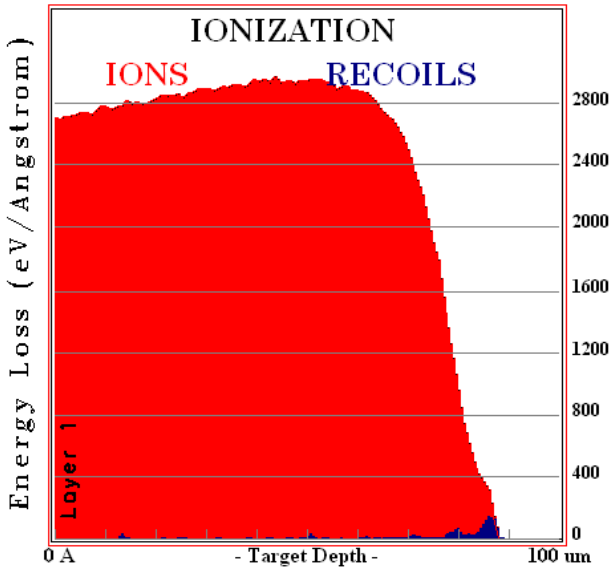

Figure 1.2 The TRIM calculations show the stopping power dependence on target depth of 2.2 GeV Au ions irradiated in fluorapatite. The electronic part (marked with ions) is significantly larger than nuclear collision (recoils) for most of the target depth except the very end [6].

Although there is a general agreement on the deceleration process of the charged fission fragments, the debate has raged concerning the formation of fission track as to which mechanism causes the resultant motion of the lattice atoms that forms and registers the damage zone [1]. The thermal spike model treats the rapid deposition of energy into the lattice as a near-instantaneous heating event [1, 7]. Lattice defects are created during the intense heating process, and the subsequently rapid quench leaves a track of massively disordered material. An alternative theory is the ion explosion model(Figure 1.3) [4, 8], by which the rapidly moving positively charged particle leaves a zone of positively-ionized lattice atoms that are displaced from their original lattice sites as a result of Coulombic repulsion. The stressed region relaxes elastically, creating long-range strains in the surrounding undamaged structure. In a recent paper, Chadderton argued

that both ion explosion and thermal spikes could be responsible to different degrees for track formation and registration depending on the properties of the solid [7].

One should note that radiation can be a remarkably constructive process during fission track formation, which is an intrinsic aspect that is often ignored [7]. The absence of latent fission fragment or heavy swift ions tracks in silicon is due to epitaxial recrystallization: first, there is the growth of the amorphous phase due to a thermal pulse moving radially from the trajectory, followed by a concomitant cooling-wave moving-inward radially for a damage recovery. Thus, no damage remains because of the total recovery in silicon. The low energy electrons generated in the same spike play an important role in this recovery. In contrast, the energy deposition density for 40 MeV C_{60} molecular cluster ion irradiation of silicon is evidently so high that epitaxial recovery is incomplete, and the retreating epitaxial interface between crystalline and amorphous phase is quenched [9]. This is also a type of recovery, probably due to radiation enhanced diffusion caused by the primary low energy δ electrons [10].

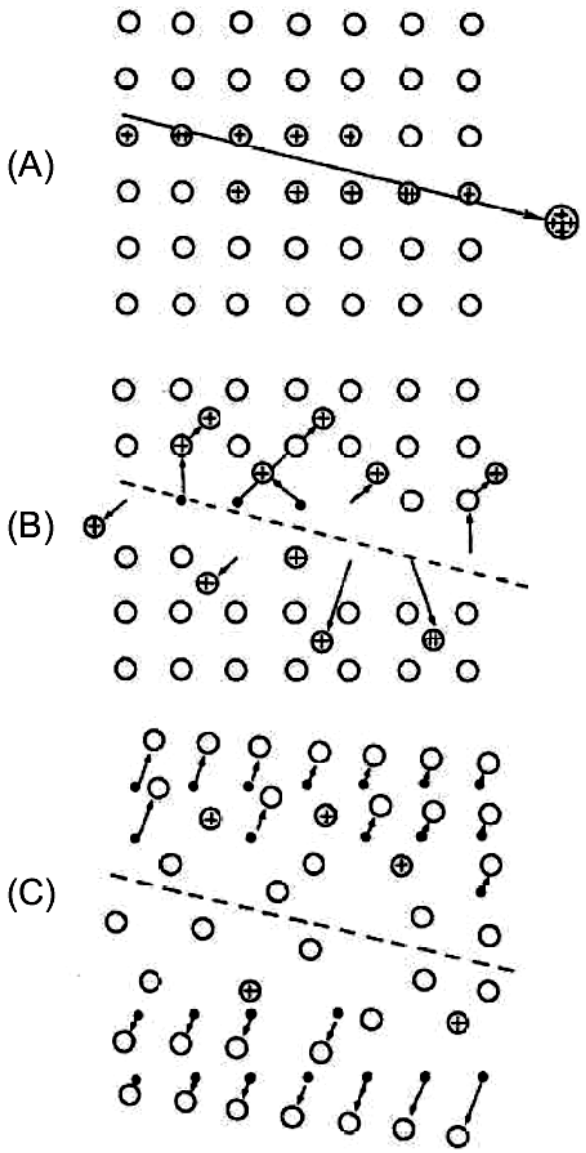

Figure 1.3 Ion explosion spike model (from Fleischer in [8]). (A) The rapidly moving positively-charged particle strips lattice electrons along its trajectory, leaving an array of positively-ionized lattice atoms; (B) the resulting clusters of positive ions are displaced from their original lattice sites as a result of Coulomb repulsion, creating interstitials and vacancies; and (C) the stressed region relaxes elastically, straining the surrounding undamaged lattice.

1.1.4. Fission track dating and modeling

In this part, two methods of fission track dating, *i.e.* track density measurements and track length measurements will be discussed. Empirical annealing models mathematically fitting the laboratory thermal annealing data will be discussed. The difficulties in physical modeling of fission track annealing will be introduced.

The basic principles of fission track age determination are based on that the measured track density induced by spontaneous fission or induced fission in the etched surface directly reflects the concentration of ^{238}U or ^{235}U, respectively. For a given uranium concentration, the spontaneous fission track density will steadily increase through time, provided the tracks remain stable and are therefore quantitatively retained. Therefore, the ratio of ^{238}U and ^{235}U concentration represents the age of the mineral. Once fission tracks have been revealed by etching, the track density or the number of tracks per unit area on the etched surface which is the main parameter measured is representative of geological age. In principle, a radiometric age is given by three parameters, *i.e*., the numbers of parent and daughter nuclides in a mineral, and the decay constant for the parent nuclide. The density of spontaneous fission tracks is directly measured on the polished surface, while that of induced fission tracks is measured on a muscovite external detector attached on the polished (Figure 1.4) [1].

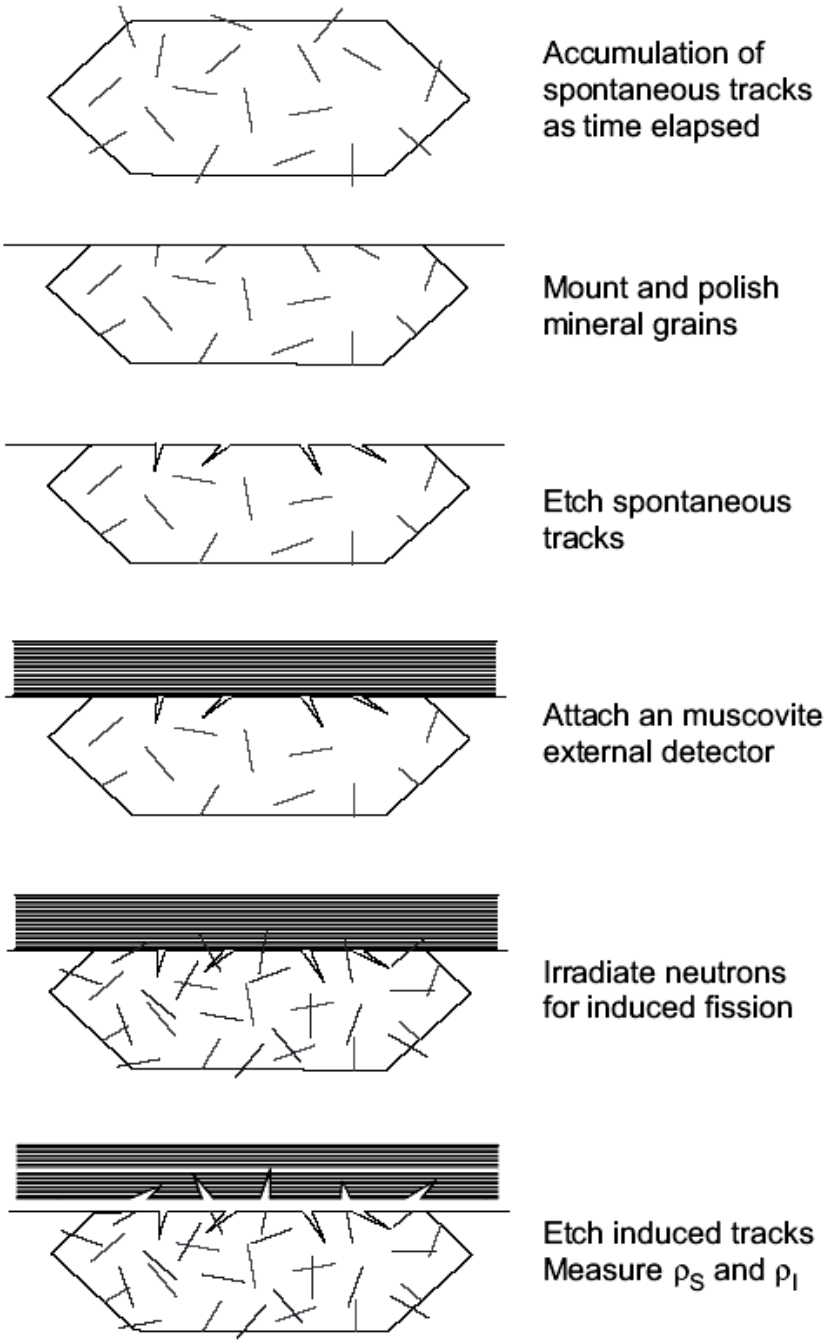

Figure 1.4 Schematic illustration of the experimental steps involved in the external detector method to determine the surface density of etched spontaneous fission tracks ρ_s and surface density of etched induced fission tracks ρ_I (From the Figure 12 in [1]).

The fission track age of unknown sample can be determined by

$$t = \frac{1}{\lambda_D} \ln\left\{1 + \lambda_D \xi \rho_D \left(\frac{\rho_S}{\rho_I}\right) QG\right\}. \tag{1.3}$$

where λ_D is α decay constant of ^{238}U(1.55125×10^{-10} y^{-1}), ξ is the zeta age calibration factor determined empirically by analyzing a set of standard materials of known ages, Q is the integrated factor of registration and observation efficiency of fission tracks, which may be ignorable in the routine analysis, G is the integrated geometry factor of etched surface, is given by inputting the measured data of standard and the reference age t into the equation above. Therefore, the fission track age determination of an unknown sample is based on the measurement of three track densities, *i.e.*, ρ_s, ρ_I and ρ_D, which are the surface density of etched spontaneous fission tracks, the surface density of etched induced fission tracks, and the induced fission track density on U-doped standard glass, respectively.

Parallel to the track density method, the etched track length measurements are intensively used in age-dating of minerals. The implicit assumption in the density measurement method is that the track lengths of spontaneous and induced tracks are the same. The three dimensional distribution of fission event with the crystal is related to the observed track density on a two dimensional surface via the average track length. However, the lengths of spontaneous and induced tracks are never exactly the same due to some shortening of the spontaneous tracks over their lifetime [11]. The application of fission track length studies to the interpretation of fission track ages depends on the three properties of spontaneous fission tracks [12].

1. All the tracks in a specified target, *e.g.* fluorapatite, have a similar initial etchable length (*e.g.*, ~16 μm in fluorapatite), which is somewhat shorter than the combined range (~21 μm in fluorapatite) of two fission fragments in the target due to the inefficiency of the etching process at each end of the track.
2. Tracks become progressively shorter with exposure to elevated temperatures and the final length is mainly controlled by the maximum temperature that each track has experienced.
3. New tracks are continually added to the sample through time so that each one has experienced a different fraction of the total thermal history.

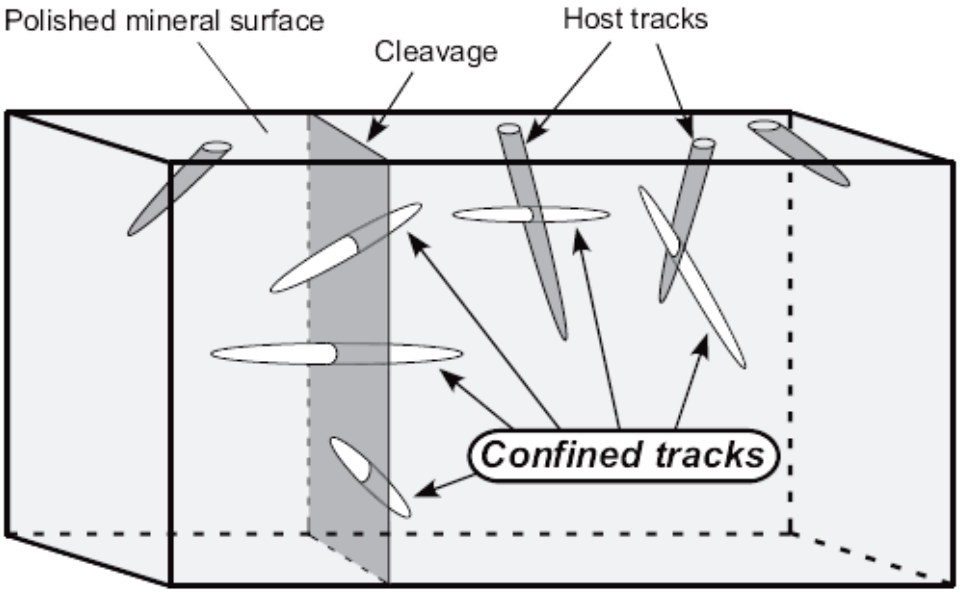

Figure1.5 A schematic illustration of an etched mineral that reveals confined tracks of different dimensions, *i.e.*, tracks-in-cleavage or tracks-in-track [1].

In practice, only the confined tracks, *i.e.* tracks that are located with a crystal and are etched through a host track or cleavage are measured because they exhibit their entire lengths (Figure 1.5) [1]. In contrast, surface-intersecting tracks are randomly truncated at some arbitrary distance along their lengths, making their use in estimating the full etchable length difficult.

Progressive shortening of the confined track length is accompanied by a reduction in the measured track density due to reduced probability of shortened tracks intersecting the polished surface of a grain and thus being exposed to the etchant. The track density increase due to the continued accumulation of spontaneous fissions in the sample should also be considered. Therefore, track length distributions observed in geological samples are seen to be the net result of both track production and track fading processes over geological time.

Despite the complexity in thermally annealing natural samples, it has been demonstrated that the systematic and progressive nature of track length reduction provided an unparalleled opportunity to obtain the thermal history of a sample [13]. Typical crustal geothermal gradients are around 20-30^{o}C/km; therefore, the temperature at 4-5 km depth is in the range of 100-200 ^{o}C if the surface temperatures around 10-20 ^{o}C. Long-term natural annealing of fission tracks from hydrocarbon exploration wells drilled within the Otway basin in southeastern Australia clearly demonstrate a systematic reduction in the mean confined track length and apparent fission track age with increasing temperature [14]. Both the apatite fission track age and mean track length

decrease systematically with depth from at the surface to at depth of ~3.5 km forming a characteristic concave-up profile of apparent apatite age [12, 14](Figure1.6).

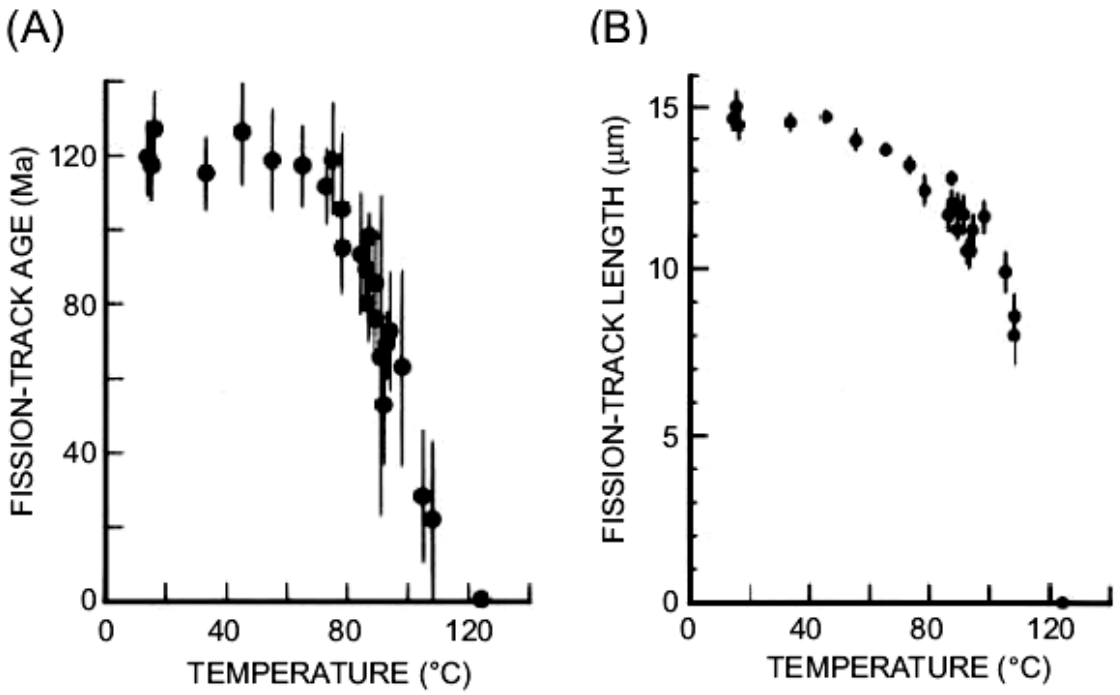

Figure1.6 Long term natural annealing of fission tracks in apatite from Otway, Basin, Australia, for which the geological evolution was well constrained. Both fission track age (A) and length (B) are reduced progressively down to zero in the temperature range due to the increase in geothermal temperature with depth [14].

Numerous efforts have been made in order to quantify the kinetics of apatite fission track annealing on the basis of laboratory experiments in which track length distributions are measured in crystals subjected to controlled thermal histories (i.e., annealing temperature:100-400 ^{o}C; annealing time: up to 500 days) [15-16]. In earlier studies, the rate equation that describes fission track annealing was described by a first order kinetics in the form:

$$\frac{dr}{dt} = -\alpha_0 r \exp(\frac{-E_A}{kT}) \tag{1.4}$$

at a series of temperature (T) and the time (t), where r is the degree of annealing, k Boltzmann's constant, α_0 a constant and E_A the activation energy [1]. In laboratory studies, the etched fission tracks in fluorapatite have been found to be completely annealed after heating at 360 ℃ for one hour (Figure 1.7) [16-18].

In practice, very complex models with several adjustable parameters other than those given in Equation1.4 have been presented in order to fit the curves based on the mathematical features of the thermal heating data, *e.g.*, the widely cited "Laslett et al.(1987) model",

$$g(r) = [\{(1-r^{2.7})/2.7\}^{0.35} - 1]/0.35 = -4.87 + 0.000168T[\ln(t) + 28.12], \tag{1.5}$$

where, $r = l/l_0$ and T and t have their usual meaning) [19]. However, these treatments have been criticized as purely empirical, based upon mathematical features of laboratory results without having a clear physical significance [20]. This is because chemical etching removes not only the disordered region comprising the latent track but also an indeterminate volume of the surrounding crystal. The geometry of etched tracks depends not only on the structure of the latent track, but also the composition and concentration of the etchant, as well as on the chemistry and structure of the apatite [16].

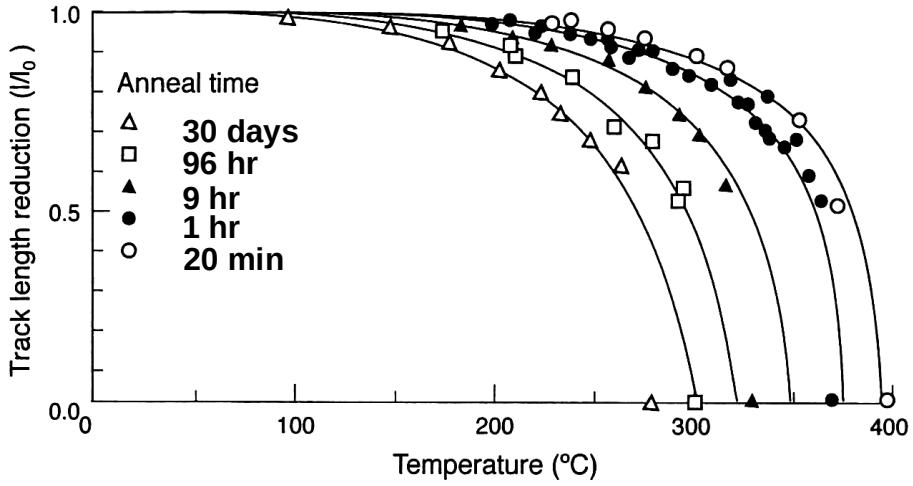

Figure 1.7 Short-term laboratory annealing data for track length in Durango apatite and curves fitted using the fanning Arrhenius model. The fission tracks are totally annealed around 360 ^{o}C for one hour [16-18].

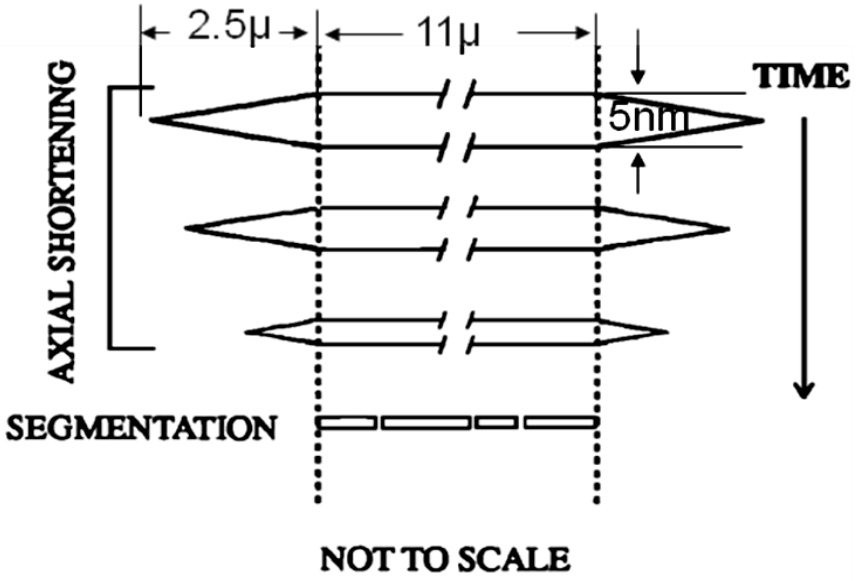

Figure 1.8 Carlson's physical model shows schematic representation of disrupted zone in a latent fission track in apatite. A cylindrical zone of disruption ~ 11 µm long and with a width around 5 nm, is determined by two conical tips, each ~ 2.5 µm in length. When the track axial dimension is shortened to less than 11 µm, the track reduction is accelerated by track segmentation because the track radius shrinks to a radius close zero (Modified from Figure 1 in [20]).

The empirical models and the observations of etched tracks provide some indications of the types of annealing mechanisms. For example, isothermal annealing of etched tracks in fluorapatite shows an initially rapid reduction in length followed by a much slower decrease at longer times [21]. Fleisher *et al.* [4] and Green *et al.* [22]suggest a physical model, by which the track etchability is controlled only by the extent to which the density of damage within the track region is greater than some threshold level. The track shrinks from each end because the damage density is highest in the middle of the track (where the fission occurred) and decreases toward each end. However, the empirical models do not provide significant insight into the fundamental processes that occur during track formation and annealing.

Despite of numerous empirical models, very few physical models are available to describe fission track annealing because of the lack of an atomic-level understanding of the track structure. The fundamental processes involved in the annealing of latent tracks in fluorapatite are still unclear [20]. Carlson postulates a model, probably the only serious physical model, in which the thermal annealing produces reduction of track length initially by defect elimination and subsequently accelerated reduction by segmentation of tracks (Figure 1.8) [20]. The track reduction is assumed to be dominated by initial axial shortening and subsequently accelerated by segmentation of tracks after 0.65 initial track length (*i.e*. 11 μm) [20]. A special geometry is assumed to calculate the track radius and axial shortening when the track length larger than 11μm; the segmentation is assumed to take place only when the track radius is close to zero [20]. However, his model was not based on a knowledge of the atomic structure of the track and an experimental

observation of annealing, but rather was criticized as a simple fit to micro-scale measurements of etched tracks [22-23].

In summary, the physical mechanisms of thermal annealing are still not known because there have been no systematic experiments on the damage structure of fission tracks and thermal annealing behavior at the atomic level. Heat is always believed to anneal radiation damage tracks atom-by-atom [24], however, this annealing process is in fact a speculative in the absence of atomic-scale experimental data. Therefore, as stated by Gleadow *et al*., "Currently, atomic scale approaches remain theoretical, but advances in this field could dramatically improve our understanding of the fundamental processes involved in track annealing in apatite [12]."

1.2. Target materials of ion beams

The properties of the target materials are not simply to influence the electronic stopping power of energetic ions, but more importantly they are the most important factors in determining whether the track can be created in a specific target material and what is the structure of the damage trail.

Whether the track can form or not seems to be related to electrical resistivity of the target material[24]. This observation directly support the ion explosion spike model on track formation [8]. If electronic conduction neutralizes the positive core before ions have time to be displaced to new sites, those displacements will be quenched. Tracks are found in dielectric substances, but not in metals or good semiconductors. That indicates

the correlation of track formation with electrical conductivity. In metals, electrons promptly move to neutralize the charge; in semiconductors, the charge can dissipate directly because it is equivalent to an array of positive current carriers (or holes), which are mobile. The tracks can form with very high resistivity (10^6-10^8 ohm/cm) in polymers and other insulators.

There is a quantity called the stress ratio that correlates well with the ionization threshold, below which there is no sufficient energy locally to induce atomic disordering. The stress ratio represents, for a given ionization, the electrostatic forces tending to displace atoms divided into the bonding forces tending to hold atoms in place [8]. Tracks should form most easily in materials of low mechanical strength, low dielectric constant, and close interatomic spacing [8]. Zircon has a much higher registration threshold than phosphate, and plastics; correspondingly the average stress ratio is much higher in zircon (1.4) than that in phosphate (0.5) and that in plastics (0.01) [24].

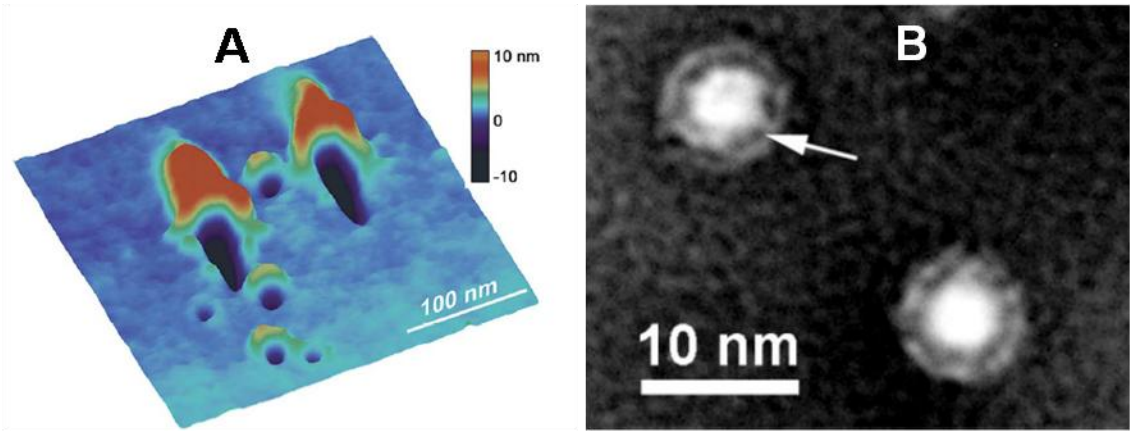

Figure1.9 A, Scanning force microscopy image of tracks induced by 11.1 MeV/u Bi bombarding a PMMA film at 0^o, 45^o and 79^o to the surface normal clearly shows free volume in the track cores [25]. B, The free volume of single ion tracks in PET (polymer) is hard to be observed in an overfocused objective lens condition under TEM [26].

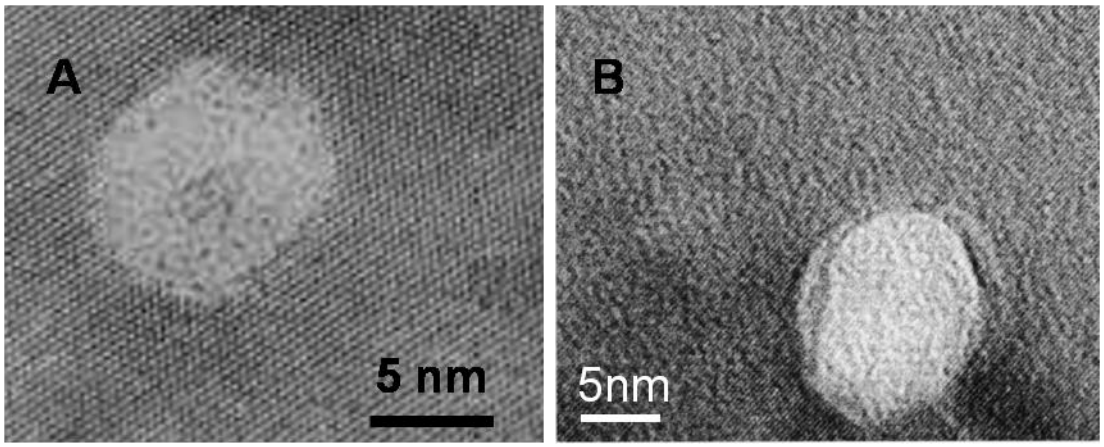

Figure1.10 A, High resolution TEM (HRTEM) image showing an amorphous track induced by Pb ion mica [27]. B, HRTEM image shows the core region of 30 MeV C_{60} cluster on fluorapatite is covered by amorphous matter and the hollow nature is hard to determine, although bubble-like features can be found in low magnification TEM images (not shown) [28].

1.2.1. Effects of target materials

The latent track structure formed by highly energetic charged particles depends on the target material. In volatile-rich polymers, a free volume is believed to form under high energy ion irradiation(Figure 1.9A) [29-30]. The escaping gas molecules result in the formation of a trail of micro-bubbles along the particle trajectory. However, the presence of these micro-voids could not be confirmed by TEM because the material damages rapidly under the electron beam(Figure 1.9B) [29-30]. Latent fission tracks in oxides and more complicated ceramics are commonly considered to be amorphous domains in a crystalline matrix, with a sharp amorphous-crystalline domain boundary (Figure 1.10A) [5, 27, 31]. However, the tracks caused by the heavy ion irradiation of ceramics with volatile-rich elements, like CaF_2 and fluorapatite ($Ca_{10}(PO_4)_6F_2$), have

provided evidence of the formation of a void-like structure [28, 32]. Again, the hollow structure of these tracks in volatile-rich solids is hard to confirm by TEM because of the simultaneous damage from the electron beam during examination (Figure 1.10B) [28].

It should be mentioned that the formation of bubble-like structure seems to be consistent with the stress ratio criterion. The volatile-rich materials, such as polymers and fluorapatite, have weaker bonding forces (*i.e.*, stress ratio) to hold atoms in place and tend to decompose during the energy deposition of energetic ions. In addition, the mass loss or the release of volatile gases during the process of track formation may lead to the formation of low density of track cores.

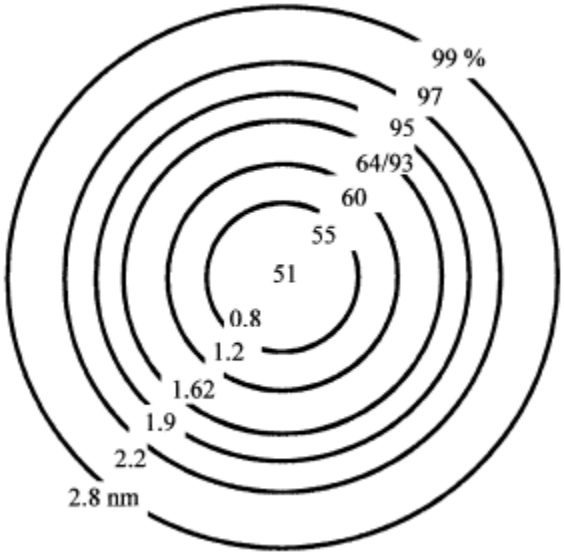

Figure1.11 The SAXS simulated residual electron density (percent of the matrix electron density) in the most probable track versus the radial distance (in nm) from the track center. The low density core region is thought to be created by irradiation induced decomposition. The release of fluorine gas results in the free volume and Li residual within the track core [33].

1.2.2. Radiation-induced decomposition

The formation of a low density core in polymer or volatile-rich solids (*e.g.*, CaF_2, LiF and fluorapatite) may result from the radiation-induced decomposition of these materials and the subsequent loss of volatile elements along the fission track due to the highly ionizing energy deposition during the track formation [34-36]. Small-angle X-ray scattering studies show that continuous density decreases of 50% within 98 μm long and 3.2 nm wide cylindrical ion damage trails, latent ion tracks, created in a LiF platelet by 2.31 GeV Pb ions (Figure 1.11) [33]. The SAXS-derived porous structure of the track core is attributed mainly to radiolytic decomposition of the crystal into Li atoms and fluorine molecules, and subsequent transport and release of the fluorine gas through the low-density tracks [33]. However, the detailed internal structure of low density core and the manner that the atoms within the core are linked are still unknown. The mass loss due to radiation-induced decomposition has also been reported in polymer [37] and CaF_2 [38] either by SAXS or TEM method.

The concept of mass loss resulting from radiation-induced decomposition during the track formation process seems have not been widely accepted by the swift ion community. However the terms like “low density core”, “void-like structure” or “free volume” have been carefully chosen to describe the structure of tracks in polymer and volatile-rich materials [28, 39]. The plastic deformation instead of mass loss due to radiation decomposition has been believed to form the simulated low density core and high density shell structure in 1.43 GeV Xe irradiated amorphous SiO_2 by SAXS analysis(Figure 1.12) [40]. For volatile-rich materials(e.g., LiF and CaF_2), although the

energy deposition causes the separation and aggregation of F centers, vacancy and metal colloid clusters, the release of volatile elements has not been widely accepted [41-42]. Through SAXS studies, the core regions of LiF tracks are believed to be the defects of complex aggregates such as small Li colloids, and fluorine and vacancy clusters [41]. The intermittent faceted structures aligned along the Bi ion trajectories in the CaF_2 matrix under TEM are attributed to faceted anion voids equivalent to Ca colloids (Figure 1.13) [42]. However, the faceted structures are also thought to be F_2 gas filled bubbles [43].

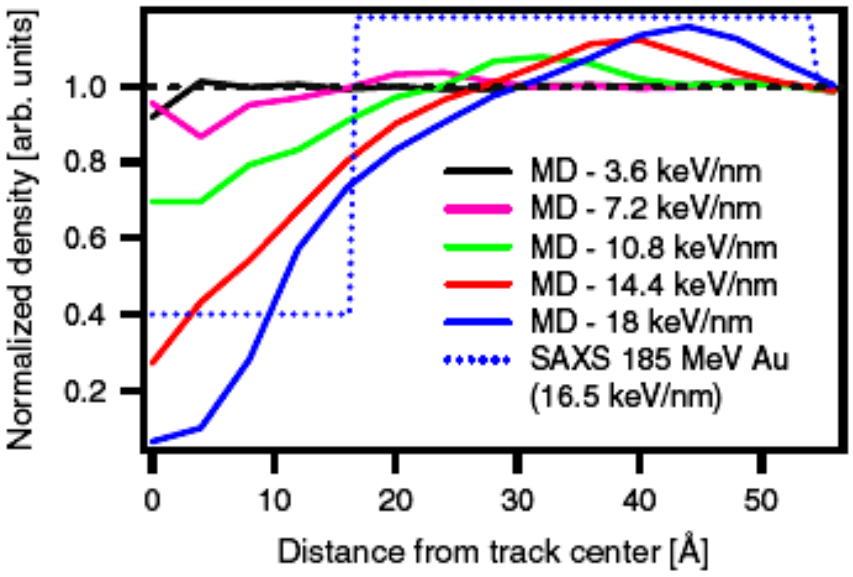

Figure 1.12 Radial density profiles obtained from MD simulations from swift ions irradiated SiO_2. The dashed line denotes the density of unirradiated material. The dotted line shows for comparison a density profile extracted from SAXS measurements of 185 MeV Au irradiation [40]. Note that instead of decreases, the total number of electrons (or mass) in both core and shell regions after irradiation increases 13%.

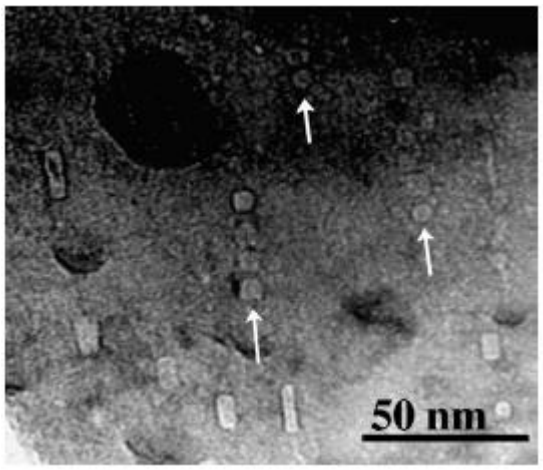

Figure1.13 Transmission electron micrograph of CaF_2 irradiated with 11.2 MeV/u ^{209}Bi ions. The rectangular structure is believed to be Ca colloids [42].

It is well known that electron beam irradiation can induce the decomposition of volatile-rich material due to the electronic energy deposition. EELS and diffraction studies showed that the decomposition of MgF_2 under electron beam irradiation results in formation of elemental metallic Mg and subsequently MgO (Figure 1.14) [44]. The oxidation of Mg is probably because of relatively large amount of water in the vacuum system [44]. The loss of fluorine as volatile F_2 is due to an ionization interaction between the beam electrons and the impinging electrons of the compound [44]. Cameron and Wang *et al.* performed electron irradiation experiments on fluorapatite and observed the formation of newly formed phase CaO (Figure 1.15) [45]. The growth and gradual coalescence of two small bubbles into a larger one under electron irradiation on fluorapatite has been also observed under TEM [35], which is direct evidence to show the decomposition of fluorapatite under electron irradiation.

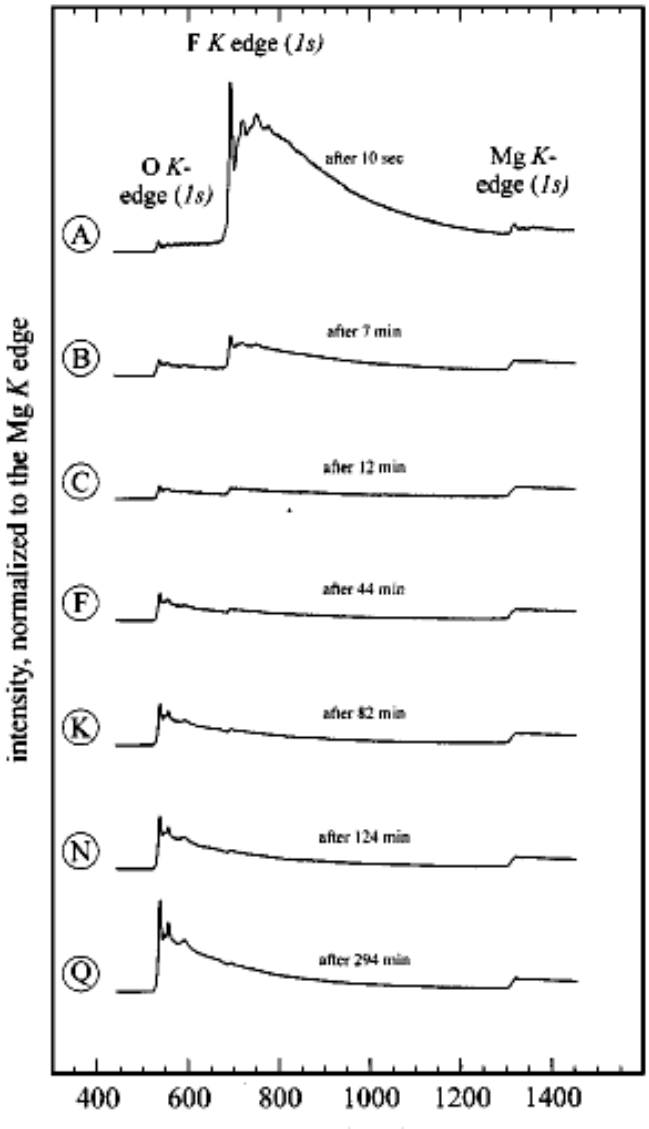

Figure1.14 EELS analysis shows that K edge of O, F, and Mg from the MgF_2 sample at different electron irradiation time. The spectra are normalized to the Mg K edge and shifted along the intensity axis (dispersion 1 eV/channel). The loss of fluorine due to the electron induced decomposition is not simultaneous with the absorption of oxygen [44].

The possible decomposition of fluoraptite by high energetic ions deposition during track formation is different from that during electron beam irradiation in many aspects, but the main energy deposition for the two processes are all from the electronic part. Therefore, the electron beam induced decomposition or mass loss can give very

important information during the track formation. In contrast to electron beam induced case, the decomposition of fluoraptite is more likely to occur during the high-energy deposition process of fission fragments where the typical stopping power is up to several keV/Å. The energy deposition of heavy ion is more focused on a small area during the fission track formation process, and the temperature of the track core is much higher.

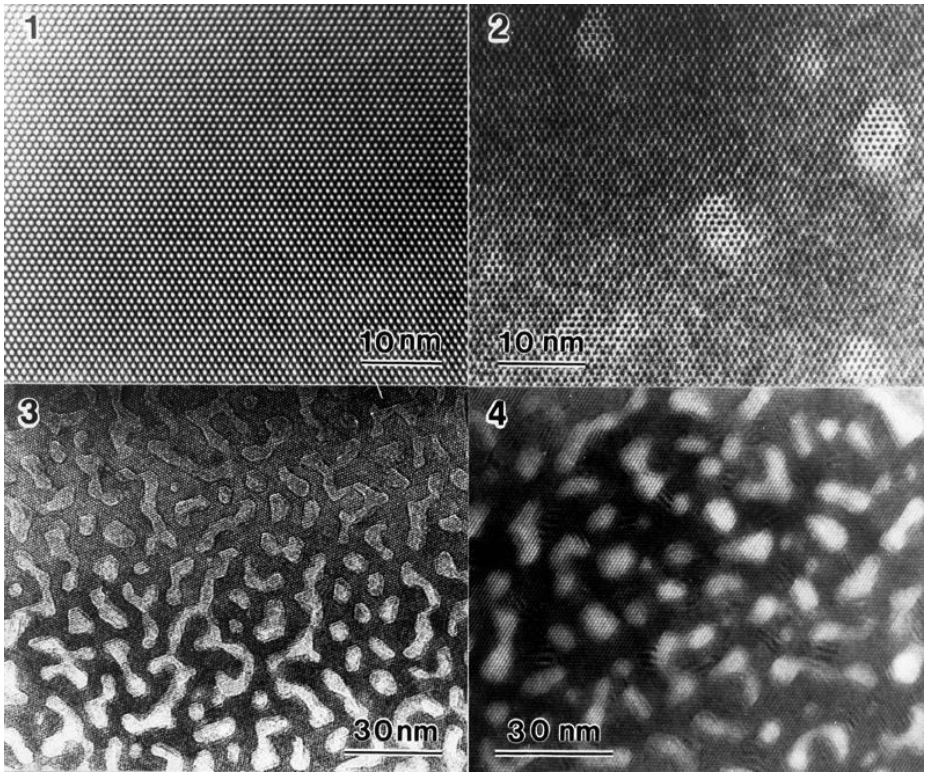

Figure1.15 HRTEM images showing effects of 200keV electron irradiation-induced decomposition on a fluorapatite, (001) single crystal. The Moir é fringes in the last image showing formation of a newly phase, which has been confirmed to be CaO by diffraction pattern [45].

1.2.3. Importance of fission tracks in fluorapatite

Apatite is a group of phosphate minerals with an ideal formula of $Ca_5(PO_4)_3(OH, F, Cl)$, *i.e.* hydroxylapatite, fluorapatite and chlorapatite, respectively. The symmetry of apatite is $P6_3/m$ - consequently, it typically forms hexagonal crystals. As shown in Figure 1.16, crystallographically, fluorapatite has PO_4 tetrahedra linked with two Ca polyhedra [46]. Therefore, an open channel formed along [0001] direction in the crystal structure favors transport of diffusing species. By measuring the etched length of fission tracks, it is found that the tracks parallel to [0001] direction are annealed more slowly than those orthogonal to the direction [47]. However, the nano-scale or atomic scale orientation effects of unetched tracks have not been directly observed under TEM. If observed, it would be important to fully understand the crystalline effects of the thermal annealing behavior of fission tracks in different crystallographic orientations [12].

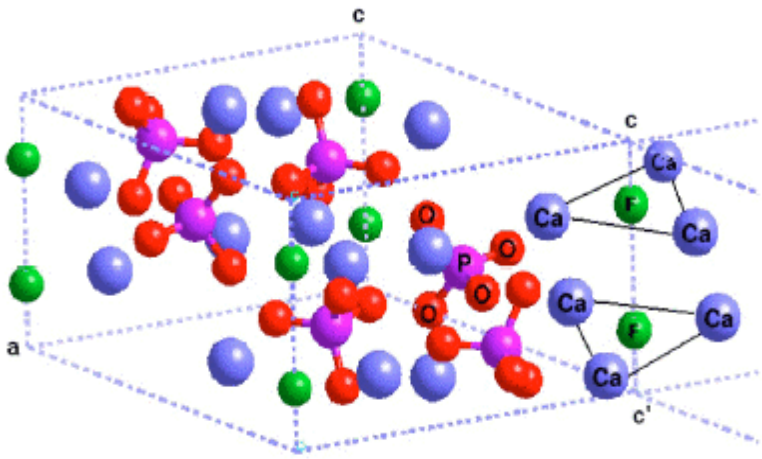

Figure1.16 General view of the fluorapatite structure including calcium triangles [46].

The physical mechanisms for the etched fission track annealing are unknown because there are no systematic studies on the internal structure and the atomic-scale annealing behavior of fission tracks. In this research, TEM instead of optic microscopy has been used as a main tool for directly observing the atomic-scale structure and annealing behavior of latent fission tracks. Fluorapatite is chosen as the studying material to figure out the contributions of chemistry and structure of the target material, *i.e.* apatite, on the internal structure of the tracks, and correspondingly annealing behavior at atomic level.

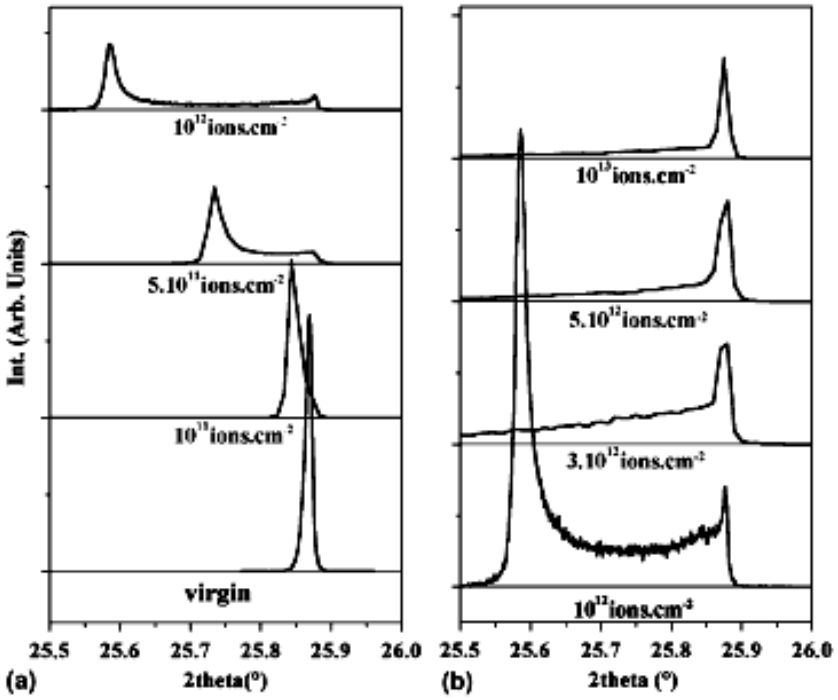

Figure 1.17 (001) single crystal diffraction scans around the (002) line for iodine-irradiated samples. (a) lower fluencies with normalized integrated intensity; (b) larger fluencies with normalized non distorted (002) peak intensity [48].

First, fluorapatite represents more than 70% of all the measurements of the number of fission track age determinations because apatite meets all the criteria for a good mineral for fission track dating [12]. To be widely useful for routine fission track dating a mineral should be: well crystallized, consistently enriched in uranium, significantly larger in grain size (> 60 μm) than fission track dimensions (~16 μm), uniform in its uranium distribution, highly transparent and free of obscuring inclusions and of common occurrence in all major rock groups [12]. All the characteristics of fluorapatite have contributed to its dominance in fission track dating.

Secondly, the nature of the internal structure of tracks in the volatile-rich fluorapatite is unclear and usually thought to be amorphous despite of its importance in fission track dating [12, 31, 48]. Peak broadening has been observed in XRD patterns of powder sample as the increasing dose of iodine ions irradiated fluroapatite, which is attributed to the amorphous track cores (Figure 1.17) [48]. By the classical Poisson's law fitting, the amorphous core (3.6 nm diameter) created by individual heavy ions has been calculated [48]. However, for single crystal diffraction, the damage-related peak surprisingly disappears for the swift ions, iodine-fluences above 10^{12} cm^{-2} leaving a diagram with the only peak from virgin material, which has been explained by the existence of healing process of defects in this material [48]. As mentioned previously, the low magnification TEM image shows bubble-like structure within in the core region of 30 MeV C_{60} clusters irradiated fluorapatite [28]. Unfortunately, the hollow tracks have not been confirmed by HRTEM images because the authors did not control well the electron irradiation-induced damage [28]. In fact, an HRTEM image of fission tracks in apatite has been reported before, but it is hard to tell whether the structure is amorphous

or hollow because the contrast around the core region is nearly saturated [2] (Figure 1.18). This HRTEM image was even thought to be evidence that fission tracks in apatite are amorphous [1].

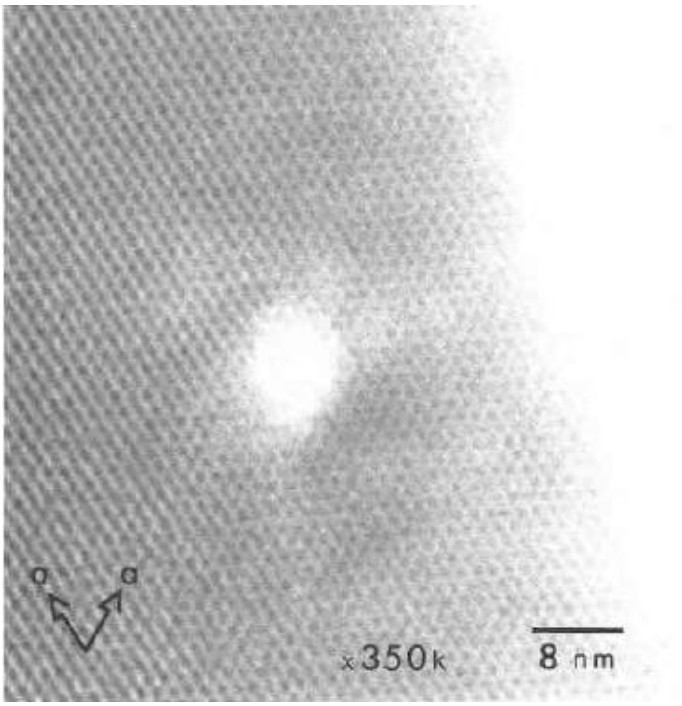

Figure1.18 Hexagonal faceting of a fission track cross section parallel to [0001] of fluorapatite [2]. Note that the contrast within the track is nearly saturated, thus hard to determine the structure of the track.

1.3. Observable characteristics of hollow features

In order to investigate the structure and the annealing behaviors of fission tracks in fluorapatite, the challenging part of this research is to tell if the nanometer scaled tracks embedded in a crystalline matrix are hollow cavities or amorphous domains. Qualitatively, amorphous core within crystalline matrix is significantly different from hollow cores embedded in a crystal. The former has a disordered core with similar

composition and density to the matrix, while the latter has significant mass loss within the core. The much larger density deficiency (or mass loss) within a hollow track would result in a huge internal potential difference between the track and its matrix.

Theoretically, without any annealing treatment this internal potential difference (related to static characters of tracks) can be used to tell whether the track is amorphous or hollow by TEM techniques. In addition, under thermal or radiolytic treatment, the large surface energy and the high surface diffusivity of molecules on the inside surface of hollow features can cause the tracks break up (or Rayleigh instability) and the random motion (or Brownian motion) of track segments. These dynamic characters of hollow features can be also directly observed by *in-situ* TEM techniques.

1.3.1. Stationary characteristics of hollow features

There are two main difficulties in practice in determining the difference between a hollow track and an amorphous track: an individual track is only 5~10 nm in diameter so that the signal from it is too weak to detect; the track will be damaged under electron beam irradiations during TEM investigations.

SAXS and XRD techniques have been applied to simulate the track structure and track morphologies [40]. In the simulation of the geometry of the track core by SAXS and XRD, it is assumed that the core region has a sharp boundary with the matrix, and there are no amorphous components outside the radius of the core counted in the simulation. However, the SAXS and XRD techniques actually collect information from a large region containing both the tracks and the matrix, which are unable to detect the localized features. Any amorphous signals from the matrix might cause significant error

in the simulation. In addition, for SAXS techniques, all the swift ion tracks are assumed to be strictly parallel to the x-ray beam [40] otherwise there are the signals from the track wall instead of totally from the track cores that would influence the simulation. In fact, this assumption is hard to satisfy because the swift ions can never be strictly parallel to each other along the track trajectory of up to several micrometers.

TEM is superior to SAXS and XRD in that it allows to see a feature as small as an atom column under HRTEM. However, the intense electron beam under the HRTEM mode may cause rapid damage of fission track in some materials like polymers and fluoraptite. As shown in Figure 1.10A, the "disordered features" of an amorphous core can be easily observed under HRTEM. However, the hollow core is much harder to "see" because the electron beam irradiation induced damage would cover the track core region during the observations and HRTEM imaging (Figure 1.10B). Therefore, when investigating the materials readily damaged by electron beam, one should control the electron beam damage by keeping the sample at low temperatures or minimizing the electron exposure at a low beam current.

Recently, a number of novel techniques have been developed in TEM/STEM, such as high angle annular dark field imaging (HAADF) and electron energy-loss spectroscopy (EELS). HAADF images (Z-contrast) can be formed by collecting high-angle scattered electrons with an annular detector, in which the image contrast strongly depends on the atomic mass of materials, providing information about structural variations across the sample on at an atomic level. EELS, based on energy analysis of the inelastically scattered electrons, can provide information on the chemical composition at an atomic or sub-nanometer scale. There is thickness information in the energy loss

spectrum because the amount of all the inelastic scattering increases with the specimen thickness, as well as the effective atomic number, *Z*. The combination of atomic resolution HAADF imaging with EELS has already proved extremely valuable for extracting atomic-scale information on the composition and electronic structure of various materials systems. Parallel to stationary characteristics of hollow features, the following is the introduction of the dynamic characteristics of hollow features under thermal or radiolytic treatment.

1.3.2. Rayleigh Instability

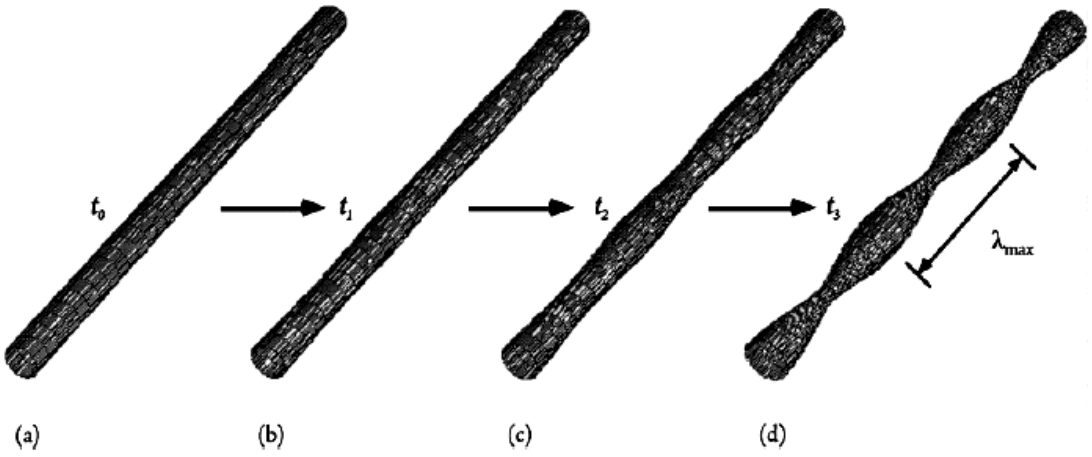

Figure1.19 Schematic illustration of the morphological evolution associated with Rayleigh instabilities. In (a), a segment of an infinitely long cylinder is shown. Infinitesimal perturbations in the radius either shrink (decay) or grow with time. In (b)–(d), the progressive increase in perturbation amplitude is shown. In the idealized situation illustrated, the wavelength that controls the ultimate particle or pore spacing is the kinetically dominant wavelength, λ_{max} [49].

Rayleigh instability is known as spontaneous self-organized disintegration (or segmentation) of a continuous solid rod or a cavity in solid, resulting in decay into a row of spherical droplets via surface or volume diffusion during thermal annealing (Figure 1.19) [49-50]. Note, the driving force for Rayleigh instability to occur is the strong tendency toward lowering the total surface area due to the high diffusivity and the surface energy of hollow tubes or solid cylinders. An infinite cylinder of radius, R, is subjected to periodic perturbation in the radius, of wavelength, λ, and amplitude, α (of initially infinitesimal, α_0), which can be given by a growth/decay law of

$$\alpha = \alpha_0 \exp[\mu t]. \tag{1.6}$$

The amplification factor

$$\mu = \frac{\delta_s D_s \gamma_s \Omega}{R^4 kT}[(\frac{2\pi R}{\lambda})^2 (1 - \frac{2\pi R}{\lambda})^2] \tag{1.7}$$

where δ_s is the surface thickness, D_s the surface diffusivity, γ_s the surface energy, and Ω the atomic volume. If any longitudinal perturbation wavelength is bigger than the circumference ($\lambda > 2\pi R$), the cylinder is unstable, *i. e.*, such perturbation increases in amplitude with time. For a wavelength,

$$\lambda_{\max} = \sqrt{2}(2\pi R) = 8.89R, \tag{1.8}$$

there is a wavelength at which the perturbation reaches a maximum value of μ (or highest growth rate) and dominates the evolution. The morphological change of fission tracks during annealing from cylindrical into spherical shape is energetically favorable

because the total surface area of the track decreases while the total volume remains unchanged.

There has been no Rayleigh instability reported for the amorphous-crystalline (AC) interface, which might be because the product of $D_s\gamma_s$ in AC interface is too small for segmentation to occur. It is known that the origin of the surface free energy is that atoms in the layers nearest the surface are without some of their nearest neighbors [51]. Therefore, the surface energy of AC interface would be much less than that for void-crystalline (VC) interface because the atoms in VC interface have deprived of many of the neighboring atoms [51]. In addition, the VC interface has a much higher surface diffusivity or lower energy barrier than the AC interface because the former has more freedom of mobility due to being rich in vacancies and voids.

From Equation 1.6 and 1.7, it is evident that the decay speed is very sensitive to the track radius. This means the hollow channel with smaller radius will decay much more rapidly. Similarly, due to the non-uniformity of track radius along the trajectory, the portions with smaller radius in the hollow channel will break before those with a larger radius, which causes the irregular segmentation without any periodicity (Figure 1.20) [49].

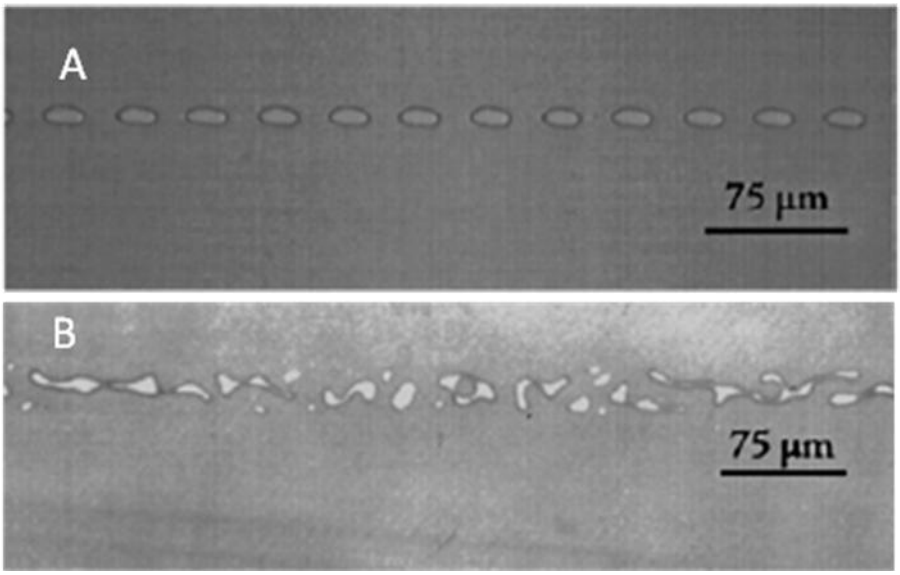

Figure1.20 Optical micrographs of preperturbed pore channels created by ion beam etching along $[1\bar{1}00]$ of sapphire and then annealed at around 1650^{o}C. In (A), the channel did break up in a more normal manner governed by Rayleigh Instability. In (B), the segmentation of pore channel became unstable, and lack of periodicity(Modified from Figure 6 in Ref. [49]).

1.3.3. Brownian motion

Surface diffusion is an important mechanism by which hollow features (bubbles or voids) in the materials move randomly or preferentially along specific directions if there is potential gradient [52]. Molecules of the solid matrix are in constant motion on the inside surface of the bubble. A net displacement of a large number of these surface molecules is manifest as a much smaller displacement of the entire bubble. The motion of these surface molecules can be random or in a particular direction dictated by the direction of a macroscopic potential gradient applied to the matrix. When the motion of surface molecules is random, the resulting bubble motion is also random and is in fact a

form of Brownian motion. When the surface molecules move in a particular direction, the bubbles move in the direction of the potential gradient that is acting on individual surface molecules [52]. It should be added that, the exchange of gas between the bubble and its matrix by volume diffusion mechanism can also cause the random motion of bubbles [52]. The Brownian motion of helium gas bubbles in a vanadium metal has been demonstrated that the bubbles migrate in a random walk manner at $0.55T_m$ by *in-situ* electron microscopy on a hot stage (Figure 1.21) [53]. The bubble A (as marked in Figure 1.21) moves to the right, then returns to the left and finally to migrate upwards [53].

As discussed earlier, in the irregular segmentation of a pore channel, random motion of pore segments will cause the segmentation lack of periodicity (See Figure 1.18 and Ref. [49]. Similarly irregular segmentation has been reported in the *in-situ* TEM observations of thermal-radiolytic annealing of neutron induced fission tracks in apatite(Figure 1.22) [2]. However, the Brownian motion of track segments apparently results from the combined effects of thermal annealing and electron beam annealing. The random motion of track segments has not been related to speculation that the structure might be hollow; on the contrary the TEM observations of the fission track annealing in apatite has been served as atomic evidence of amorphous core restoring to crystalline structure [1]. In fact, the Brownian motion of track segments in this experiment is not good evidence as hollow nature of fission tracks in fluroapatite because the original structure of fission tracks might change much under prolonged electron beam bombardment.

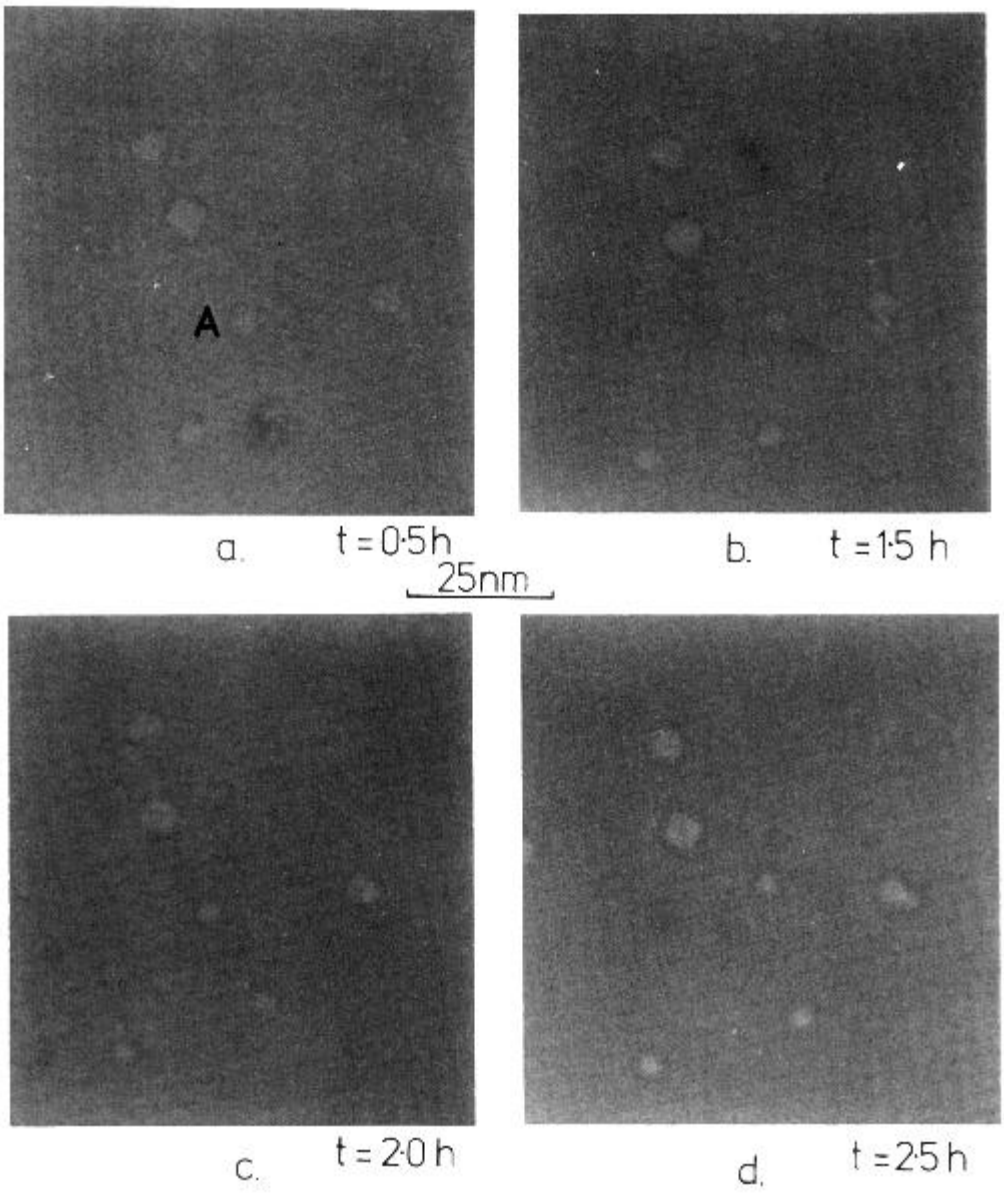

Figure 1.21 Four TEM micrographs from an isothermal hot stage sequence at 950 ℃. Helium bubble A in bcc vanadium has migrated in a different direction in each time interval [53].

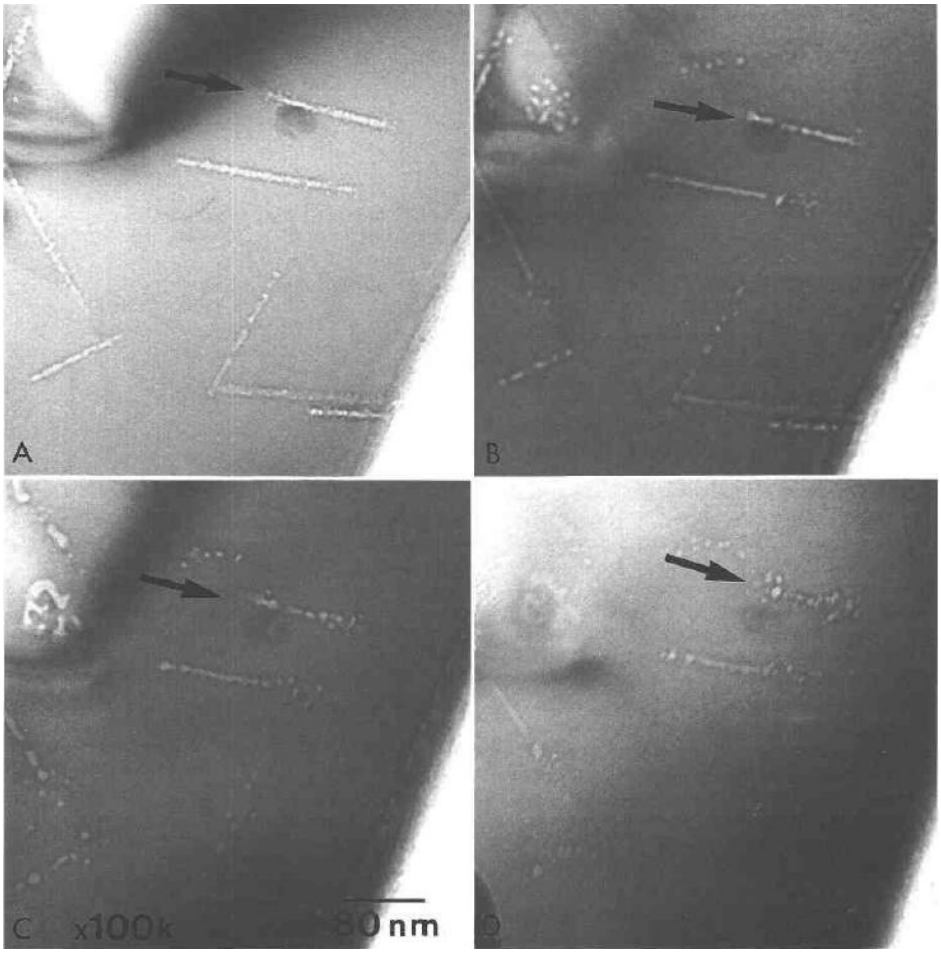

Figure 1.22 Radiolytic-thermal annealing of induced fission tracks in fluorapatite. Beam current density is kept in constant current ~0.35 A/cm^2. (A) Initial sample temperature -175 ^{o}C. (B) After continuous electron-beam exposure and sample heating for 80 min (-74 ^{o}C), (C) After 140 min of electron-beam exposure and heating (-26 ^{o}C). (D) After 180 min of electron-beam exposure and heating (+75 ^{o}C). The Brownian motion of track segments is apparent, which cause the shattering of fission tracks along the trajectory(from Paul et al in [2]).

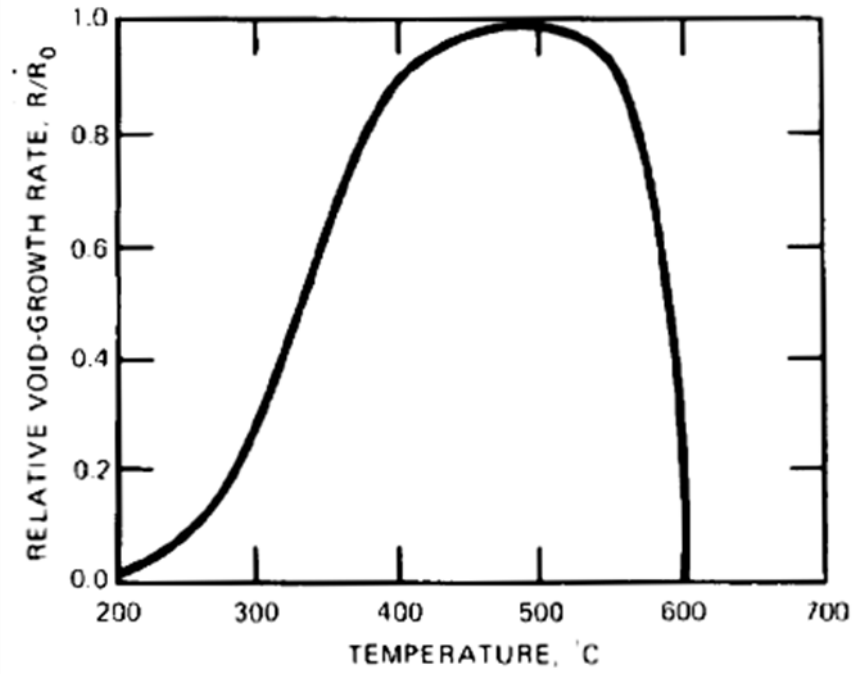

Figure 1.23 Temperature dependence of the void-growth rate in stainless steel under fast-neutron irradiation (After Ref. [52, 54]).

1.3.4. Growth and shrinkage of cavities

The cavity growth in irradiated materials is controlled by diffusion of vacancies and interstitials from the bulk of the solid to the void surface. The growth law is valid for the cavity containing some gas (the bubble) or the gas-free cavity (the void), provided that the internal gas pressure is set equal to zero whenever it appears in the void case. The void-growth law can be expressed as;

$$\dot{R} = \frac{dR}{dt} = \frac{\Omega}{R}\left\{D_V\left[C_V - C_V^{eq}\exp(\frac{2\gamma\Omega}{RkT})\right] - D_i C_i\right\}, \tag{1.9}$$

where R is void radius, C_V^{eq} equilibrium vacancy concentration, D_V vacancy diffusivity, D_i interstitial diffusivity, γ surface energy, Ω the volume per atom, T temperature and t time. The solution of Equation 1. 9 is expressed as

$$\dot{R} = \dot{R}_0 F(\eta) + \dot{R}_e, \tag{1.10}$$

where $\dot{R}_0$ is the void-growth rate in the absence of both homogeneous recombination ($k_{iv} = 0$) and thermal emission (C_V^{eq} =0).

The equilibrium vacancy concentration (C_V^{eq}) and the vacancy diffusivity (D_V) are the two highly temperature sensitive parameters [52]. As shown in Figure 1.23, the void radius might first increase and then decrease as temperature increases. At low temperatures, D_V becomes small and the parameter η becomes large ($F(\eta)$ becomes small). Since both $\dot{R}_e$ and $F(\eta)$ become small at low temperature, the void growth ceases in the limit. At the opposite extreme of high temperature, η becomes small and $F(\eta)$ approaches unity; $\dot{R}_e$ becomes increasingly negative. Thus the theory predicts a temperature at which the void-growth rate is a maximum (corresponding to the observed peak swelling temperature). Beyond this temperature, void growth should rapidly decrease and eventually become negative since the voids tend to evaporate rather grow [52].

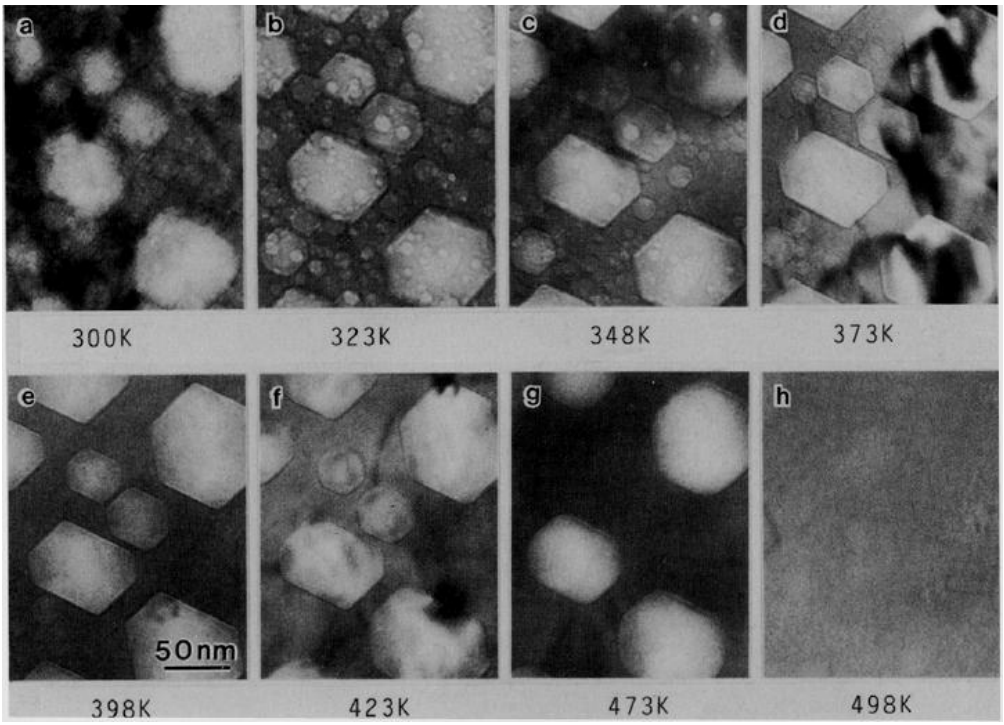

Figure 1.24 Behavior of bubble shrinkage and disappearance during annealing from 300 to 498 K after 10 keV H^+ irradiation in alumina at 113 K. The smaller bubbles disappear near 330 K and the bigger ones disappear at a higher temperature around 498 K [55].

In-situ TEM observations have been performed to investigate the H_2 bubble shrinkage behaviors in alumina matrix after 10 keV H^+ irradiation(Figure 1.24) [55]. The small bubbles of about 2.5 nm in radius began to shrink initially and disappeared at low temperatures near 330 K, and then larger bubbles began to shrink and vanished at higher temperatures. All the bubbles disappeared at 498 K. Another interesting feature seen in these figures is that the bubbles exhibiting a round shape at room temperature produced facets at 323 K and then became roundish again with increasing temperatures. This change to roundish shape in the bubbles is considered to correspond to the change in the inner pressure of bubbles due to the partial emission of hydrogen [55].

1.4. Objectives, significance and questions

The primary objectives of this research is to investigate the internal structure of fission tracks in fluorapatite and to develop a fundamental understanding of thermally- or radiolytically-induced fission track fading at atomic level. Fission tracks have been extensively used to date geological samples and to reconstruct the thermal history of rock units. The atomic-scale structure of latent, unetched, fission tracks controls their annealing, or "fading," mechanism, and the final length of etched tracks. However, there have been no systematic studies of the internal structure of fission track in fluorapatite at atomic level and its control on the fission track annealing mechanisms is still unknown. The internal structure of fission track in fluorapatite has been assumed as amorphous as in other target materials. Therefore the annealing of fission tracks in fluoapatite is believed to be a process of recrystallization of amorphous cores. The atomic level research will provide important information for a better understanding of track fading at geological timescale, and will be a critical step towards improving fission track dating. Systematic studies of hollow fission tracks and their annealing behaviors in fluorapatite at atomic level will be discussed in the next chapters. The internal structure and the annealing behavior between hollow tracks in fluorapatite and amorphous tracks will be compared. The principal questions addressed in the research include:

1. What is the internal structure of fission tracks in volatile rich fluorapatite and what are the differences between hollow tracks and amorphous tracks? Where does the decomposed material go? Do the hollow tracks contain any gaseous phases? Is it possible to fill the hollow tracks with heavy elements?

2. What is thermal annealing of fission tracks, and what happens when heating a fluorapatite fission track at high temperatures? How does thermal annealing produce a reduction of etchable track length in fluorapatite? Do segmentation of fission tracks and random motion of track segments cause the unecthable gap? What are the atomic level annealing mechanisms of fission tracks in fluorapatite? Does the recrystallization process atom by atom cause the same shrinkage of track radius as well as the ecthable length in both zircon and fluorapatite? What causes the rapid annealing (or the orientation effect) when the tracks perpendicular to c axis in fluorapatite?

3. What is electron beam-induced annealing of fission tracks? What are the differences and similarities between thermal annealing and radiolytic annealing of tracks? Why track-segments are so similar to electron irradiation induced bubbles in many aspects?

4. How does the decomposition process of volatile-rich materials influence on the track radius? What is the relation of track radius and the stopping power? Is that possible to simulate the fission track profile if knowing the track radius dependence on the stopping power?

1. T. Tagami and P.B. O'Sullivan, *Fundamentals of fission track thermochronology*. Rev. in Mineralogical & Geochemistry, 2005. **58**: p. 19-47.
2. T.A. Paul and P.G. Fitzgerald, *Transmission electron microscopic investigation of fission tracks in fluorapatite.* Am. Mineral., 1992. **77**: p. 336-344.
3. T.A. Paul, *Transmission electron microscopy investigation of unetched fission tracks in fluorapatite-physical process of annealing.* Nucl. Tracks. Radiat. Meas., 1993. **21**: p. 507-511.
4. R.L. Fleischer, P.B. Price and R.M. Walker, *Nuclear Tracks in Solids*. 1975, Berkeley: University of California Press. 31.

5. A. Meftah, F. Brisard, J.M. Costantini, M. Hage-Ali, J.P. Stoquert, F. Studer and M. Toulemonde, *Swift heavy ions in magnetic insulators: A damage cross section velocity effect.* Phys. Rev. B, 1993. **48**: p. 920.
6. SRIM, *http://www.srim.org/SRIM/SRIM2006.htm*. 2006.
7. L. Chadderton, *Nuclear tracks in solids: registration physics and the compound spike.* Radiat. Meas., 2003. **36**: p. 13-34.
8. R.L. Fleischer, P.B. Price and R.M. Walker, *Ion explosion spike mechanism for formation of charged particle tracks in solids.* J. Appl. Phys., 1965. **36**: p. 3645-3652.
9. A. Dunlop, G. Jaskierowicz and S. Della-Negra, *Latent track formation in silicon irradiated by 30 MeV fullerenes.* Nucl. Instrum. Methods Phys. Res., Sect. B, 1998. **146**: p. 302-308.
10. F. Seitz and J.S. Koehler, *Displacement of atoms during irradiation.* Solid State Phys. , 1952. **2**: p. 305–448.
11. A.J.W. Gleadow, I.R. Duddy, P.F. Green and J.F. Lovering, *Confined fission track lengths in apatite: a diagnostic tool for thermal history analysis.* Contrib. Mineral. Petrol., 1986. **94**: p. 405- 415.
12. A.J.W. Gleadow, D.X. Belton, B.P. Kohn and R.W. Brown, *Fission track dating of phosphate minerals and the thermochronology of apatite*, in *Reviews in Mineralogy & Geochemistry*, M.J. Kohn, J. Rakovan, and J.M. Huges, Editors. 2002: Washington, DC. p. 579-630.
13. G.A. Wagner and D. Storzer, *Fission track length reductions in minerals and the thermal history of rocks.* Trans. Am. Nucl. Soc., 1972. **15**: p. 127-128.
14. A.J.W. Gleadow, I.R. Duddy, P.F. Green and J.F. Lovering, *Fission track analysis: A new tool for the evalution of thermal histories and hydrocarbon potential.* Austral. Petrol. Explor. Assoc. J., 1983. **23**: p. 93-102.
15. P.F. Green, I.R. Duddy, G.M. Laslett, K.A. Hegarty, A.J.W. Gleadow and J.F. Lovering, *Thermal annealing of fission tracks in apatite 4. Quantitative modelling techniques and extension to geological timescales.* Chem. Geol., 1989. **79**: p. 155-182.
16. K.D. Crowley, M. Cameron and R. Schaefer, *Experimental studies of annealing of etched fission tracks in fluorapatite.* Geochimica et Cosmochimica Acta, 1991. **55**(5): p. 1449-1465.
17. P.F. Green, I.R. Duddy, A.J.W. Gleadow, T. P.R. and G.M. Laslett, *Thermal annealing of fission track in apatite, 1. A qualitative description.* Chem. Geol., 1986. **59**: p. 237-328.
18. P.F. Green, I.R. Duddy, A.J.W. Gleadow and T. P.R., *Fission-track annealing in apatite: track length measurements and the form of the Arrhenius plot.* Nucl. Tracks. Radiat. Meas., 1985. **10**: p. 323-328.
19. G.M. Laslett, P.F. Green, D. I.R. and G. A.J.W., *Thermal annealing of fission track in apatite, 2. A quantitative analysis.* Chem. Geol., 1987. **65**: p. 1-13.
20. W.D. Carlson, *Mechanisms and kinetics of apatite fission-track annealing.* Am. Mineral., 1990. **75**: p. 1120-1139.
21. P.F. Green, I.R. Duddy and G.M. Laslett, *Can fission track annealing in apatite be described by first-order kinetics?* Earth and Planetary Science letters, 1988. **87**: p. 216-228.

22. P.F. Green, G.M. Laslett and I.R. Duddy, *Mechanisms and kinetics of apatite fission-track annealing-Discussion.* Am. Mineral., 1993. **78**: p. 441-445.
23. K.D. Crowley, *Mechanisms and kinetics of apatite fission-track annealing-Discussion.* Am. Mineral., 1993. **78**: p. 210-212.
24. R.L. Fleischer, *Fission tracks in solids - production mechanisms and natural origins.* Mater. Sci., 2004. **39**: p. 3901-3911.
25. R.M. Papaleo, R. Leal, C. Trautmann and E.M. Bringa, *Cratering by MeV-GeV ions as a function of angle of incidence.* NIM B, 2003. **206**: p. 7-12.
26. A. Adla, H. Fuess and C. Trautmann, *Characterization of heavy ion tracks in polymers by transmission electron microscopy.* J. Polym. Sci. A2, 2003. **41**: p. 2892-2901.
27. J. Vetter, R. Scholz, D. Dobrev and L. Nistor, *HREM investigation of latent tracks in GeS and mica induced by high energy ions.* Nucl. Instrum. Methods Phys. Res., Sect. B, 1998. **141**: p. 747-752.
28. G. Jaskierowicz, A. Dunlop and R. Jonckheere, *Track formation in fluorapatite irradiated with energetic cluster ions.* Nucl. Instrum. Methods Phys. Res., Sect. B, 2004. **222**: p. 213-227.
29. D. Fink, V. Hnatowicz and P.Y. Apel, *Modifications on the molecular and supramolecular level*. Fundamentals of Ion-irradiated polymers, ed. R. Hull and R.M. Osgood. 2004. 319.
30. Y. Eyal and K. Gassan, *Observation of latent heavy-ion tracks in polyimide by means of transmission electron microscopy.* Nucl. Instrum. Methods Phys. Res., Sect. B, 1999. **156**: p. 183-190.
31. T. Tagami and P.B. O'Sullivan, *Foundamentals of fission track thermochronology.* Rev. in Mineralogical & Geochemistry, 2005. **58**: p. 19-47.
32. J. Jensen, A. Dunlop and S. Della-Negra, *Tracks induced in CaF_2 by MeV cluster irradiation.* Nucl. Instrum. Methods Phys. Res., Sect. B, 1998. **141**: p. 753-762.
33. S.A. Saleh and Y. Eyal, *Porous track cores along wakes of swift Pb ions in LiF.* NIM B, 2005 **230**: p. 246–250.
34. A. Meldrum, S.J. Zinkle, L.A. Boatner and R.C. Ewing, *A transient liquid-like phase in the displacement cascades of zircon, hafnon and thorite.* Nature, 1998. **395**(6697): p. 56-58.
35. A. Meldrum, L.M. Wang and R.C. Ewing, *Electron-irradiation-induced phase segregation in crystalline and amorphous apatite: A TEM study.* Am. Mineral., 1997. **82**(9-10): p. 858-869.
36. M. Cameron, L.M. Wang, K.D. Crowley and R.C. Ewing. *HRTEM observations on electron irradiation damage in F-apatite*. in *50th Annual Meeting of the Microscopy Society of American*. 1992. San Francisco: San Francisco Press.
37. S.A. Saleh and Y. Eyala, *Porous tracks along wakes of swift uranium ions in polyimide.* Appl. Phys. Lett., 2004. **85**: p. 2529.
38. S.A. Saleh and Y. Eyal, *Morphologies of latent and etched heavy-ion tracks in {111} CaF2.* Philosophical Magazine, 2007. **87**: p. 3967–3980
39. A. Adla, H. Fuess and C. Trautmann, *Characterization of heavy ion tracks in Polymers by Transmission Electron Microscopy.* J. Polymer Science, 2003. **41**: p. 2892.

40. P. Kluth, C.S. Schnohr, O.H. Pakarinen, F. Djurabekova, D.J. Sprouster, R. Giulian, M.C. Ridgway, A.P. Byrne, C. Trautmann, D.J. Cookson, K. Nordlund and M. Toulemonde, *Fine Structure in Swift Heavy Ion Tracks in Amorphous SiO_2*. Phys. Rev. Lett., 2008. **101**: p. 175503.
41. K. Schwartz, C. Trautmann, T. Steckenreiter, O. Geiß and M. Kra ïmer, *Damage and track morphology in LiF crystals irradiated with GeV ions.* Phys. Rev. B, 1998. **58**: p. 11232.
42. N. Khalfaoui, C.C. Rotaru, S. Bouffard, M. Toulemonde, J.P. Stoquert, F. Haas, C. Trautmann, J. Jensen and A. Dunlop, *Characterization of swift heavy ion tracks in CaF_2 by scanning force and transmission electron microscopy*. NIM B, 2005. **240**: p. 819-828.
43. T. Ding, *Self-organization of three-dimensional nano-void superlattice in electron irradiated calcium fluoride*, in *Nuclear Engineering and Radiological Sciences*. 2007, University of Michigan: Ann Arbor.
44. L.P. Zenser and R. Gruehn, *Decomposition of MgF_2 in the transmission electron microscope.* J. Solid State Chem., 2001. **157**: p. 30-39.
45. M. Cameron, L.M. Wang, K.D. Crowley and R.C. Ewing. *HRTEM observations on electron irradiation damage in F-apatite*. in *50 st Annual Meeting of the Microscopy Society of American*. 1992. San Francisco: San Francisco Press.
46. L. Calderin, M.J. Stott and A. Rubio, *Electronic and crystallographic structure of apatites.* Phys. Rev. B, 2003. **67**: p. 134106.
47. R.A. Donelick, R.A. Ketcham and W.D. Carlson, *Variability of apatite fission-track annealing kinetics: II. Crystallographic orientation effects.* Am. Mineral., 1999. **84**: p. 1224-1234.
48. S. Miro, D. Grebille, D. Chateigner, D. Pelloquin, J.P. Stoquert, J.J. Grob, J.M. Costantini and F. Studer, *X-ray diffraction study of damage induced by swift heavy ion irradiation in fluorapatite.* Nucl. Instrum. Methods Phys. Res., Sect. B, 2005. **227**: p. 306-318.
49. A.M. Glaeser, *Model studies of Rayleigh instabilities via microdesigned interfaces.* Interface Sci., 2001. **9**: p. 65-82.
50. F.A. Nichols and W.W. Mullins, *Surface-(interface-) and volume-diffusion contributions to morphological changes driven by capillarity.* Trans. Met. Soc. AIME, 1965. **233**: p. 1840.
51. D.A. Porter and K.E. Easterling, *Phase Transformations in Metals and Alloys*. 1981: Van Nostrand Teinhold Co. Ltd.
52. D.R. Olander, *Fundamental Aspects of Nuclear Reactor Fuel Elements*. 1976, Springfield, Virginia: National Technical Information Service, U.S. Department of Commerce. 236-239, 490-491.
53. S.K. Tyler and R.S. Averback, *Direct Evidence for the Brownian motion of helium bubbles.* J. Nucl. Mater., 1980. **92**: p. 201.
54. A.D. Brailsford and R. Bullough, *The rate theory of swelling due to void growth in irradiated metals.* Journal of Nuclear Materials, 1972. **44**(2): p. 121-135
55. S. Furuno, K. Hojou, H. Otsu, K. Izui, N. Kamigaki and T. Kino, *In-situ observation of the dynamic behavior of bubbles in aluminum during 10 keV H_2^+ ion irradiation and successive annealing.* Journal of Nuclear Materials, 1991. **179-181**: p. 1011-1014

CHAPTER II

HOLLOW FISSION TRACKS IN FLUORAPATITE

2.1. Background

Fission tracks, as revealed by chemical etching, have been extensively used to date geological samples and to reconstruct the thermal history of rock units [1, 2]. The atomic-scale structure of latent, unetched, fission tracks controls their annealing, "fading", and the corresponding length of etched tracks [2-5]. Models of track annealing have long been limited to empirical fits to etched track length data without any consideration of the atomic-scale track structure [6-8]. Due to the lack of direct experimental evidence, track annealing was described as an atom-to-atom damage recovery of an amorphized phase [4], resulting in the gradual reduction of the observed etched track length. In volatile-rich fluorapatite, the internal structure of tracks has been also assumed to be a straight cylinder containing an amorphous volume [1, 9, 10]created by the energy deposited along the fission-fragment trajectory, but there are no systematic studies related to this topic, even though this is important to understanding the annealing mechanism.

Details on the damage structure depend on the target material and energy deposition. Tracks in many oxides and complex ceramics are demonstrated to be amorphous domains embedded in a crystalline matrix. In volatile-rich polymers, high

energy ion irradiation is believed to produce a free volume inside the organic material [13-15]. The high sensitivity to radiation damage make direct TEM observations difficult as the structure is rapidly modified under the electron beam [14, 15]. Void-like structures were also shown under TEM to exist in other volatile-rich solids, *e.g.*, CaF_2 and fluorapatite ($Ca_{10}(PO_4)_6F_2$) [16, 17], but the hollow nature of tracks has not directly confirmed.

2.2. Experiments

Two types of tracks are investigated in this study: (1) randomly oriented thermal-neutron induced tracks from fission of ^{235}U created in the naturally-occurring, hexagonal fluorapatite from Durango, Mexico, (2) parallel tracks produced by swift ions in single crystals (bulk thickness: 50 μm) of the same material along the *c-axis*. Ion irradiations have been performed at the UNILAC-accelerator of the GSI Helmholtz Centre for Heavy Ion Research at Darmstadt, Germany. Swift heavy ions create much longer tracks (*e.g.* 2.2 GeV Au ions: 90 μm) as compared to typical fission fragments (100 MeV Xe ions: ~ 10 μm). The mass and kinetic energy determine the energy loss per unit path length of ions, d*E*/d*x*, and this value was for the swift Au ions of this study slightly higher as compared to an average fission fragment (2.2 GeV Au ions: 26 keV/nm *vs*. 100 MeV Xe ions: 16 keV/nm). However, this small difference in energy loss per depth does not result in significant differences in the track morphology [12]. TEM studies have been conducted with a JEOL JEM 2000FX, a JEOL 3011, and a JEM 2010F electron microscope. To avoid possible ion-irradiation induced damage during the sample preparation, crushed power samples deposited Cu grid with carbon film were prepared

for all the TEM studies as described elsewhere [18]. During the TEM observations, the electron current density was kept as low as possible (0.1 to 1 A/cm^2) to minimize electron-irradiation-induced microstructural changes. A Muffle furnace was used to perform the *ex situ* annealing of fission tracks with a crushed sample which was sealed in an Ar protected tube.

2.3. Evidence of hollow fission tracks in fluorapatite

Randomly oriented neutron-induced fission tracks within the fluorapatite matrix can be directly observed by TEM (Figure 2.1, Figure 2.1(1)) and HRTEM (Figure 2.2(2)) when they are slightly out of focus. The randomly orientated track actually embedded in the matrix, and the image of the track core actually contains the structural information from both the track and the matrix. Therefore, one should find a track strictly parallel to electron beam to reveal the atomic-scale internal structure the track.

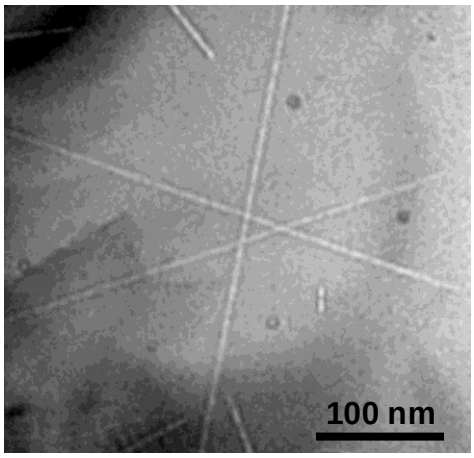

Figure 2.1 Fission tracks. Randomly oriented neutron induced fission tracks are embedded in fluorapatite mineral, which can be observed by TEM. There are no fundamental differences in the nature of the tracks created by the spontaneous fission of ^{238}U or the neutron-induced fission of ^{235}U.

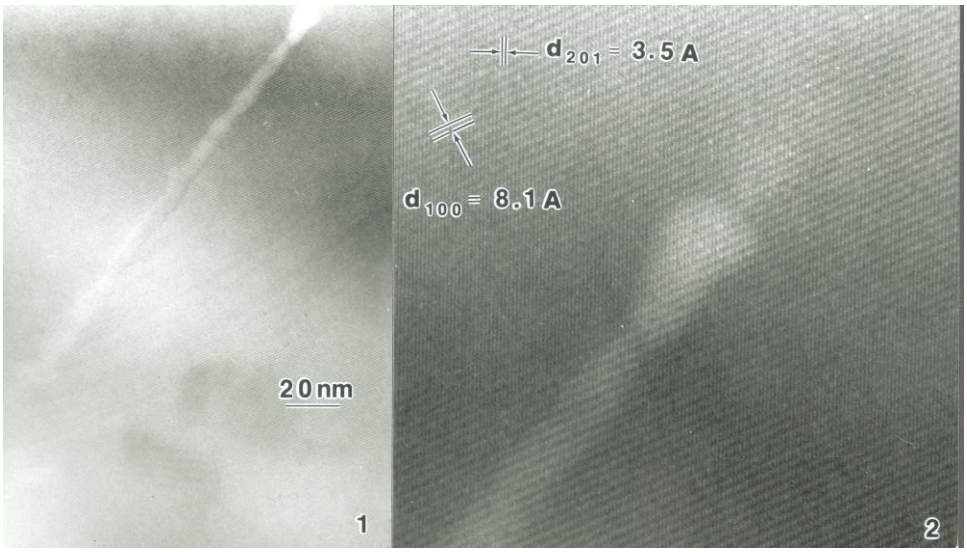

Figure 2.2 Conventional TEM (1) and HRTEM (2) images of a fluorapatite fission track, which is perpendicular to electron beam direction. The images were provided by Prof. L.M. Wang.

2.3.1. Direct observation of hollow track by HRTEM

Due to the random orientation of damage trails, it is extremely difficult to directly reveal the atomic-scale internal structure of an individual track using high resolution TEM (HRTEM). This requires a sample tilting to align the electron beam parallel to the track, while also requires the track trajectory happens to be along a main zone axis for direct observations of the crossing lattice-fringes in HRTEM. The extended time of electron exposure would cause severe modifications of the initial structure of the single track. In contrast to randomly oriented fission tracks, irradiations with swift heavy ions produces parallel tracks of specific orientations. By choosing a proper irradiation surface and irradiation angle, the track alignment can be adjusted along specific crystal zone axis. These advantages can protest the tracks on one side of a crushed particle from prolonged

electron beam irradiation by intentionally performing the tilting on other side. At a low current density (~ 0.5 A/cm^2), the hollow nature of ion-induced tracks (2.2 GeV Au) in fluorapatite has been directly observed by HRTEM (Figure 2.3). The central region of the track has the same contrast as the free space beside the sample suggesting that no solid components are left in the track core.

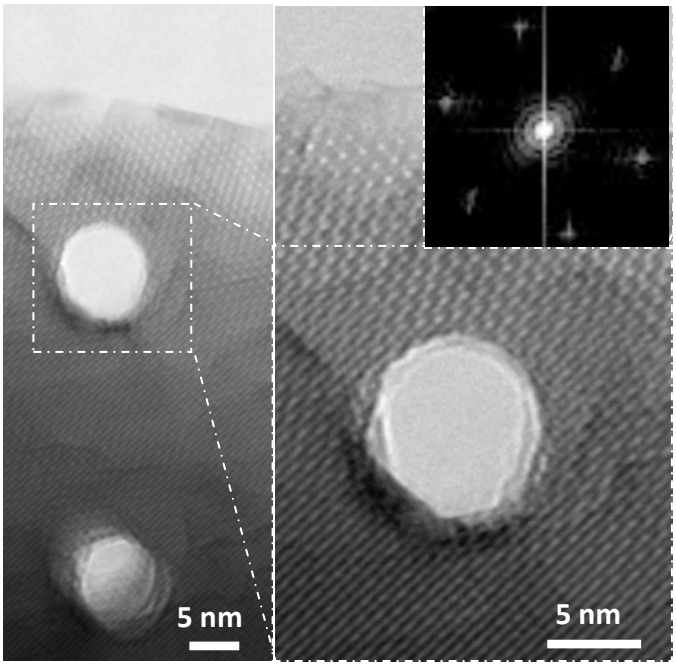

Figure 2.3 HRTEM image. Plan view HRTEM images of tracks induced by 2.2 GeV Au ions showing a hollow core region. The tracks are deliberately produced along the *c* axis of a fluorapatite single crystal. The Airy pattern in the inset fast Fourier transform (FFT) image taken from the framed region further suggests the track is a hole.

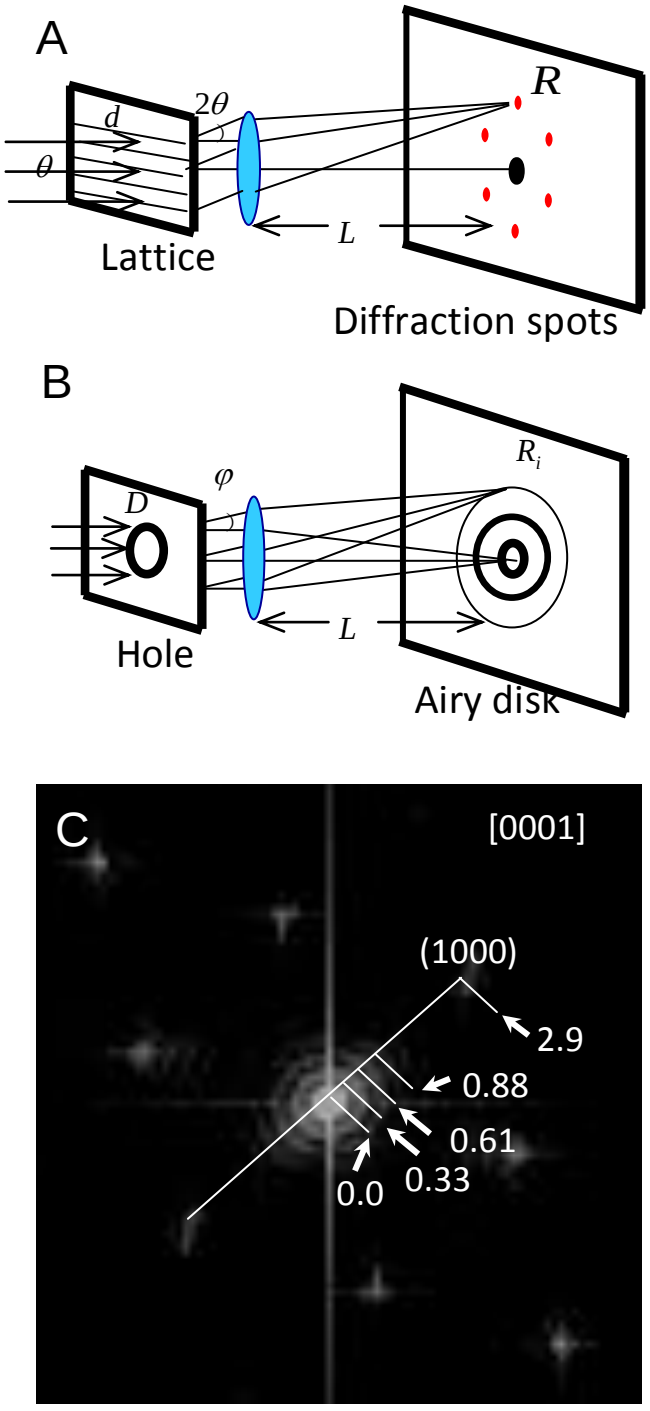

Figure 2.4 Schematic illustrations of forming (A) diffraction spots and (B) Airy pattern, respectively. (C) Analysis of the actual FFT image showing the calculated size (~8.6 nm) of the circular hole matches well with the observed track diameter in the HRTEM image.

A very interesting Airy pattern and diffraction pattern are shown in the same Fast Fluorite Transform (FFT) image centered at the hollow track in apatite (the inset of Figure 2.3 and Figure 2.4C). It is straightforward to understand that the hexagonal diffraction spots are from the {1000} and $\{1\bar{1}00\}$ spacing groups in fluorapatite, which have the same lattice spacing of 0.811 nm (Figure 2.4A). Knowing the lattice spacing of {1000} and $\{1\bar{1}00\}$ planes one can easily calculate the camera length using the following equation,

$$\frac{R}{L} = 2\theta = \frac{\lambda}{d}, \tag{2.1}$$

where d is the lattice spacing, L camera length and λ wave length of electrons (0.00197 nm for 300 keV TEM). The Airy rings are speculated to result from the circular aperture diffraction (Figure 2.4B). The relationship between the radii of dark rings and the diameter of the hole can be determined by,

$$\frac{R_i}{L} = \varphi = 1.22\frac{\lambda}{D}, 2.23\frac{\lambda}{D}, 3.24\frac{\lambda}{D}... \tag{2.2}$$

where D is the diameter of the aperture. It should be noted that the distance between each dark ring is not a constant. By measuring the radius of each dark ring, the diameter of the track can be obtained as shown in Table 2.1. All the three calculated diameters from the three dark rings match well with the observed diameter (8~9 nm) by HRTEM, which confirms that the rings are resulted from the circular aperture diffraction. In the real space, the size of the hollow track (8.6 nm) is only an order of magnitude larger than that of lattice (0.81 nm). This makes it possible to show both Airy pattern and diffraction pattern in a single FFT image in the inverse space. The Airy pattern further verifies no solid component left within the hollow track to deflect the electron beam.

Table 2.1 Calculation of the camera length and the track size from the diffraction spots and Airy rings in the FFT image.

FFT features	R (cm)	L (cm)	d (nm)	D (nm)
Spot (1000)	2.9	1193.8	0.811	
3rd Airy Ring	0.88	1193.8		D_3 =8.69
2nd Airy Ring	0.61	1193.8		D_2 =8.58
1st Airy Ring	0.33	1193.8		D_1 =8.68

2.3.2. Fresnel contrast and Fresnel fringe from hollow fission tracks

I have taken the images of fission tracks in fluorapatite using the Fresnel contrast method. Fresnel contrast is often used to demonstrate that the defect is cavity and to determine its shape. One can usually see the most contrast if the content of cavity is vacuum [19]. In principle one can apply this technique to holes which contain a second phase solid, however the Fresnel contrast is likely to be hidden by stain contrast in the specimen. As shown in Figure 2.5 (b), when the image is in focus, the fission track is almost invisible. However, one would defocus the objective lens out of the bottom surface of the specimen to see the contrast as shown in Figure 2.5 (a) and (c). When changing focus, one can see very clear Fresnel contrast around the tracks, *i.e.*, dark core and bright fringe for overfocus and (c) bright core and dark fringe for underfocus conditions. The distinct change of Fresnel contrast between overfocus and under focus

conditions suggests that the electron density(or inner potential) of the matrix is significantly higher than that of the track core region, which means the content of the track is more like vacuum or gases than solid second phase. In contrast, I have applied the Fresnel contrast technique on amorphous tracks created by 2.2 GeV Au ions irradiated zircon (Figure 2.6). Significantly different to hollow tracks, the amorphous tracks are always in dark color and have no fringes surround the tracks when the focus conditions change. These experiments suggest that the inner-potential difference (or the electron-density difference) around the hollow track core and its matrix is significantly larger than that around the amorphous core and its matrix.

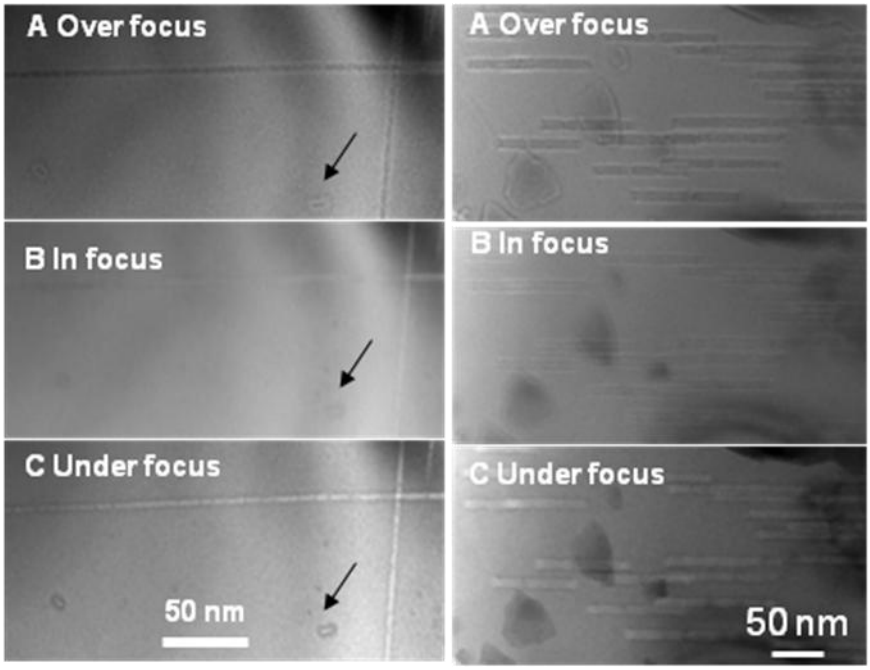

Figure 2.5 Fresnel contrast from fission tracks (left) and 2.2 GeV Au irradiated tracks (right) in fluorapatite. A) Over focus image has a dark core surrounded by a bright fringe. B) In focus image has little phase contrast. C) Under focus image has a bright core surrounded by a dark fringe. Fresnel contrast is a characteristic of bubbles or voids.

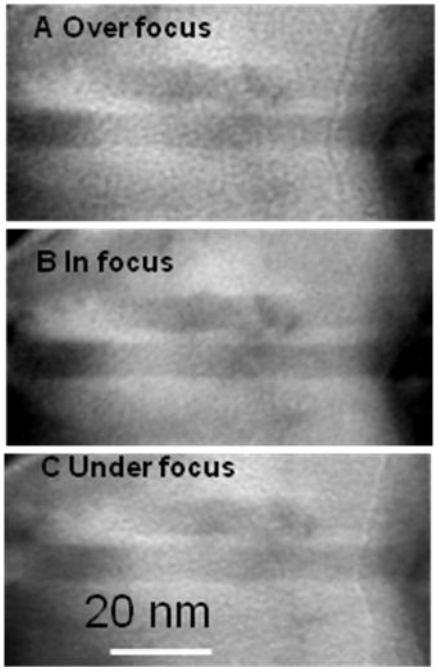

Figure 2.6 There is no Fresnel contrast shown in the amorphous tracks created by 2.2 GeV Au ions in zircon when changing from over focus, to at focus and under focus conditions. The amorphous track cores are not surrounded by any fringes.

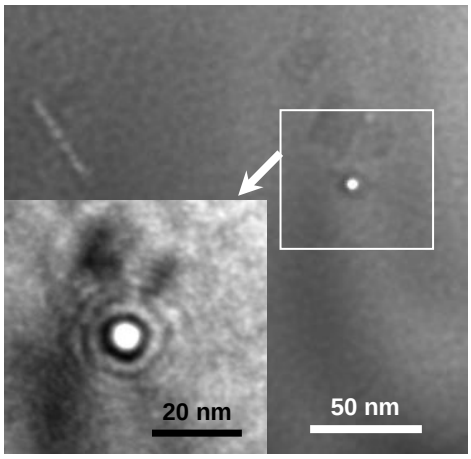

Figure 2.7 Under-focus bright-field TEM images of neutron induced fission tracks in fluorapatite in different orientations. The magnified inset image shows alternatively dark and bright Fresnel fringes, characteristic of a void space in a solid matrix.

When operating an FEG with high coherency slightly out of focus, one can find Fresnel fringe, *i.e.*, alternating dark and bright rings shown from the edge of a hole in a specimen. I have observed the Fresnel fringe from a fission track perpendicular to the sample surface. Figure 2.7 shows the under-focused TEM image of random fission tracks and the inset is an under-focused magnified TEM image showing a fission track parallel to electron beam. The Fresnel fringe from the fission track perpendicular to the surface demonstrates that the fission track passes through the whole thickness of the sample, showing strong alternatively bright and dark rings between the hole and its crystalline matrix.

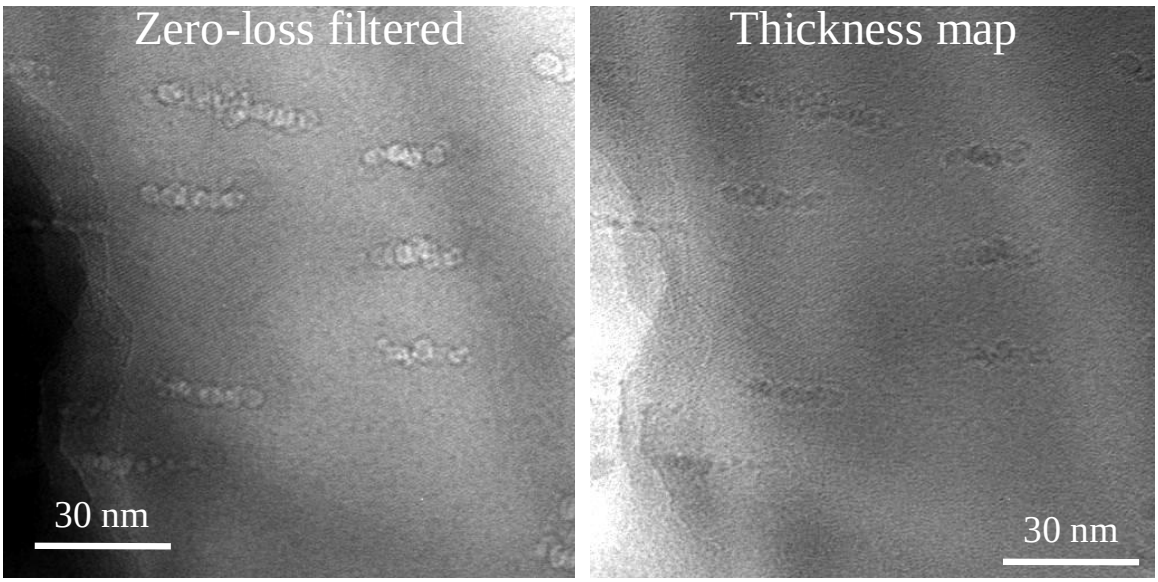

Figure 2.8 Energy filtered elastic image and corresponding thickness map of 30 MeV Au ion irradiated fluorapatite.

2.3.3. Thickness map from fission tracks and electron beam drilled holes

Electron Energy Loss Spectrometers (EELS) in TEM mode were conducted in order to investigate the internal structure of the tracks induced by 30 MeV Au ions irradiated fluorapatite. Energy filtered elastic image and corresponding thickness map of fluorapatite are shown in Figure 2.8. EELS has advantage to separate the inelastically scattered electrons, the amount of which increases with sample thickness [19]. One can see that the track cores are darker than the crystalline apatite matrix (Figure 2.8), showing that the passage of highly energetic ions results in a decrease of thickness (or a mass loss) in the tracks. The amorphous cores might be slightly darker in the thickness map than the crystalline matrix. But the contrast would not be as significant as hollow track because it is reasonable to assume that the composition of amorphous core is very close to that of its matrix. The swift ion tracks in this experiment are lying on the viewing plane therefore the images from the core regions contain the thickness signals from both the tracks and the matrix. Only the thickness map from tracks penetrating the entire thickness of the sample is capable to verify if the tracks are hollow or amorphous.

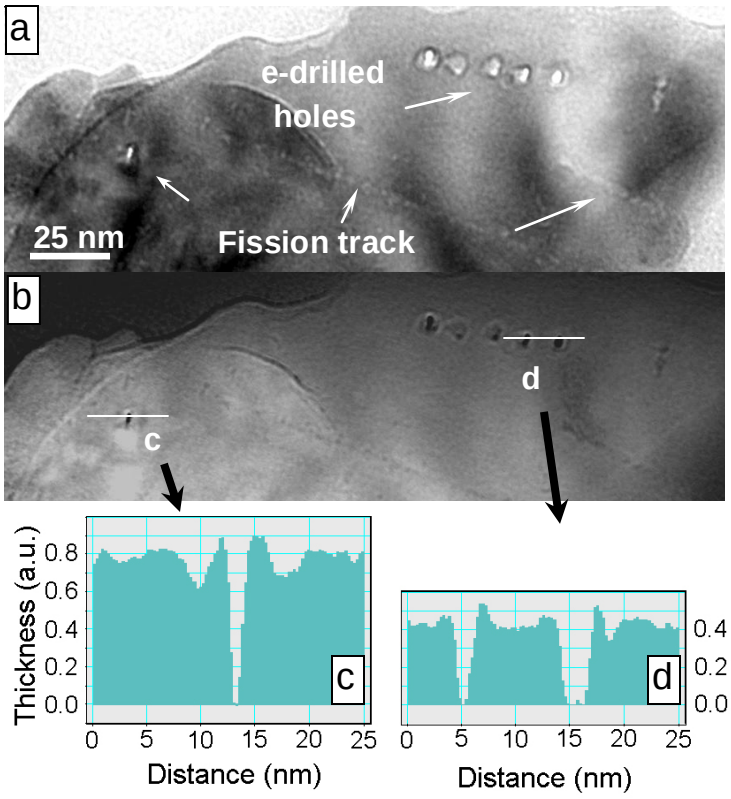

Figure 2.9 Thickness map. TEM images are taken from a region where a fission track penetrates through the entire fluorapatite layer. A sequence of five small holes in the close neighbourhood of the track was deliberately drilled using the electron beam. a, energy filtered elastic image. b, thickness map. c, thickness profile along Line c through the fission track as highlighted in the lower left of (b). d, thickness profile along Line d cutting through two electron-beam-drilled holes as highlighted in the upper right part of image (b).

Further evidence that tracks in fluorapatite are empty has been obtained by an thickness map of a through-thickness fission track and several focused electron beam drilled holes [20]. Electron Energy Loss spectroscopy in TEM mode has been applied to record a thickness map of a region where a fission-track penetrates through the entire fluorapatite layer (Figure 2.9). As marked in the elastic image(Figure 2.9a), a sequence of five small holes were deliberately drilled in the close neighborhood of the track using the electron beam [20, 21]. It allows us to directly compare the signal of the fission track and

the electron-beam drilled channel (Figure 2.9b). The thickness profiles from the fission track and the two electron-drilled holes are shown in Figure 2.9c and d, respectively. The thickness signal from the central core of the fission track is as low as the background of the sample, indicating the track completely passes through the whole thickness as the electron-beam-drilled holes do, and suggesting the fission track is hollow.

2.3.4. AFM of parallel tracks

AFM images are taken from the cleaved (0001) surface of a 2.2 GeV Au ion induced tracks along the *c-axis* of a fluorapatite single crystal in order to overcome the surface roughness due to the limitation of mechanical polishing (Figure 2.10). Again, the image of the tracks suggests that they are hollow. The depth of the tracks shown in the figure is estimated as about 10 nm, which is limited by the tip size for AFM imaging.

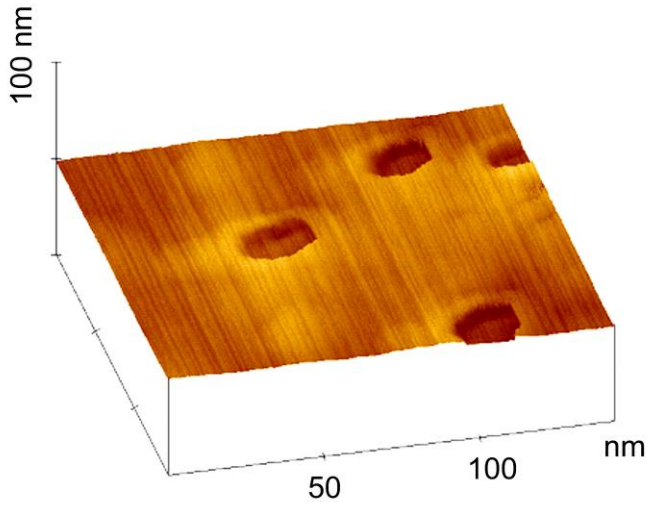

Figure 2.10 AFM image of 2.2 GeV Au ion induced tracks on a cleaved (0001) surface of fluorapatite single crystal.

2.3.5. Cu atoms filling in hollow fission tracks at 700^{o}C

As shown in Figure 2.11, Zhang *et al.* found that Cu atoms from a carbon covered TEM copper grid were able to diffuse into carbon nano-tubes at 600 ^{o}C through the openings at the end [22]. The greatly enhanced mobility of Cu atoms at elevated temperature results in the formation of Cu nano-rods inside the tubes additionally to the random accumulation of spherical Cu nano-particles on the carbon film [22]. In this work, *in situ* heating experiments have been conducted in a TEM heating stage at 700 ^{o}C to investigate the microstructure of latent fission tracks in fluoraptite (Figure 2.12). During the annealing experiments of fission tracks, I observed similar spherical Cu nano-particles immediately at 700 ^{o}C, which showed a random distribution on the fluorapatite surface and the carbon film (Figure 2.12). Interestingly, some fission tracks are filled during the heating process with cylindrical Cu nano-rods (Figure 2.12). The copper atoms diffuse through the track opening that is created by the interface of sample surface and track, and fill the empty space of the fission tracks. This is a compelling evidence to show the hollow structure of fission tracks in fluorapatite.

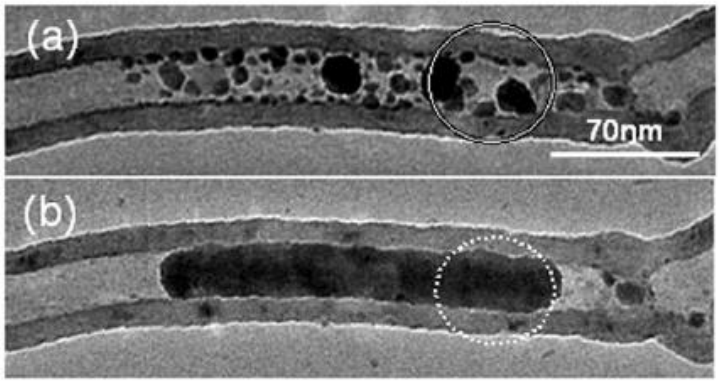

Figure 2.11 Cu atoms from copper grid filled in carbon nanotube after heating at 600^{o}C for 8 h. Cu atoms diffuse into the CNT through the open end (From Zhang et al. in [22]).

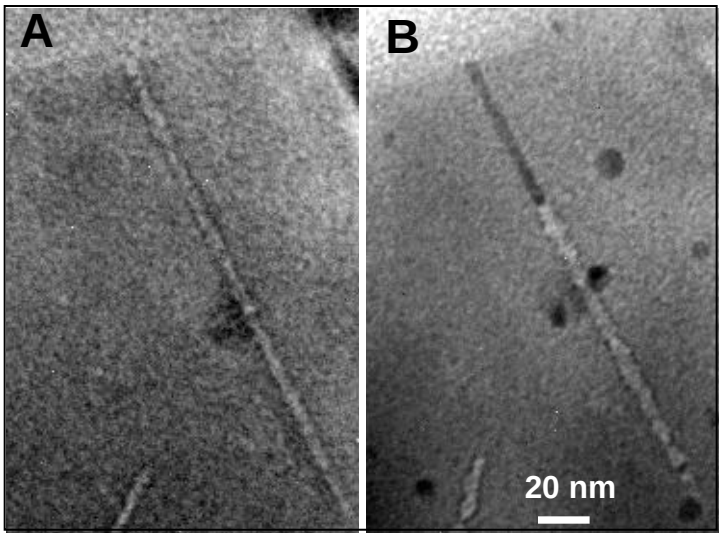

Figure 2.12 The TEM images of fission tracks in apatite (A) before heating and (B) after the temperature stabilizes at 700^{o}C for 1 minute. Cu atoms from copper grid diffuse into a fission track through the open end and form a nano-rod inside the track. Additional Cu spots are formed randomly in the sample and carbon film.

2.3.6. Other evidence

Under thermal treatment or electron beam irradiation, latent tracks tend to break up into segments. The track segments either move randomly along the track trajectory, causing the fattening of along the track trajectory, or move preferentially along [0001] direction. The enhanced diffusion by heating or electron beam irradiation on the inner surface of hollow track results in the bubbles- (or voids-) like behaviors of tracks. The preferential motion and elongation along [0001] direction has also been observed in the bubble formed during electron beam irradiation at high temperature (as it will be discussed in Chapter IV). The similarity of bubbles and fission tracks in the preferential motion under electron irradiation and under thermal treatment further confirm the hollow

nature of fission tracks. More evidence of hollow tracks will be discussed in details in Chapter III and IV, on the TEM investigations of the thermal annealing and electron beam annealing behaviors of unetched fission track in fluorapatite.

2.4. Formation of hollow track by decomposition of volatile rich fluorapatite

The formation of the hollow core may result from the radiation-induced decomposition of fluorapatite and the loss of volatile elements along the fission track due to the highly ionizing energy deposition during the track formation [23-25]. To which extent the volatile elements are completely released depends on the temperature and the interaction of the track with its environment. If the track is connected with other tracks or cleavage planes, the loss of volatile elements may be significantly enhanced. However, also the opposite process has to be considered: the filling of the hollow track structure with gas atoms *via* interactions with the solid at elevated temperatures[8] or even with the outside air. At any rate, a fission or swift heavy ion track in apatite represent a hollow channel that may be for some conditions filled with a gaseous phase, *i.e.*, does not contain amorphous material.

In situ energy dispersive x-ray spectroscopy (EDS) analysis was performed to qualitatively simulate the compositional change during fission track formation, providing that almost all the energy deposition of a fission fragment is from the electronic part (Figure 2.13). The electron beam was focused to cover a small particle to expedite the

decomposition process (particle size ~500 nm and beam current ~5 A/cm^2). Under continuous electron beam irradiation, the volatile elements can either escape to the vacuum in the TEM column resulting in a loss of these elements in the EDS spectrum, or accumulate into bubbles in a bulk sample with CaO rich rims forming gradually surrounding the matrix [24-26]. Figure 2.13 plots the normalized percentage loss of each major element in fluroapatite with the time under electron irradiation. The percentage loss is normalized by calcium because it is the most stable element in fluorapatite ($Ca_{10}(PO_4)_6F_2$). As is clearly illustrated in Figure 2.13, the normalized percentage loss of F is the highest, followed by O and P. The normalized percentage loss for F increased rapidly at the beginning and reached a saturation point when the irradiation time reaches to 20 minutes. While those for O and P keep increasing as the extent of irradiation increases up to 118 minutes. These suggest that F is more readily to sublimate and release to vacuum in a TEM than the other elements under electron beam irradiation. With the release and accumulation of gaseous phases into bubbles in a bulk sample, CaO rich surrounding matrix can be gradually formed. The progressive formation of CaO has been observed from both HRTEM images and selected area electron diffraction patterns in our pervious experiments on electron irradiation in fluorapatite [25]. Meldrum *et al.* have investigated the composition of the newly formed bubbles in electron irradiated fluorapatite by EDS analysis and reported a significant enrichment in gaseous components [24]. These results further suggest ionizing radiation is capable of decomposing fluorapatite and generating gaseous phases.

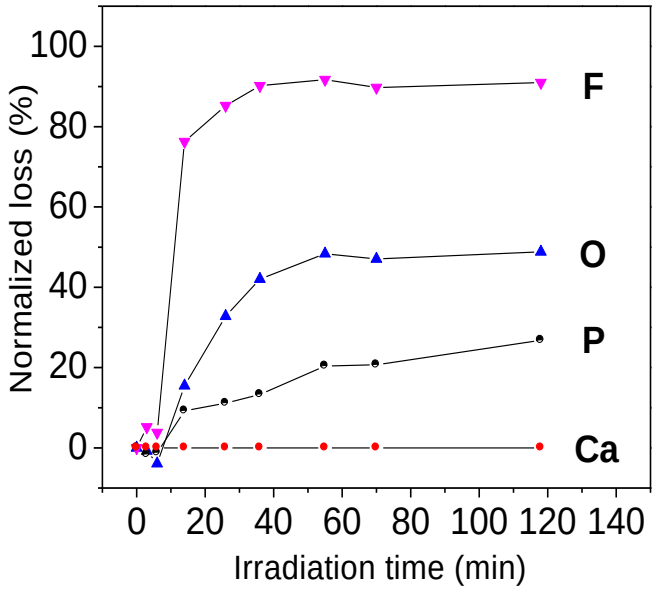

Figure 2.13 EDS analysis. The normalized percentage loss of each element normalized to calcium content, in fluorapatite under a 200 keV electron-beam irradiation with a high current (~5 A/cm^2) in a TEM for up to 118 minutes. The normalized percentage loss of F is the highest, which means that F is more readily sublimated than the other elements.

Irradiation-induced decomposition can be found in many target materials [23, 24, 26]. However, the decomposition of volatile-rich materials is likely irreversible due to the loss of the volatile elements. During track formation, the intense pressure within fission track assists in sublimation of the volatile elements into outside [17] along the track because the chance is high for a fission track (16~21 μm long and ~5 nm wide) to pass through a cleavage or another fission track [10]. The formation of the hollow structure might result from the mass loss and the subsequent inefficiency of the decomposed components returning to the originally complicated composition. It should be mentioned that the decomposition of fluoraptite during track formation is different from that during electron beam irradiation in many aspects. In the case of electronic energy deposition by

a fission fragment (10~18 keV/nm) during track formation, the decomposition occurs in an extremely short time (~10^{-12} s) and within a small volume (of the order of a track size). In comparison, the energy deposition of an electron on fluorapatite is much smaller (~0.8 eV/nm) and the irradiated region (~500 nm) is much larger. However, the prolonged irradiation (up to 118 minutes) from electrons can accumulate enough energy deposition to decompose the target material. Since the decomposition process during track formation is difficult to directly investigate in experiments, the EDS analysis of compositional change under electron exposure can provide important information of the decomposition of fluorapatite during track formation. Based on the EDS analysis, it is reasonable to infer that the volatile elements are more readily to release during the track formation.

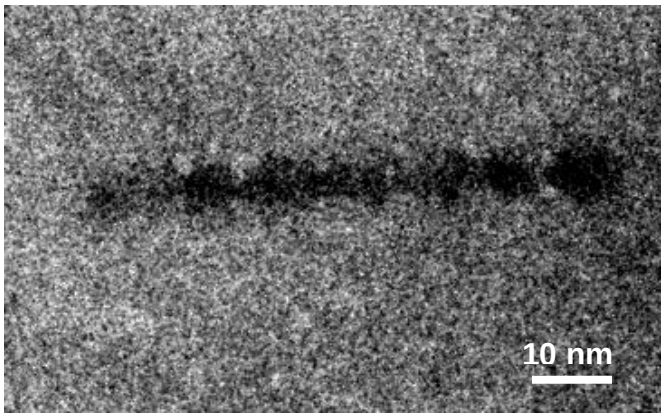

Figure 2.14 HAADF Z-contrast STEM image of a fission track. The darker contrast of a fission track in fluorapatite indicates a much lower total mass or thickness in the track core area.

High angle annular dark field STEM Z-contrast images have also been taken to investigate the composition difference between the track core and the matrix (Figure 2.14). The brightness in the image is directly proportional to the square of atomic number or the total mass in the area. The darker contrast from a fission track core in fluorapatite indicates that a significant loss of matter within the track during the track formation, which is consistent with the EDS results of the mass loss under electron irradiation. The irreversible decomposition of fluorapatite during the huge energy deposition by the fission products along their trajectory leads to sublimation of volatile elements. Jaskierowicz *et al.* believed that a series of explosions might lead to matter ejecting from the tracks and redepositing on the swift ion irradiated sample surface, on which the track is open to free space [17]. The STEM Z-contrast from the 30 MeV Au ion irradiated fluorapatite also shows the passage of energetic Au ions causes significant loss of mass, or a large decrease in the average of atomic number Z (Figure 2.15).

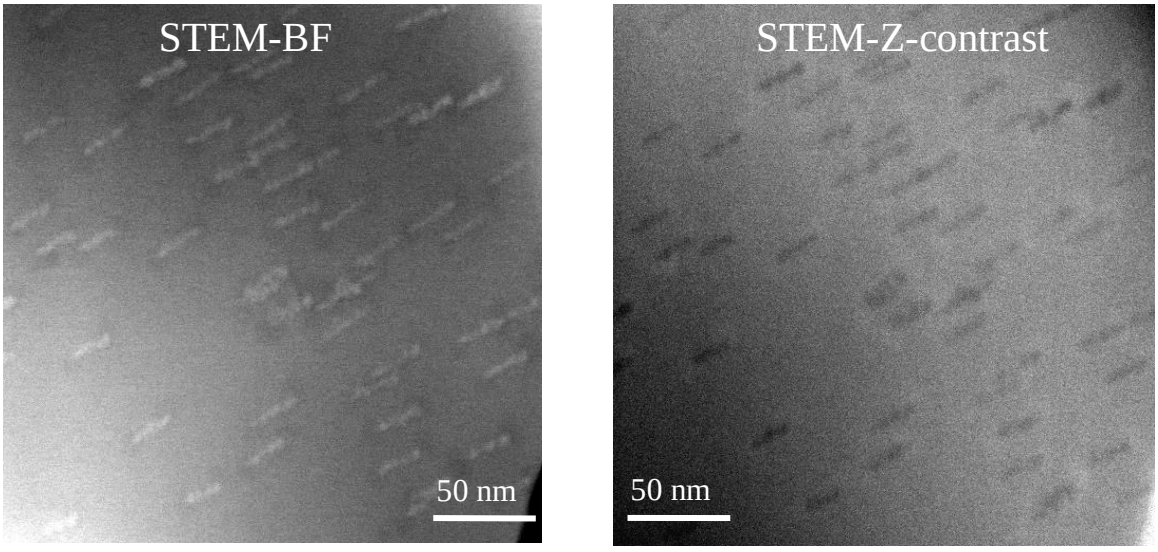

Figure 2.15 STEM bright field image and HAADF Z-contrast image of tracks induced by 30 MeV Au ions irradiation in fluorapatite.

In summary, using advanced transmission electron microscopy (TEM) techniques, it is shown that neutron-induced fission tracks in fluorapatite are hollow, but probably filled with volatile gas, instead of an amorphous core. The irreversible decomposition of fluorapatite and the sublimation of volatile elements along the fission track due to the highly ionizing energy deposition cause the formation of the hollow core. The examination of parallel tracks in fluorapatite induced by high energy ions (GeV), which have larger energy loss per unit length as fission fragments but generate much longer tracks, also support the conclusion that the tracks are hollow. I will show in next chapters that the understanding of hollow structure of latent tracks is a key to an adequate physical description of the fading of fission tracks in apatite at elevated temperatures or under electron beam irradiations. This finding provides information required of a refined physical model of track annealing. Finally, the hollow nm-sized channels (5~10 nm wide, up to 100 μm long) in fluorapatite may be provided as suitable templates for synthesis of nanostructures by applying ion-beam technology.

1. Gleadow, A.J.W., Belton, D.X., Kohn, B.P. and Brown, R.W., *Fission track dating of phosphate minerals and the thermochronology of apatite*, in *Reviews in Mineralogy & Geochemistry*, M.J. Kohn, J. Rakovan, and J.M. Huges, Editors. 2002: Washington, DC. p. 579-630.
2. Green, P.F., Duddy, I.R., Gleadow, A.J.W., Tingate, P.R. and Laslett, G.M., *Thermal annealing of fission tracks in apatite 1. A qualitative description.* Chem. Geol., 1986. **59**: p. 237-253.

3. Fleischer, R.L., Price, P.B. and Walker, R.M., *Nuclear Tracks in Solids*. 1975, Berkeley: University of California Press. 31.
4. Fleischer, R.L., *Fission tracks in solids - production mechanisms and natural origins.* J. Mater. Sci., 2004. **39**: p. 3901-3911.
5. Chadderton, L., *Nuclear tracks in solids: registration physics and the compound spike.* Radiat. Meas., 2003. **36**: p. 13-34.
6. Laslett, G.M., Green, P.F., Duddy, I.R. and Gleadow, A.J.W., *Thermal annealing of fission track in apatite, 2. A quantitative analysis.* Chem. Geol., 1987. **65**: p. 1-13.
7. Crowley, K.D., Cameron, M. and Schaefer, R., *Experimental studies of annealing of etched fission tracks in fluorapatite.* Geochimica et Cosmochimica Acta, 1991. **55**(5): p. 1449-1465.
8. Carlson, W.D., *Mechanisms and kinetics of apatite fission-track annealing.* Am. Mineral., 1990. **75**: p. 1120-1139.
9. Villa F., Grivet M., Rebetez M., Dubois C., Chambaudet A., Chevarier A., Martin P., Brossard F., Blondiaux G., Sauvage T. and M., T., *Damage morphology of Kr ion tracks in apatite: Dependence on dE/dx.* Radiation Measurements, 1999. **31**: p. 65-70.
10. Tagami, T. and O'Sullivan, P.B., *Fundamentals of fission track thermochronology.* Rev. in Mineralogical & Geochemistry, 2005. **58**: p. 19-47.
11. Meftah, A., Brisard, F., Costantini, J.M., Dooryhee, E., Hage-Ali, M., Hervieu, M., Stoquert, J.P., Studer, F. and Toulemonde, M., *Track formation in SiO_2 quartz and the thermal-spike mechanism.* Phys. Rev. B, 1994. **49**: p. 12457.
12. Meftah, A., Brisard, F., Costantini, J.M., Hage-Ali, M., Stoquert, J.P., Studer, F. and Toulemonde, M., *Swift heavy ions in magnetic insulators: A damage cross section velocity effect.* Phys. Rev. B, 1993. **48**: p. 920.
13. Adla, A., Fuess, H. and Trautmann, C., *Characterization of heavy ion tracks in polymers by transmission electron microscopy.* J. Polym. Sci. A2, 2003. **41**: p. 2892-2901.
14. Fink, D., Hnatowicz, V. and Apel, P.Y., *Modifications on the molecular and supramolecular level*. Fundamentals of Ion-irradiated polymers, ed. R. Hull and R.M. Osgood. 2004. 319.
15. Eyal, Y. and Gassan, K., *Observation of latent heavy-ion tracks in polyimide by means of transmission electron microscopy.* Nucl. Instrum. Methods Phys. Res., Sect. B, 1999. **156**: p. 183-190.
16. Jensen, J., Dunlop, A. and Della-Negra, S., *Tracks induced in CaF_2 by MeV cluster irradiation.* Nucl. Instrum. Methods Phys. Res., Sect. B, 1998. **141**: p. 753-762.
17. Jaskierowicz, G., Dunlop, A. and Jonckheere, R., *Track formation in fluorapatite irradiated with energetic cluster ions.* Nucl. Instrum. Methods Phys. Res., Sect. B, 2004. **222**: p. 213-227.
18. Headley, T.J., Ewing, R.C. and Haaker, R.F., *Amorphous structure of metamict minerals observed by TEM.* Nature, 1981. **293**(5832): p. 449-450.
19. William, D.B. and C.B., C., *Transmission electron microscopy*. 1996, New York and London. 82 and 450.

20. Sun, K., Wang, L.M. and Ewing, R.C., *Fabrication of nano/micro-patterns on iron phosphate glass surfaces by focused energetic beams.* NIM B, 2008. **266**: p. 3133.
21. Bysakh, S., Shimojo, M. and Mitsuishi, K., *Mechanisms, of nano-hole drilling due to nano-probe intense electron beam irradiation on a stainless steel.* J. Vac. Sci. Technol., B., 2004. **22**: p. 2620-2627.
22. Zhang, Z. and Su, D., *Behaviour of TEM metal grids during in-situ heating experiments.* Ultramicroscopy, 2009. **109**: p. 766-774.
23. Meldrum, A., Zinkle, S.J., Boatner, L.A. and Ewing, R.C., *A transient liquid-like phase in the displacement cascades of zircon, hafnon and thorite.* Nature, 1998. **395**(6697): p. 56-58.
24. Meldrum, A., Wang, L.M. and Ewing, R.C., *Electron-irradiation-induced phase segregation in crystalline and amorphous apatite: A TEM study.* Am. Mineral., 1997. **82**(9-10): p. 858-869.
25. Cameron, M., Wang, L.M., Crowley, K.D. and Ewing, R.C. *HRTEM observations on electron irradiation damage in F-apatite*. in *50th Annual Meeting of the Microscopy Society of American*. 1992. San Francisco: San Francisco Press.
26. Zenser, L.P. and Gruehn, R., *Decomposition of MgF_2 in the transmission electron microscope.* J. Solid State Chem., 2001. **157**: p. 30-39.

CHAPTER III

THERMAL ANNEALING OF FISSION TRACKS IN FLUORAPATITE

3.1. Background

A fission track is a 5~10 nm wide damage-trail created by a pair of spontaneous fission fragments of ^{238}U that have trajectories in opposite directions. The total kinetic energy for the pair is around 170 MeV [1], corresponding to a range of 16~20 μm in fluorapatite ($Ca_{10}(PO_4)_6F_2$). Fission track ages in apatite are generally accepted as giving a measure of the time over which a sample has been exposed to temperatures below approximately 150 ℃ [2]. The continuous production of tracks through time is on the order of 10^6 to 10^9 years [3], coupled with the fact that the length of each track shrinks to a value characteristic of the maximum temperature it has experienced. Thus, final length directly reflects the variation of temperature with time.

This consideration has lead to numerous efforts to quantify the kinetics of apatite fission track annealing on the basis of laboratory experiments in which track length distributions are measured in crystals subjected to controlled thermal histories [4-5]. Laboratory heating experiments are conducted on material containing fission

tracks at a series of temperatures (T) and times (t) in order to describe the degree of annealing of fission tracks by:

$$\frac{dr}{dt} = -\alpha_0 r \exp(\frac{-E_A}{kT}) \tag{3.1}$$

where r is the degree of annealing(or the ratio of length between annealed track and original track), k Boltzmann's constant, α_0 a constant and E_A the activation energy [6]. After furnace heating, the fission tracks around 5~10 nm in width are etched and enlarged to several micrometers. The track lengths are then measured by an optical microscope to determine the annealing degree. The etched fission tracks in fluorapatite have been found to be completely annealed at around 360 ℃ for one hour [5, 7-8]. Empirical, mathematical models have been presented for the quantitatively thermal history fitting the observed fission track data, as shown in Figure 3.1 [9]. Green *et al.* concluded that temperature dominates over time in determining final fission track parameters, with an order of magnitude increase in time being equivalent to a ~ 10 ℃ increase in temperature [4]. However, the interpretation of fission track ages in the nature is required to assume that the same physical processes consistently govern track shortening at both high temperature (95-400 ℃) in the laboratory and low temperature (below 150 ℃) in the nature. This means the application of experimental studies to natural occurrences requires the extrapolation of laboratory data measured up to 500 days to geological times of the order of millions of years. Thus, these treatments have been criticized as purely empirical, based upon mathematical features of laboratory results without a clear physical significance [2]. Furthermore, chemical etching removes not only the disordered region comprising the latent track but also an indeterminate volume of the surrounding crystal. The geometry of etched tracks depends not only on the structure of latent track, but also

the composition and concentration of the etchant, as well as on the chemistry and structure of the apatite [5]. This approach that is dealing with etched tracks is difficult to obtain a fundamental understanding of the processes that occur during track annealing.

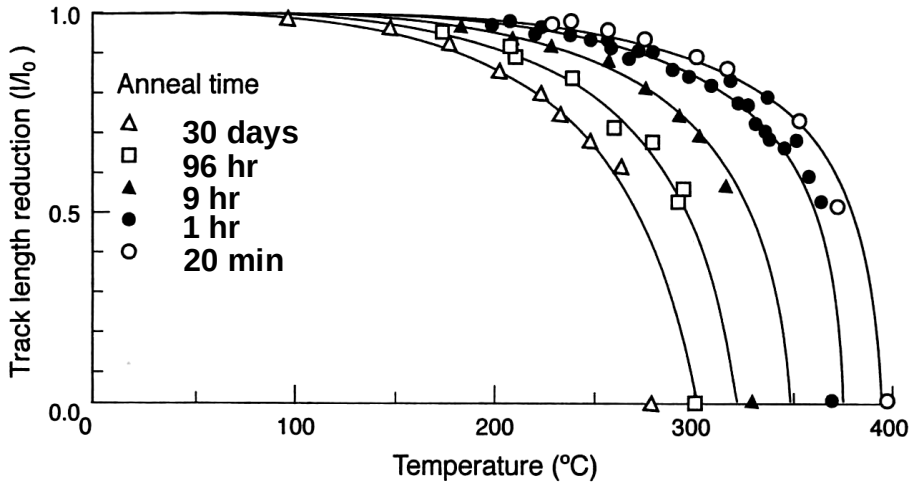

Figure 3.1 Laboratory annealing data for track length (Green *et al.* [8]) in Durango apatite and curves fitted using the fanning Arrhenius model (adapted from Laslett *et al.* [9]). The fission tracks are completely annealed around 360 ^{o}C for one hour.

On the other hand, atomic scale approaches can dramatically improve our understanding of the processes involved in track annealing. TEM studies of fission tracks in their latent or unetched state are now possible and can be used to unravel the microstructure of fission tracks, as well as the recombination processes of defects in the core region. However, there has been only a limited effort to investigate the annealing behavior of apatite fission tracks by TEM [10-12]. Paul *et al.* in 1992 made the first *in situ* TEM observations of fission track annealing in apatite at low temperatures on a

liquid nitrogen cooled cold stage [13]. Their radiolytic-thermal annealing experiments were induced by allowing the sample temperature increase from -175 ℃ to -74 ℃ while continuously exposing the sample to the electron beam [13]. However, thermal annealing experiments at high temperature were not conducted because they were not able to achieve a high temperature (>120^{o}C) in the TEM. In addition, they have also investigated furnace annealed samples by TEM and found that the population of tracks is not eliminated at 450 ^{o}C after 5 hours [12]. However, it is difficult to determine the degree of annealing because no comparison has been made of the same tracks before and after furnace annealing. In this study, the thermal annealing behavior of apatite fission tracks at high temperatures (up to 700 ℃) under *in situ* TEM have been completed. TEM micrographs of the same fission tracks before and after external furnace annealing have also been obtained.

3.2. Experiments

A greater track density was introduced into the naturally-occurring, hexagonal fluorapatite from Durango, Mexico by the thermal-neutron induced fission of ^{235}U in a nuclear reactor. Swift heavy ions irradiated samples were also prepared at the UNILAC-accelerator of the GSI Helmholtz Centre for Heavy Ion Research at Darmstadt, Germany. A small quantity of irradiated sample for TEM studies was crushed and dispersed ultrasonically in ethanol and a drop of suspension then deposited onto TEM copper-grids coated with holy carbon film. *In situ* thermal annealing experiments were performed in a

200 kV field emission gun JEOL 2010 TEM equipped with Gatan double tilt heating specimen holder with temperature up to 1000 ℃. This enabled us to directly observe high temperature fission track annealing behavior under TEM. The external thermal annealing experiments were performed in a Muffle furnace up to 730 ℃. A holy carbon film grid sample was sealed in a glass tube to protect it with argon gas from oxidization during the furnace annealing.

3.3. TEM observations of unetched fission track annealing behavior

3.3.1. Furnace annealing of bulk sample

Figure 3.2 shows a TEM micrograph of 2.2 GeV Au ion tracks in fluorapatite after furnace heating at 400 ^{o}C for 2 h in the air. A single crystal fluorapatite around 50 μm in thickness was irradiated by swift ions followed by furnace annealing. TRIM calculation shows that the whole thickness of the bulk sample can be penetrated by the swift ion along the *c*-axis of the apatite [14]. After furnace annealing, the bulk sample was crushed and then was placed on top of a holy carbon grid for TEM observation. As shown in Figure 3. 2, parallel unetched tracks irradiated by 2.2 GeV Au ions can still be seen after the annealing. This suggests that the swift ion tracks cannot be totally removed at 400 ℃ heating for 2 hours in the air. This is consistent with the finding of Paul. *et al.* that the population of unetched fission track in apatite is not eliminated after heating at 450 ℃ heating for 5 hours [12]. On the contrary, the etched fission tracks under optical microscopy were totally removed at 360 ℃ for 1 h [8]. Paul *et al.* believed that the degree of annealing determined by optical observation on etched tracks was not correlative to

that from TEM observations on unetched tracks [12]. They did not explain this since no further work was conducted.

It is impossible to tell whether these tracks are partially annealed or not annealed at all if no comparison is made of the tracks before and after thermal annealing. Without measuring the track length, one can estimate the degree of annealing by qualitatively comparing the morphological change of the same tracks before and after heating using the TEM. It is known that the accuracy of the average track length measurement can be improved by selectively measuring horizontally confined tracks under an optical microscope. However, the observable track lengths under TEM depend on the thickness and the orientation of crushed grain, which is always random. Therefore, it would be difficult to quantitatively determine the degree of annealing by measuring average track length with a TEM.

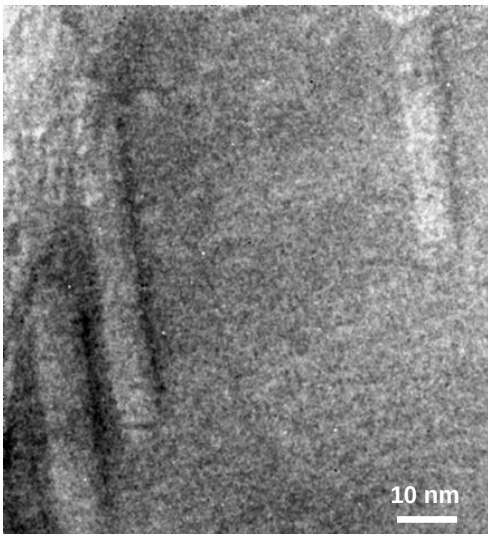

Figure 3.2 TEM image showing the 2.2 GeV Au induced tracks in apatite after furnace annealing at 400 ℃ for 2 h in the air.

3.3.2. *In situ* annealing under TEM

Although annealing studies of latent tracks at the nanoscale provide the basis for an improved understanding of the fading of etched tracks, only a very limited number of TEM investigations have been conducted up to now [12-13]. Numerous experiments on furnace annealing of etched fission track in fluroapatite have been carried out before, and the degree of annealing has been determined by measuring the average lengths of etched tracks [5, 8]. However, the length change of the same tracks could not be directly monitored. Similarly, although the annealing degree of the same tracks can be determined under TEM after external furnace heating, the dynamic process of annealing cannot be directly observed. Therefore, I have carried out *in situ* thermal annealing experiments on fission track by using TEM specimen-heating holder at high temperatures.

As we can see in the following experiments, the annealing behavior for individual tracks can be significantly different. The rate of track decay depends on the track's orientation relative to the hexagonal fluorapatite, its radius, and the radius uniformity along the track trajectory. Any difference in the three factors can cause different track morphologies on heating. In addition, the lengths of fission tracks that can be observed are usually less than 1 μm due to the limitation of TEM viewing screen. Therefore, the latent track observed by TEM can only reflect the annealing behavior of a portion of the track segment (less than 1 μm), as compared with the entire length (~16 μm), as in the etched tracks observed by optical microscopy.

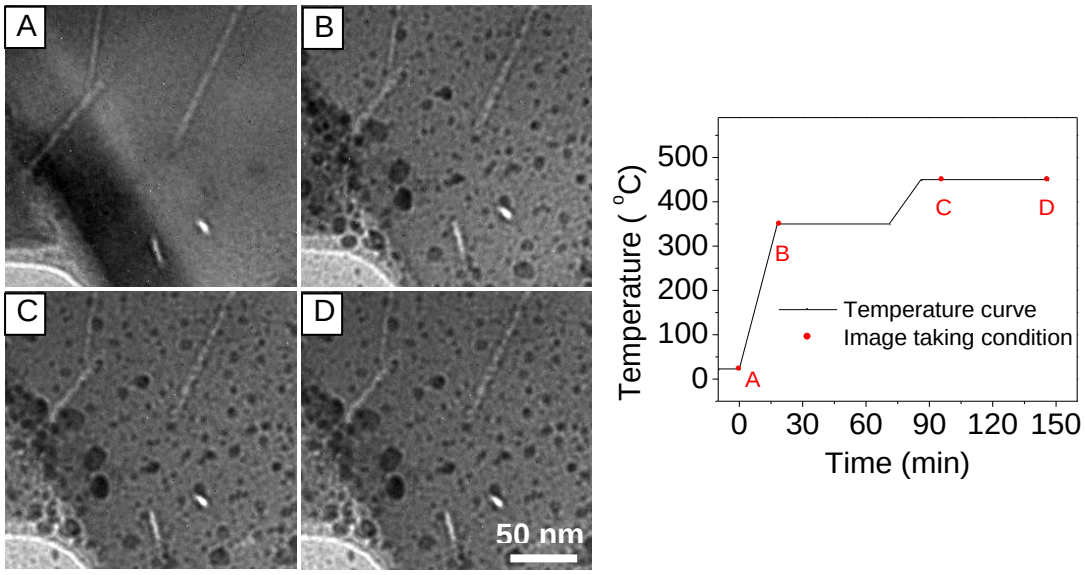

Figure 3.3 TEM images of *in situ* thermal annealing of apatite fission track: before heating (A) and during the heating (B-D); the right plot showing the temperature curve as a function of time and the temperature-time conditions at which each of the above images were obtained. After taking each micrograph, the beam was moved away in order to avoid electron beam annealing.

Figure 3.3 shows the TEM micrographs of *in situ* thermal annealing of apatite fission track before heating (A), and during the heating (B-D). The right plot the lower plot shows the temperature curve and the time-temperature points at which each of the above images were obtained. In between recording of the TEM images, the electron beam was moved away from the particle to avoid radiolytically-induced annealing. The electron dose rate is 3.9×10^{16} $e^-/cm^2.s$ and it takes less than 30 s to obtain each image. Low electron dose rate can be achieved by increasing the beam size and decreasing the magnification. In this way, the influence caused by electron irradiation can be minimized. As clearly shown in Figure 3.3, the fission tracks show no apparent fading under the TEM heating stage at 350 ℃ for 63 minutes and at 450 ℃ for an additional 60 minutes.

The *in situ* observations further confirm the fission tracks cannot be totally annealed at the maximum temperature of 450 ℃ for one hour. The dark spots scattered within the grain and carbon film are from the result of the deposition of copper from the TEM cooper grid.

In order to study the thermal annealing behavior, another *in situ* experiment has been performed with significantly increased temperature and time. Figure 3.4 shows a series of TEM images of apatite fission tracks before heating (A) and during heating (B-F). The lower plot shows the temperature curve and the time-temperature points at which each of the above images were obtained. As illustrated in Figure 3.4, the fission tracks in apatite keep unfading for more than 10 hours at 700 ℃. In the first annealing stage, the temperature was 400 ℃ and the sample was heated for 30 minutes. No obvious reduction of length has been observed for these fission tracks as shown by comparing Figures 3.4(A) and (B). The heating causes some copper spots to be uniformly deposited onto the surface, the carbon film and the apatite grain. The temperature was further elevated to 600 ℃ for an additional 35 minutes annealing in the second stage. Again, no apparent track annealing has been detected. Finally, the heating temperature was raised to 700 ℃ and held for 600 minutes as shown in Figure 3.4(D), (E) and (F) in the after the 10 hours annealing at 700 ℃ no significant change occurred in the morphologies of the tracks.

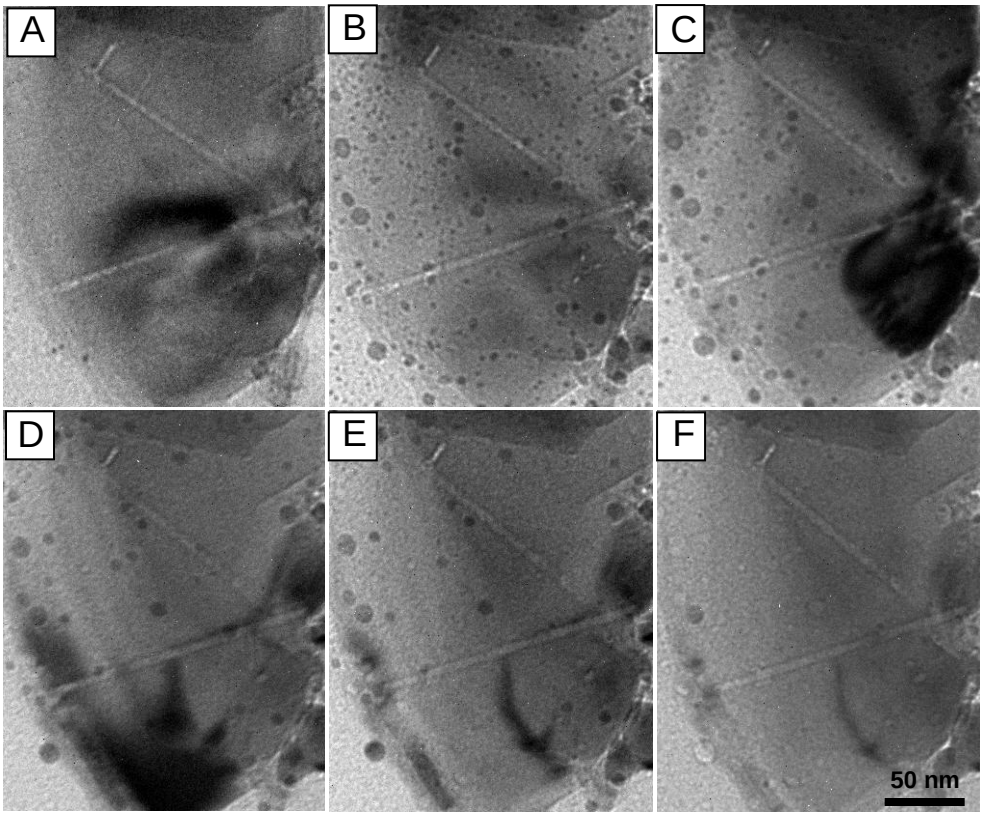

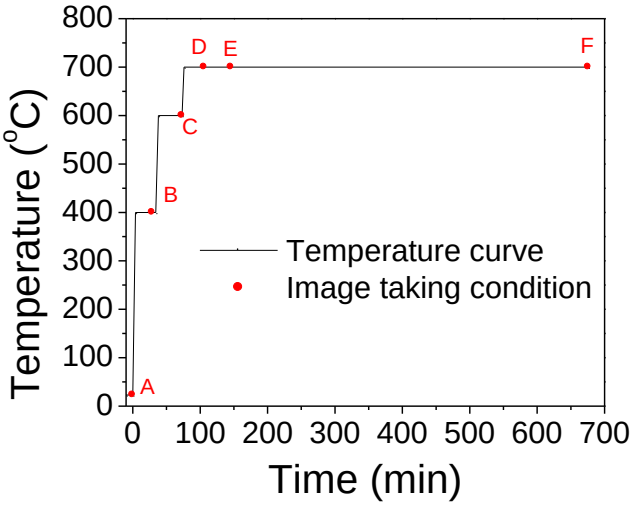

Figure 3.4 TEM images of *in situ* thermal annealing of apatite fission track before heating(A), and during the heating (B-F); the lower plot shows the temperature curve and the time-temperature points at which each of the above images were obtained. After taking each image was obtained, the electron beam was moved away from the sample area in order to avoid electron beam annealing.

It is very important to mention that once exposed to a continuous electron-beam-irradiation, the fission tracks that remained unchanged at 700 ℃ for 10 hours annealed rapidly. After 1 minute of electron irradiation at a dose rate of 6.0×10^{17} $e^-/cm^2.s$, one track shrank to one-half of its diameter. In Chapter IV, the entire process of electron beam-induced annealing of a fission track will be discussed in details. It is clear that fission tracks can be rapidly annealed under the electron beam, but they are not as sensitive to thermal annealing.

Another sequence of track shape change was obtained *in situ* at 700 ^oC as function of annealing time (Figure 3.5). Initially, the track radius either shrinks or grows along the ion trajectory without much periodicity in the intervals (Figure 3.5B, after 1 minute). After annealing times in excess of 53 minutes (Figure 3.5C), the fission track breaks into segments, randomly fragmented along the ion trajectory. The fragmentation of the track can be ascribed to the Brownian motion caused by the high mobility of atoms on the inside surface of the hollow track [15]. This is in clear contrast to the typical annealing mechanism of amorphous tracks, which shrink gradually due to the elimination of defects [1-2].

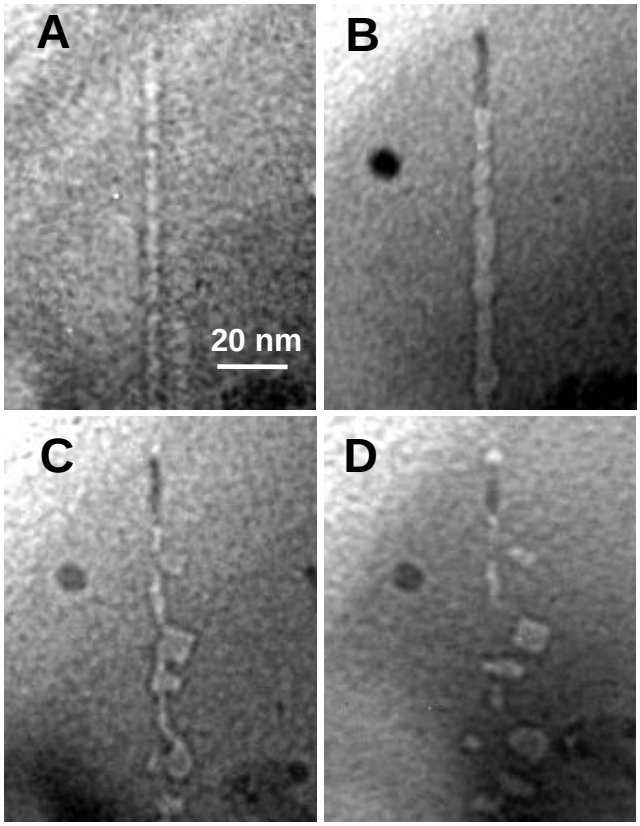

Figure 3.5 Thermal annealing. Bright field images show the morphological change of fission tracks before (A) and after 1(B), 53 (C) and 130(D) minutes heating at 700^{o}C in a TEM heating holder. After 130 minutes heating at 700^{o}C, a fission track fragments into smaller segments. The Brownian motion of the segments suggests that the structure of fission track is hollow.

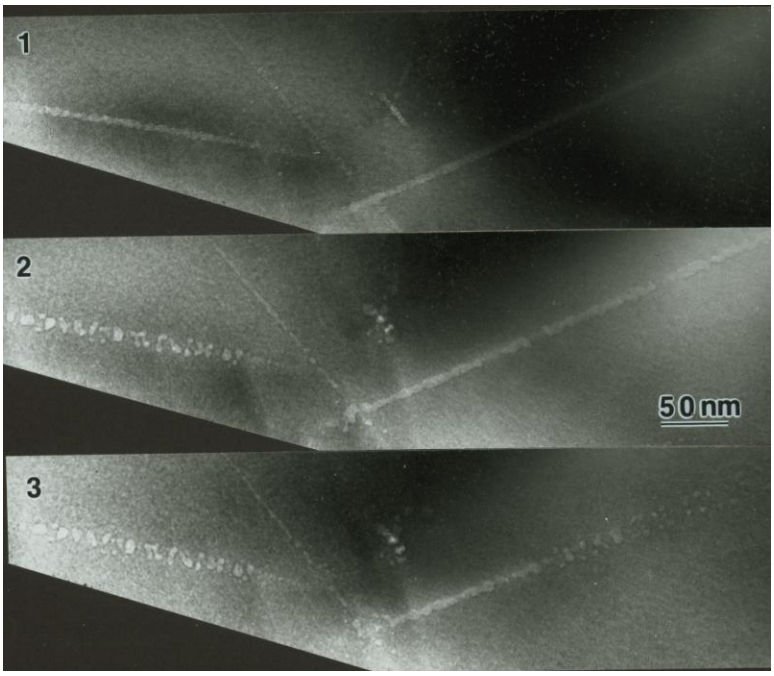

Figure 3.6 Bright-field TEM images of segmentation of neutron-induced fission tracks in fluorapatite during electron beam irradiation at liquid nitrogen temperature. The images were taken by Prof. L.M. Wang. Apparently, content within the tracks was mobile and fragmented under the electron beam. This is consistent with a fluid (gas-filled) core rather than an amorphous solid in the track.

The fragmentation of track segments has also been observed when the neutron-induced fission tracks in fluorapatite are subjected to electron beam irradiation (Figure 3.6). The images were acquired at liquid nitrogen temperature in order to avoid rapid electron beam damage to the matrix. The tracks become thicker in the radial direction as is apparent in stage 2. Comparing the images from the three stages shows that the content within the tracks was mobile. The fission tracks fragment into spherical segments in all directions under electron beam irradiation in order to lower the total surface are due to their irregular morphologies. These results demonstrate that both the electron beam

irradiation and thermal treatment can enhance the mobility of atoms, leading to the Brownian-type of motion of the fragmented segments.

In another *in situ* thermal annealing experiment, the fragments of some fission tracks were found to move along [0001] direction of hexagonal fluorapatite at 700 ^{o}C, which reflects the underlying preferred diffusion path of atoms along specific crystallographic orientations (Figure 3.7). This preferential motion of fission-track segments may influence the results on etched fission tracks for dating, such as the introduction of an anisotropic length bias [16].

As will be discussed in Chapter IV, electron beam irradiations on fluorapatite cause bubble formation and their elongation along the *c-axis*. The bubbles form gradually in apatite matrix, elongating along the [0001] direction with increasing dose. However, the fragmentation of the fission track that is aligned most closely to the [0001] direction was significantly slower than that of the track almost perpendicular to the [0001] direction. The [0001] direction favors the transport of fluorine atoms because of a large channel in the structure. Therefore, the tracks perpendicular to *c-axis* would break-up more easily; whereas the tracks or the bubbles parallel to *c-axis* would prefer to elongate rather than breaking up.

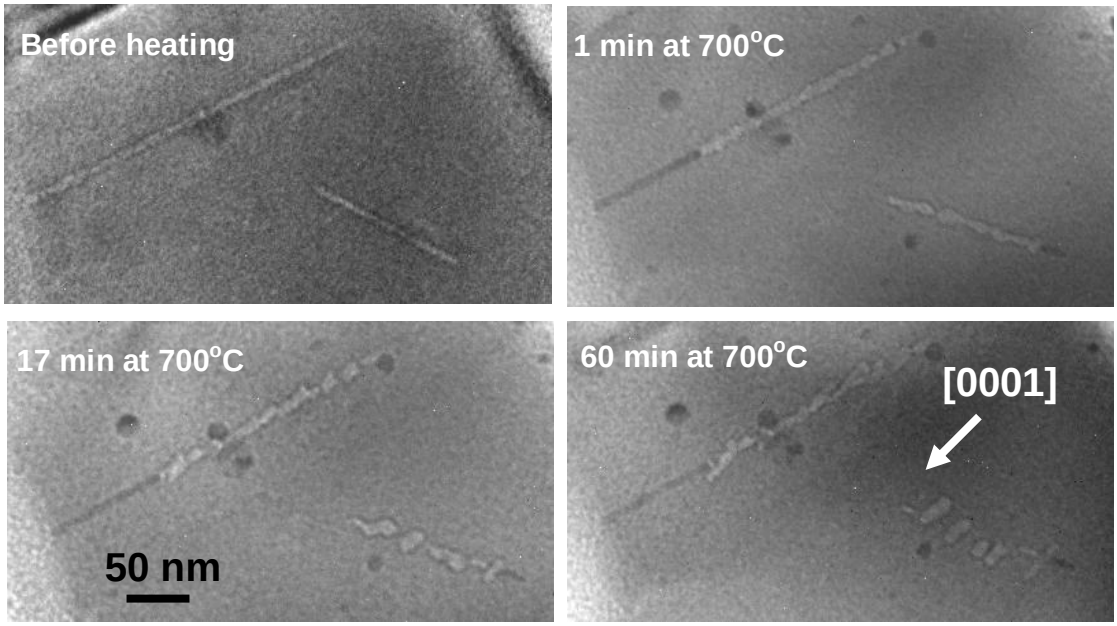

Figure 3.7 *In situ* TEM images showing the preferential motion of fission track segments along [0001] of fluorapatite during heating at 700°C.

3.3.3. Observation of the same fission track after *ex-situ* annealing

Figure 3.8 illustrates the same fission tracks before and after thermal treatment in a furnace at 400°C for 2 hours. The apatite with neutron-induced fission tracks was crushed and put onto a holy carbon grid for TEM observation. After obtaining the first set of images, the sample on the carbon grid was removed from TEM and sealed in a glass tube filled with 1 atm Ar for furnace annealing. After the heat treatment, the sample was returned to the TEM to obtain images of the same tracks after annealing. In order to compare the morphological change of the tracks before and after furnace annealing, marks were made to find the same tracks.

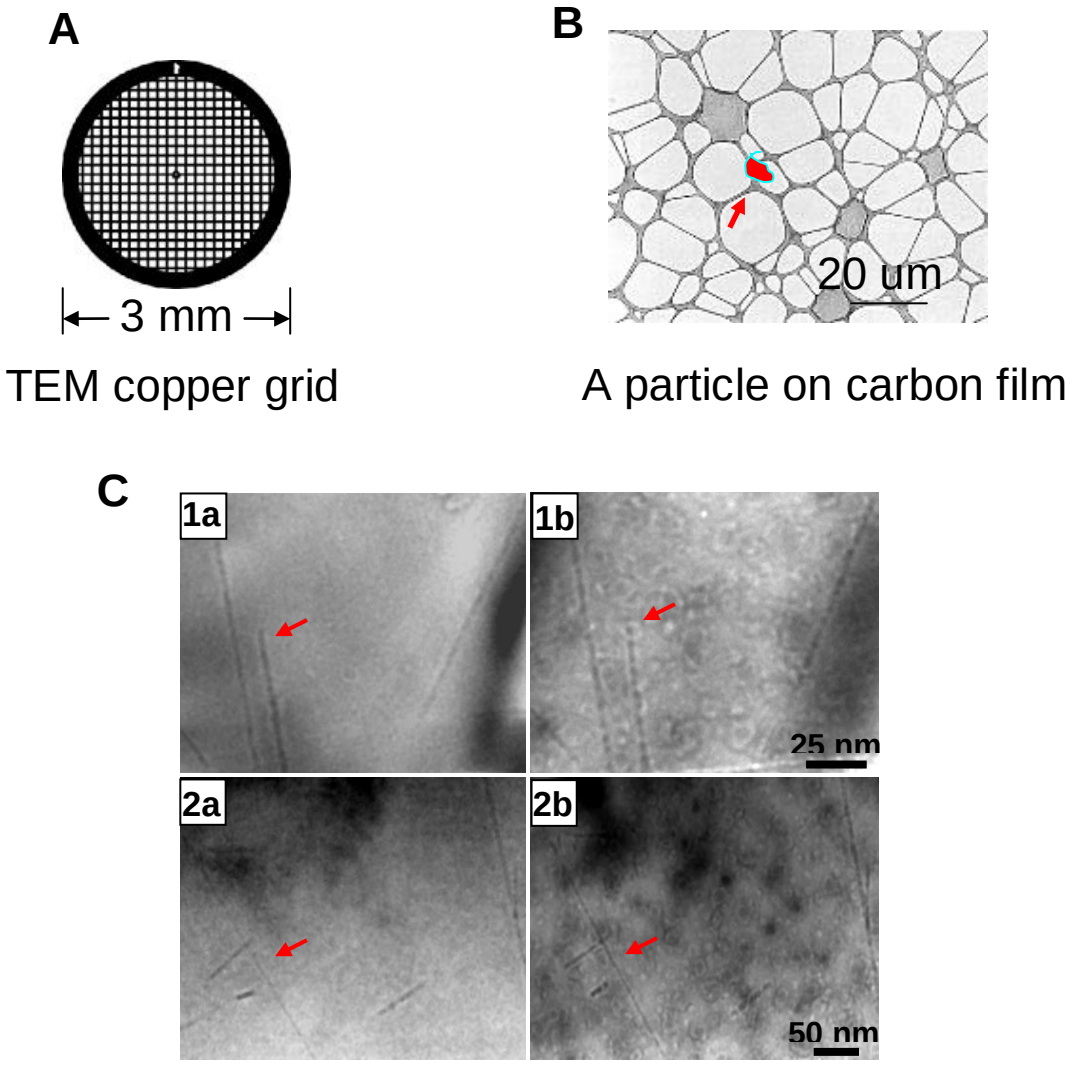

Figure 3.8 The same unetched fission tracks in fluroapatite on the carbon film can be found by making marks in the TEM copper grid. (A) A copper grid, (B) particle on carbon film, (C) TEM images of fission tracks before furnace heating (1a), and (2a), and corresponding images after heating (1b), and (2b), respectively. The sample was sealed in a glass tube filled with 1 atm pressure Ar before being heated at 400 ℃ for 2h.

As shown in Figure 3.8, two locations are given to show the morphological changes of the same fission tracks. After heating, the same tracks show no significant fading. However, some changes in the relative position or relative distance of tracks

might be noticed. This is because the zone axis of a grain on the carbon film might tilt at high temperature although the grain remains in the same location after the heating. In addition, some spots are found depositing on the surface of carbon film, as well as fluorapatite grains. EDS analysis shows these spots are copper deposition from the TEM copper grid during the heating. This external thermal annealing experiment further confirms fission tracks would not be totally removed at 400 ℃ for 2h, contrary to etched tracks being totally removed at 360 ℃ for 1 h [7].

The annealing temperature was increased to 700 ^{o}C in another *ex situ* thermal annealing experiment to examine for possible track morphological change. The TEM images before and after *ex situ* furnace heating the same fission track in fluorapatite show an obvious segmentation with periodic spacing occurring after 2 hours (Figure 3.9). In addition to the periodic segmentation, the total chain volume shrinks significantly. This result is still totally different from the common assumption that fission tracks shrink gradually at high temperature due to recrystallization of the amorphous core to the crystalline state [2, 17], which is believed to completely remove the etched tracks after annealing at 360 ℃ for 1 hour [18].

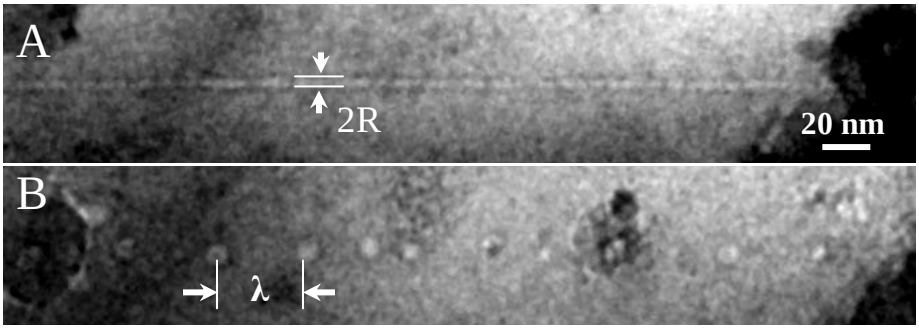

Figure 3.9 Furnace heating induced track segmentation. Regular segmentation is observed after *ex situ* furnace heating a fission track at 700°C for 2h. A, bright field image of a fission track. B, bright field image of the same fission track after furnace heating the powder sample. The sample was sealed in a tube filled with 1 atm Ar. The same fission tracks in fluorapatite can be found under TEM by the register marks made on the copper grid.

The spontaneous, self-organized disintegration (or segmentation) of an empty fission tracks at elevated temperature is driven by Rayleigh Instability. A harmonic perturbation of a cylindrical void in a solid or a cylindrical solid rod results in the disintegration into a row of spherical droplets spaced ~ 8.89R in an idealized situation *via* surface diffusion [19-20]. The morphological change of fission tracks during annealing from cylindrical into spherical shape is energetically favorable because the total surface area of the track decreases while the total volume remains unchanged. According to Rayleigh instability, the decay rate is very sensitive to the track radius [19] therefore any deviation from that of a strict cylinder along the track may cause a segmentation of tracks with the lack of periodicity as observed by TEM (Figure 3.5b). The Brownian motion of the empty segments further expedites the irregularity of the segmentation at high temperature. Similar to this thermo-driven disintegration, radiation-

induced annealing also results in a segmentation of tracks due to beam-enhanced diffusion processes.

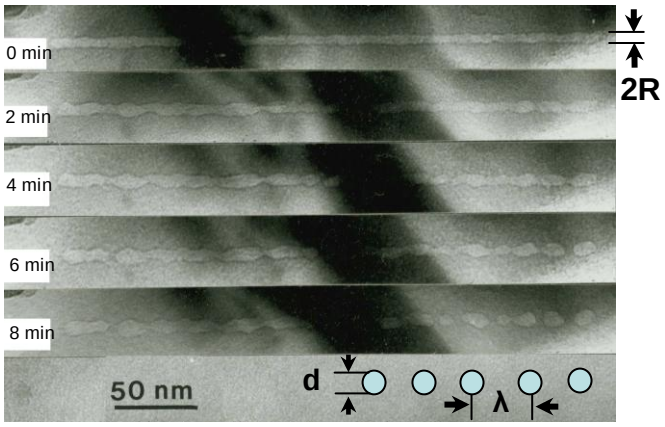

Figure 3.10 Rayleigh instability. Bright-field TEM micrographs of segmentation sequence of a fission track in fluorapatite with time during radiolytic annealing under a 200 keV electron beam at liquid nitrogen temperature. The images were provided by Prof. L.M. Wang. The inset represents the scheme of the sphere and spacing, as modeled in [20].

Electron-beam exposure of fission tracks in fluorapatite at liquid nitrogen temperature also leads to a regular break down of tracks (Figure 3.10).The track radius under electron beam either shrinks or grows along the ion trajectory initially but with much more periodicity in the intervals (Figure 3.10), which is due to the uniformity of the initial radius along the track. Further electron irradiation leads the fission track a gradual decay into separate droplets with intervals around 6.9~9.5*R* (*R*, initial track radius: 2.6 nm). The change of the total chain volume is less than 1% of that of the initial fission track. This clearly evidences the Rayleigh instability as being the driving force for track

fragmentation during the annealing process. The less fragmentation of segments along the ion trajectory due to the reduced Brownian motion at low temperatures also contributes the regular segmentation as observed during electron-beam irradiation.

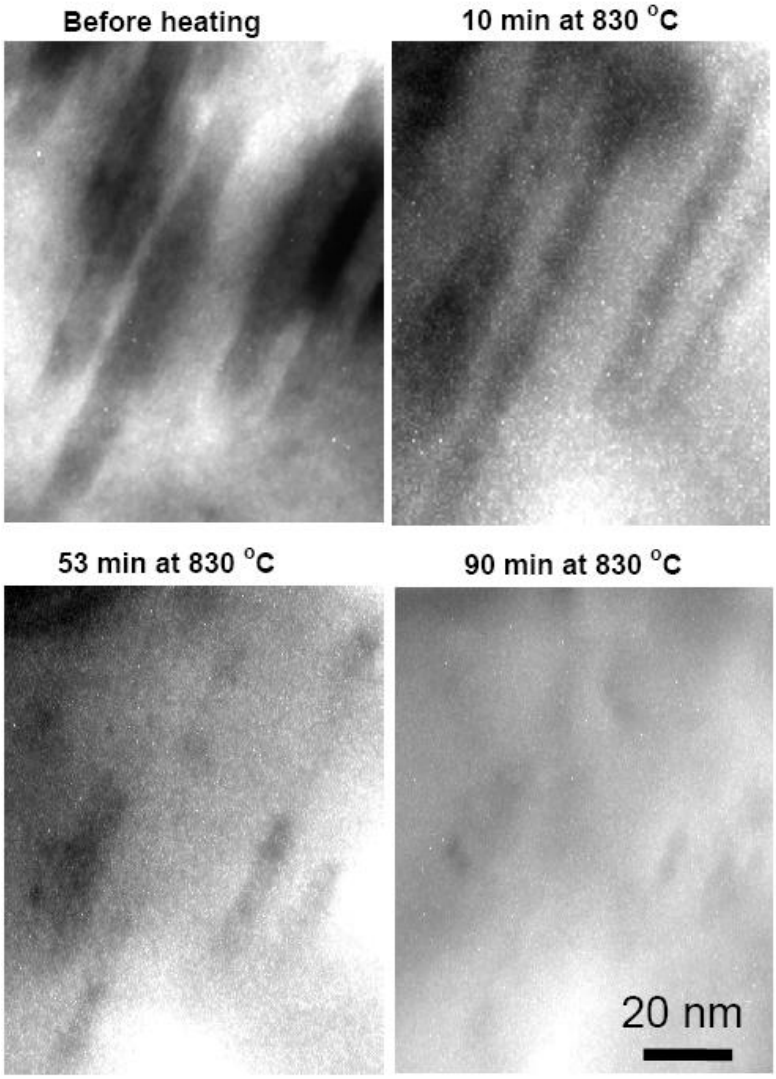

Figure 3.11 *In situ* thermal annealing of amorphous tracks in zircon created by 2.2 GeV Au ions. The side-by-side images show the tracks as a function of increasing time. The amorphous tracks became fading and eventually disappeared due to defect elimination.

At this stage, many types of thermal annealing experiments on hollow fission tracks in fluorapatite have been conducted, which show the fragmentation of tracks due to the high mobility and high surface tension of hollow features. However, there have been very few thermal annealing experiments of tracks previously completed. The fragmentation of tracks was first reported by Paul *et al.* in an *in situ* thermal-radiolytic annealing experiment (*i.e.*, the combined effects of thermal treatment and electron beam irradiation) of fission tracks in apatite [13], and later in an *ex situ* annealing experiment of fission tracks in the same material, entirely induced by thermal treatment [12]. However, the fragmentation has never been explained as being due to the hollow structure of fission tracks in fluorapatite. In this research, an *in situ* thermal annealing of amorphous tracks in zircon at 830^{o}C for up to 90 minutes has been conducted in order to see the difference in the thermal annealing behavior between amorphous and hollow tracks. Significantly different to hollow tracks, amorphous tracks became narrower and eventually disappeared due to defects elimination (Figure 3.11). No spontaneous segmentation and random motion of track segments were observed. The comparison of the thermal annealing behavior of hollow tracks in apatite and amorphous tracks in zircon reflects their significant differences in their internal structure.

3.4. Discussion

3.4.1. The difference between etched method and unetched method

As mentioned before, optical microscopy observations have shown that the etched fission tracks in fluorapatite were completely annealed at approximately 360 ℃ after one

hour [5, 7]. Green el al. believed that the effects of temperature dominate over time in determining final fission track parameters, with an order of magnitude increase in time (from several minutes to 500 days) being equivalent to a ~ 10 ℃ increase in temperature [4]. Therefore, the time spent for complete elimination of fission tracks at 700 ℃ would be instantaneous if this interpretation of the process were true. However, latent fission tracks at 700 ℃ for 10 hours are not annealed (Figure 3.4), which is significantly different from those from optical microscopy observations. Some might argue that the vacuum environment or lack of oxygen in TEM may be responsible for the lack of fading of fission tracks at high temperature. However, the fission tracks have not totally removed by the *ex situ* furnace annealing experiments (Figure 3.9).

The differences in the annealing behavior between the TEM observations of latent tracks and the optical microscopy observations of etched tracks should be clarified. The differences may be used to explain the significant contradictions in interpretation. First, the definition of the degree of annealing for these two methods is inconsistent. The annealing degree in etched tracks is determined by the measured lengths under optical microscope. However, latent tracks annealing is determined by direct observation of morphological change under TEM. For prolonged heating, the morphologies of the tracks may change, or the chemical composition of the core may change. These types of changes may not be detected by TEM observations. Whereas, such changes might be significant enough to change the etch rate of a track, and this would be evident by use of optical microscopy. Second, *in situ* thermal annealing under TEM makes it possible to directly observe the morphological changes in several specific fission tracks. The

experimental procedures are much simpler and thus help to reduce the errors mainly from the chemical etching. On the contrary, the annealing process of the etched tracks cannot be directly monitored and the measured lengths of etched tracks depend not only on the structure of latent tracks, but also the etching time, and the composition and concentration of etchant. The structural information in etched tracks is removed by etching; therefore, they are unable to reflect a detailed picture of recombination process. Finally, *in situ* observations of fission track annealing are usually localized because of the limitation of the grain size and the view field of TEM. Compared to the whole track length up to 16 μm observed by optical microscope, the fission tracks that can be observed under TEM are usually less than 1 μm. Individual tracks may have different annealing behaviors resulting from different track radius, orientation or track uniformity along a track, which provide a general view of the entire annealing process. However, multiple measurements at different locations under TEM can be used to address this issue.

3.4.2. Influence of β decay on fission track annealing over geological time

As discussed above, the fission tracks which remained unchanged at 700 ℃ for 10 hours are able to be easily annealed by electron irradiation. This means the annealing of fission tracks might be very sensitive to electron beam irradiation. However, there is accumulation of ionizing irradiation due to the β-decay from natural uranium and thorium over the geological time. Meldrum et al. also found that electron irradiation can induce the crystallization of the damaged apatite, which is contradictory to traditional thought

that β decay may weakly enhance the damage accumulation process [21]. The annealing effects of electron irradiation due to β-decay from natural uranium and thorium on fission tracks might not be neglected.

In the following, the energy depositions from 200 keV electrons in TEM and from β-decay from natural U and Th have been compared in order to see if the two depositions are comparable from the view of energy. Misdaq *et al*. have calculated the total dose rate (mrads a^{-1}) in a considered ceramic sample, due to the nuclei of the uranium and thorium families by,

$$D_G^{\beta} = D_{SP}^{\beta}(U).C(U) + D_{SP}^{\beta}(Th).C(Th) \quad (3.2)$$

where $D_{SP}^{\beta}(U)$ and $D_{SP}^{\beta}(Th)$ (mrads a^{-1} ppm^{-1}) are the specific annual β doses deposited by 1 ppm of ^{238}U and 1 ppm of ^{232}Th inside a ceramic sample [22]. For the Durango apatite sample in the work, $C(U)$ and $C(Th)$ are estimated as 15 and 200 ppm, respectively [23]. Since there are no data available for annual β-dose inside apatite, *i.e.*, $D_{SP}^{\beta}(U)$ and $D_{SP}^{\beta}(Th)$, they are estimated by the values of the ceramic material used in Misdaq's paper as 70 and 13 mrads a^{-1} ppm^{-1}, respectively [22]. Then the annual dose can be calculated by Equation 3.2 as 3,650 mrads a^{-1}.

The age of Durango apatite is estimated as 30 Ma, therefore the total energy deposition from β decay from natural U and Th is

$$3{,}650 \text{ mrads } a^{-1} \times 30 \text{ Ma} = 1.1 \times 10^{6} \text{ Gy}. \quad (3.3)$$

On the other hand, the stopping power of electron irradiation on apatite ($Ca_5P_3O_{12}F$, density=3.12g/cm3) at 200 keV can be calculated as follow:

$$\frac{dE}{dx} = \frac{4\pi e^4 n}{mc^2\beta^2}[\ln\frac{mc^2\tau\sqrt{\tau+2}}{\sqrt{2}I_{ex}} + F(\beta)], \tag{3.4}$$

$$F(\beta) = \frac{1-\beta^2}{2} + \frac{1}{2(\tau+1)^2}[\frac{\tau^2}{8} - (2\tau+1)\ln 2], \tag{3.5}$$

where at 200keV,

$$\beta = v/c = 2.086/2.988 = 0.698, \tag{3.6}$$

$$\tau = E/mc^2 = \frac{200}{512} = 0.3906, \tag{3.7}$$

n, target electron density, I_{ex} the mean electron excitation energy of the target is 157.6 eV.

$$\frac{dE}{dx} = 7.08 \text{ MeV/cm} = 7.08\times10^{-2} \text{ eV/Å}. \tag{3.8}$$

In this way, the energy deposition in 1 second electron irradiation at a dose rate of 6.0×10^{17} $e^-/cm^2.s$ can be obtained as:

$$Gy = \frac{dE/dx \times t}{\rho} = \frac{6.0\times10^{17}\times7.08\times10^{-2}\times1.6\times10^{-19}\times1\times10^3\times10^8}{3.12} \text{ (J/kg)}$$

$$= 2.2\times10^8 \text{ Gy}. \tag{3.9}$$

This means the total energy deposition, that is 1.1×10^6 Gy, from β-decay accumulated within 30 Ma is only comparable to 5×10^{-3} s electron irradiation under 200 keV TEM. The dose rate for β-decay (~ 3.2 $e^-/cm^2.s$) is 17 orders of magnitude smaller

than that of electron irradiation (~6.0×10^{17} $e^-/cm^2.s$) under 200 keV TEM. Therefore, the annealing effects of electron irradiation due to β-decay from natural uranium and thorium might be neglected based on the estimation of energy deposition by electron irradiation.

3.4.3. Mechanisms of track annealing for hollow fission tracks

Models of track annealing have long been limited to empirical fits to etched track length data without any consideration of the atomic-scale track structure [2, 5, 24]. Due to the lack of direct experimental evidence, track annealing was described as an atom-by-atom damage recovery of an amorphous phase [1, 17], resulting in the gradual reduction of the observed etched track length as shown in Figure 3.12A. Etched tracks completely anneal at ~360 ℃ within one hour [5, 18]. This is in clear contrast to the results of annealing experiments on latent tracks in this study; remnants of tracks in the form of isolated segments are still present at 700 ℃ for annealing times in excess of 130 minutes. The obvious discrepancy suggests that in addition to the shrinkage, the discontinuity of fission tracks possibly impedes chemicals from entering into the hollow tracks for further etching, and then significantly reduces the etched length [25-26]. As shown in Figure 3.12B**,** the damage recovery in a track is driven by Rayleigh instability, Brownian motion or preferential motion of empty (or gas filled) segments, in addition to the shrinkage of hollow track by thermal emission of vacancies to the surrounding solids.

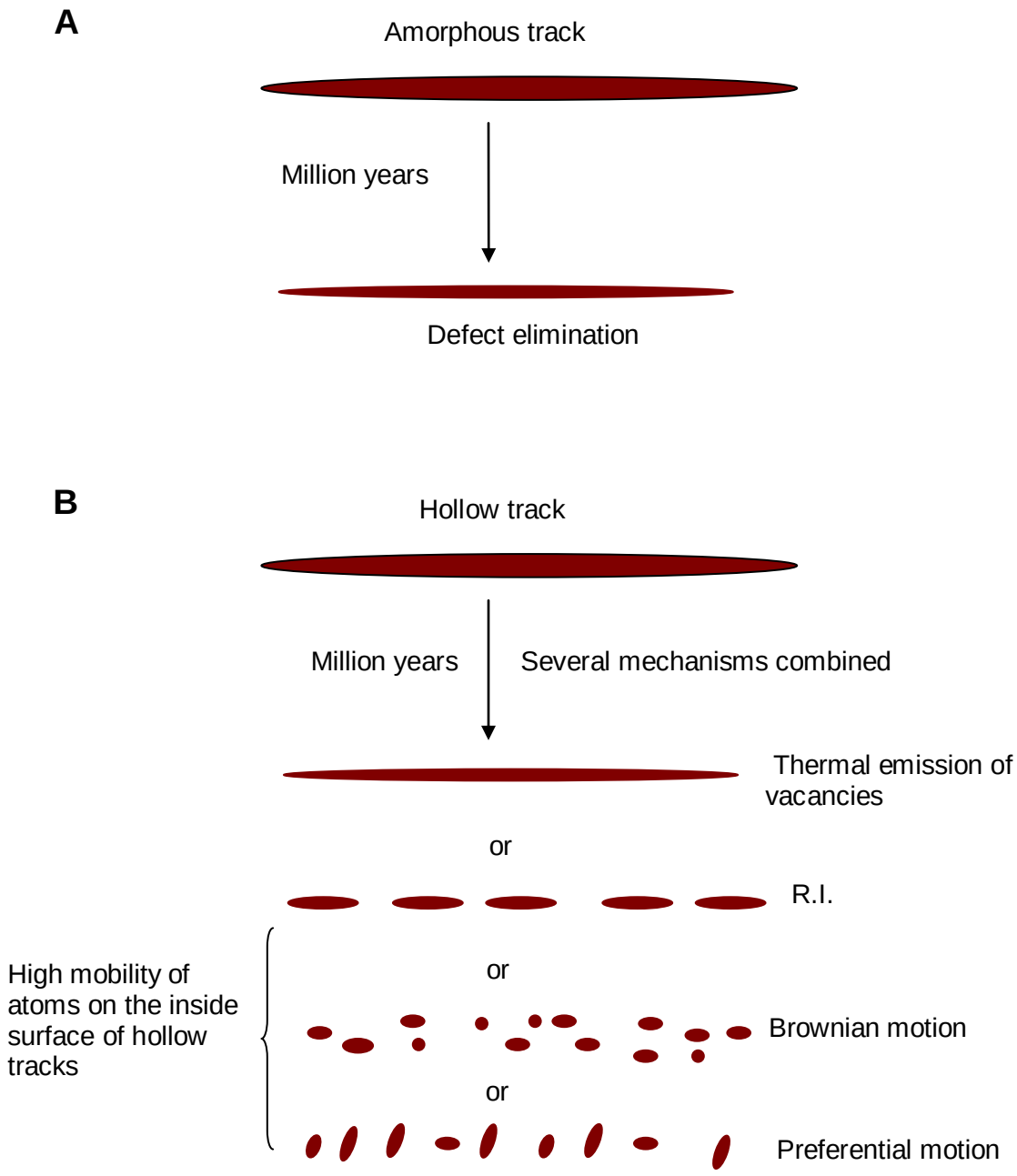

Figure 3.12 Comparison of fission track annealing mechanisms with amorphous core (A) and with hollow core (B). The etchability of hollow fission tracks is controlled by gradual shrinkage and the discontinuity of fission tracks, which is either caused by Rayleigh instability, by Brownian motion or by preferential motion of track segments due to high diffusivity of atoms on the inside surface of hollow tracks.

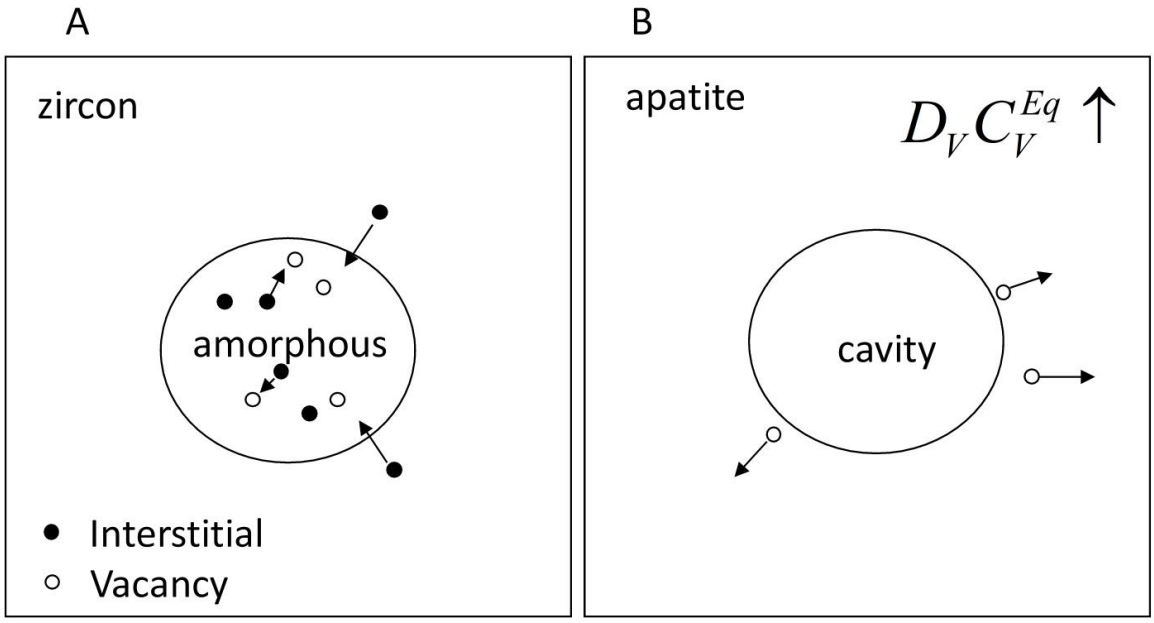

Figure 3.13 Comparison of shrinkage mechanism in fission tracks with an amorphous core *versus* with a hollow core. (A) The amorphous track shrinks by restoring the amorphous core atom-by-atom. (B) The hollow track shrinks by thermo-emission of vacancies from the hollow track to the matrix since the significant increase in the product of equilibrium of vacancy concentration and vacancy diffusivity at high temperatures.

In addition, the shrinkage of a hollow fission track is significantly different from the shrinkage of amorphous track which restores the damaged core to a crystalline structure by a recrystallization process (Figure 3.13A). According to void-growth/shrinkage law [15], the thermal emission of vacancies from voids to surrounding solid can be neglected at low temperatures due to the low equilibrium vacancy concentration in the solid. Whereas, at high temperatures, the voids tend to evaporate rather than grow because the rapid increase in the product of vacancy diffusion

coefficient and the equilibrium vacancy concentration causes thermal emission of vacancies from voids (Figure 3.13B).

The etched experiments and their empirical models suggest that isochronal annealing of etched track in fluorapatite can be characterized by two distinct processes, *i.e.*, a progressive shrinking of the track from each end, which is dominant at lower temperatures and a rapid breakup of the track into discontinuous portions, which is dominant at higher temperatures [18, 24]. In comparison, isothermal annealing of etched track in fluorapatite show an initially rapid reduction of length followed by a very much slower decrease at longer times [27]. However, the fundamental processes involved in the annealing of latent tracks in fluorapatite are still unclear because the initial structure of the latent tracks is lost after chemical etching, and there have been no systematic studies of atomic-level nature of an unetched track [2]. Despite of great number of empirical models, very few physical models are available to describe fission track annealing due to lack of atomic-level understanding in this field.

Fleisher *et al.* [28] and Green *et al.* [29] suggested a physical model that track etchability is controlled only by the extent to which the density of damage within the track region is greater than some threshold levels. The track shrinks from each end because the damage density is highest in the middle of the track, where the fission occurred and corresponding stopping power is highest, and decreases toward each end. The gaps in ecthability within tracks might result from random fluctuations in damage density, possibly accentuated by annealing. This model can qualitatively explain all

aspects of the observed annealing behaviors of fission track in fluorapatite, but it is not quantitative due to lack of data on the track structure, the ecthability thresholds and the quantitative effects of annealing [29]. Carlson postulated a physical model for which the thermal annealing produces reductions of track length initially by defect elimination and subsequently accelerated reductions by segmentation of tracks [2]. His model was not based on any knowledge of the atomic structure of the track and an experimental observation of annealing, but again was a simple fit to micro-scale measurements of etched tracks [29-30].

The observations of regular track segmentation and the understanding of track segmentation by Rayleigh instability can improve the physical models with quantitative description of track annealing in fluorapatite. The segmentation of latent fission tracks at elevated temperature, possibly together with the shrinkage of fission tracks due to thermal emission of vacancies to the solid, causes a gradual reduction of etched length of fission tracks. Tracks anneal much faster initially from each end of the track and subsequently slower toward center, which coincides with decreasing track radius from the middle toward each end of the track [27]. The regions near each end anneal faster due to smaller radius than those near center, because the effective track radius induced by fission fragments (with initial energy 50-100 MeV) has an approximate linear relation to $S_e^{1/2}$, the square root of energy loss per depth [31], and the characteristic time scale for the Rayleigh instability of voids is proportional to R^4 (R, track radius) [32]. Paul et al. have observed the gaps (up to 50 nm) due to track segmentation under electron beam [13].

However, they have not explained the relation of the two "gaps" (20~100 times difference in length) because preservation of gaps in annealing and chemical etched tracks is thought to require that the original gap be > 1 μm in length [13]. The relation of two "gaps" can be explained by Rayleigh instability. Due to the large track length and radius ratio (l/R ~5000), the radius change can be neglected within a short range, *e.g.*, 1 μm, despite that track radius really depends on the energy loss per depth. Therefore, many (*e.g.* 20~100) small gaps would be formed almost simultaneously in that short range (~1 μm) during the segmentation of the track into separated droplets according to Rayleigh instability (as shown in Figure 3.12). Within the normal etching time (20~60s) for fission tracks in fluorapatite, the small gaps would merge into large gaps (> 1 μm) due to the delay or even the termination of etchant into the hollow track. Meftah et al. propose that chemical etching of latent tracks is inefficient until the energy loss per unit depth is above a threshold level when the separated segments begin to overlap into a cylinder [26], which is consistent with the proposal that a line of small segmented gaps (up to 50 nm) would cause the etchant to be inefficient. In this way, the ecthability threshold in Fleischer's model can be replaced with analytic determination of the threshold radius by the $S_e^{1/2}$ relation [31], since the ecthable length (~16 μm) is shorter than the total range (~ 22 μm) of a track induced by two fission fragments.

All thermal annealing experiments suggest that the degree of annealing determined by optical microscopy of etched apatite fission tracks is not the same as that observed during the annealing of latent fission tracks as determined by TEM studies. Our data show clearly that track annealing is a very complex process with several underlying

mechanisms. The hollow structure of latent tracks is a key to developing an adequate physical description for the fading mechanisms of fission tracks in apatite at elevated temperatures.

In summary:

- Latent fission tracks after heating at 700 ^{o}C for 10 hours can be still observed by TEM, which contradicts the observations of etched fission tracks that were completely removed by annealing at 360 ^{o}C for 1 hour. However, due to the random orientation and limited length of latent track, the annealing behavior for different tracks may be significantly different. Any difference in the track orientation, track radius and the track uniformity along the track trajectory can cause different track morphologies to result from annealing.

- The segmentation of tracks and the Brownian, or preferential motion of track segments during thermal annealing further confirm the hollow structure of fission tracks in fluorapatite.

- The discontinuity of fission tracks, in addition to the shrinkage, prevents chemicals from entering into the hollow tracks for continued etching, and this significantly reduces the etched track length. The high diffusivity of atoms on the inner surface of the hollow fission tracks causes the discontinuity of fission tracks.

- The shrinkage of hollow fission tracks results from thermo-emission of vacancies from the cavities to surrounding solids instead of recrystallization of an amorphous track to the crystalline state.

- The preferential motion of atoms along *c*-axis causes the more rapid annealing of fission tracks perpendicular to *c*-axis.

- These new insights provide the basis for a track annealing model at the atomic scale, which will be of major importance for fully understanding the length reduction of the etched fission tracks used for age-dating.

1. R.L. Fleischer, *Fission tracks in solids - production mechanisms and natural origins.* J. Mater. Sci., 2004. **39**: p. 3901-3911.
2. W.D. Carlson, *Mechanisms and kinetics of apatite fission-track annealing.* Am. Mineral., 1990. **75**: p. 1120-1139.
3. A.J.W. Gleadow, I.R. Duddy, P.F. Green and J.F. Lovering, *Confined fission track lengths in apatite: a diagnostic tool for thermal history analysis.* Contrib. Mineral. Petrol., 1986. **94**: p. 405- 415.
4. P.F. Green, I.R. Duddy, G.M. Laslett, K.A. Hegarty, A.J.W. Gleadow and J.F. Lovering, *Thermal annealing of fission tracks in apatite 4. Quantitative modelling techniques and extension to geological timescales.* Chem. Geol., 1989. **79**: p. 155-182.
5. K.D. Crowley, M. Cameron and R. Schaefer, *Experimental studies of annealing of etched fission tracks in fluorapatite.* Geochimica et Cosmochimica Acta, 1991. **55**(5): p. 1449-1465.
6. T. Tagami and P.B. O'Sullivan, *Fundamentals of fission track thermochronology.* Rev. in Mineralogical & Geochemistry, 2005. **58**: p. 19-47.
7. P.F. Green, I.R. Duddy, A.J.W. Gleadow, T. P.R. and G.M. Laslett, *Thermal annealing of fission track in apatite, 1. A qualitative description.* Chem. Geol., 1986. **59**: p. 237-328.
8. P.F. Green, I.R. Duddy, A.J.W. Gleadow and T. P.R., *Fission-track annealing in apatite: track length measurements and the form of the Arrhenius plot.* Nucl. Tracks. Radiat. Meas., 1985. **10**: p. 323-328.
9. G.M. Laslett, P.F. Green, D. I.R. and G. A.J.W., *Thermal annealing of fission track in apatite, 2. A quantitative analysis.* Chem. Geol., 1987. **65**: p. 1-13.

10. P.B. Price and R.M. Walker, *Observations of charged-particle tracks in solids.* J. Appl. Phys., 1962. **33**: p. 3400-3406.
11. P.B. Price and R.M. Walker, *Electron microscope observation of a radiation-nucleated phase transformation in mica.* J. Appl. Phys., 1962. **33**: p. 2625-2628.
12. T.A. Paul, *Transmission electron microscopy investigation of unetched fission tracks in fluorapatite-physical process of annealing.* Nucl. Tracks. Radiat. Meas., 1993. **21**: p. 507-511.
13. T.A. Paul and P.G. Fitzgerald, *Transmission electron microscopic investigation of fission tracks in fluorapatite.* Am. Mineral., 1992. **77**: p. 336-344.
14. SRIM, *http://www.srim.org/SRIM/SRIM2006.htm*. 2006.
15. D.R. Olander, *Fundamental Aspects of Nuclear Reactor Fuel Elements*. 1976, Springfield, Virginia: National Technical Information Service, U.S. Department of Commerce. 236-239, 490-491.
16. R.A. Donelick, *Crystallographic orientation dependence of mean etchable fission track length in apatite: An empirical model and experimental observations.* Am. Mineral., 1991. **76**: p. 83-91.
17. R.L. Fleischer, *Fission tracks in solids - production mechanisms and natural origins.* Mater. Sci., 2004. **39**: p. 3901-3911.
18. P.F. Green, I.R. Duddy, A.J.W. Gleadow, P.R. Tingate and G.M. Laslett, *Thermal annealing of fission tracks in apatite 1. A qualitative description.* Chem. Geol., 1986. **59**: p. 237-253.
19. A.M. Glaeser, *Model studies of Rayleigh instabilities via microdesigned interfaces.* Interface Sci., 2001. **9**: p. 65-82.
20. F.A. Nichols and W.W. Mullins, *Surface-(interface-) and volume-diffusion contributions to morphological changes driven by capillarity.* Trans. Met. Soc. AIME, 1965. **233**: p. 1840.
21. A. Meldrum, L.M. Wang and R.C. Ewing, *Electron-irradiation-induced phase segregation in crystalline and amorphous apatite: A TEM study.* Am. Mineral., 1997. **82**(9-10): p. 858-869.
22. M.A. Misdq, K.Fahde, H.Erramli and A. Mikdad, *A new method for evaluating annual alpha and beta dose rates in different ceramic samples by using solid state nuclear track detectors.* Radiat. Phys. Chem., 1997. **50**: p. 293-297.
23. J.W. Boyce and K.V. Hodges, *U and Th zoning in Cerro de Mercado (Durango, Mexico) fluorapatite: Insights regarding the impact of recoil redistribution of radiogenic He-4 on (U-Th)/He thermochronology.* Chem. Geol., 2005. **219**: p. 261-274.
24. G.M. Laslett, P.F. Green, I.R. Duddy and A.J.W. Gleadow, *Thermal annealing of fission track in apatite, 2. A quantitative analysis.* Chem. Geol., 1987. **65**: p. 1-13.
25. Villa F., Grivet M., Rebetez M., Dubois C., Chambaudet A., Chevarier A., Martin P., Brossard F., Blondiaux G., Sauvage T. and T. M., *Damage morphology of Kr ion tracks in apatite: Dependence on dE/dx.* Radiation Measurements, 1999. **31**: p. 65-70.
26. A. Meftah, F. Brisard, J.M. Costantini, M. Hage-Ali, J.P. Stoquert, F. Studer and M. Toulemonde, *Swift heavy ions in magnetic insulators: A damage cross section velocity effect.* Phys. Rev. B, 1993. **48**: p. 920.

27. P.F. Green, I.R. Duddy and G.M. Laslett, *Can fission track annealing in apatite be described by first-order kinetics?* Earth and Planetary Science letters, 1988. **87**: p. 216-228.
28. R.L. Fleischer, P.B. Price and R.M. Walker, *Nuclear Tracks in Solids*. 1975, Berkeley: University of California Press. 31.
29. P.F. Green, G.M. Laslett and I.R. Duddy, *Mechanisms and kinetics of apatite fission-track annealing-Discussion.* Am. Mineral., 1993. **78**: p. 441-445.
30. K.D. Crowley, *Mechanisms and kinetics of apatite fission-track annealing-Discussion.* Am. Mineral., 1993. **78**: p. 210-212.
31. G. Szenes, *Analysis of tracks induced by cluster ions in CaF_2.* Phys. Rev. B, 2000: p. 14267.
32. T.K. Gupta, *Instability of cylindrical voids in alumina.* J.Am. Cer. Soc., 1978. **61**(5-6): p. 191-195.

CHAPTER IV

RADIOLYTIC ANNEALING OF FISSION TRACKS IN FLUORAPATITE

4.1. Background

Fission tracks are widely used to date the mineral age and to reconstruct the thermal history of the mineral [1-2]. The track lengths are shortened at elevated temperatures therefore can be measured under optical microscope to determine the thermal history of the minerals. Extensive empirical models have been developed to mathematically fit the curve of track length reduction related to temperature and time [3-5]. Laboratory thermal annealing experiments by etching methods have shown that fission tracks perpendicular to *c-axis* in apatite are usually shorter than those parallel to *c-axis* [6-7] . However, very few atomic scale studies have been done to investigate the microstructure of tracks and the physical mechanism of track annealing, especially the orientation effect on the track annealing [8-11].

In the previous chapters, it is revealed that fission tracks in volatile fluorapatite contain a hollow core that might be filled with several gaseous phases instead of an amorphous core as commonly assumed [12]. *In situ* TEM observations of thermal annealing behaviors under TEM showed that fission tracks cannot be totally annealed

even at 700 ^{o}C for 10 hours. That is significantly different from the etched tracks totally removed at 360 ^{o}C for 1 hour. The thermal annealing behaviors are actually combined complex processes. It should be noted that most of the annealing behaviors have also observed in the electron beam induced annealing experiments. The hollow nature of fission tracks in apatite is the key point to understand the annealing mechanisms induced by thermal treatment or electron irradiation.

Similar to the thermally enhanced diffusion, the diffusion of defects or gaseous phases in solids, especially in the volatile rich materials, is significantly enhanced by electron beam irradiation, resulting in the bubble-like behaviors of fission tracks [13-16]. In this chapter, I will further demonstrate *in situ* TEM observations of electron beam irradiation induced orientation effects on the track annealing, and on the formation and mobility of elongated bubbles along *c-axis* in apatite at high temperature. I will separate the four mechanisms, *i.e*., radiolytic shrinkage, decomposition, morphological change and orientation effects under electron irradiation. The combined effects of these mechanisms on the track annealing and the motion and the elongation of bubbles will be discussed.

4.2. Experiments

Both neutron induced fission tracks and swift ion induced tracks in fluroapatite have been used to investigate radiolytic annealing behaviors in a JEOL 2010 operated at 200 kV with a field emission gun. The naturally-occurring, hexagonal natural minerals

fluorapatite from Durango, Mexico are put in a reactor for producing thermal-neutron induced tracks. Parallel swift ion tracks have also been created by 1.54 GeV Xe ions or 710 MeV Bi ions along the [0001] direction of fluorapatite minerals from Durango. A small quantity of crushed sample containing either fission tracks or swift ion tracks for TEM studies is then dispersed ultrasonically in ethanol and a drop of suspension then deposited onto a holey-carbon-coated copper-grid and allowed to air dry. *In situ* electron beam annealing experiments have been carried out at different temperatures and different dose rates. High temperature, room temperature and low temperature are achieved by using hot stage, normal stage and cold stage, respectively. The different dose rates have been chosen by altering the beam size and the magnification under TEM.

4.3. Results and discussion

In situ electron beam annealing experiments have been performed at a dose rate of 6.0×10^{17} $e^-/cm^2.s$ using a JEOL 2010 TEM with a Gatan heating stage. As shown in Figure 3.4 in Chapter 3, the powder sample was first heated at 700℃ for 10 hours in TEM. The 10 hours heating produced no obvious changes of the tracks before radiolytic annealing. However, as clearly revealed in Figure 4.1, the fission tracks show significant bubble formation and rapid track breakage once under continuous electron beam exposure at 700℃. The bubbles are forming and enlarging gradually in apatite matrix. Unlike the bubbles at room temperature keeps spherical shape under electron beam irradiation [16], the bubbles at 700 ℃ changed their shape from sphere to cylinder, elongating along the [0001] direction with increasing dose. This eventually results in the

formation of 1-D parallel cylindrical bubbles about 5~10 nm in diameter and 10~50 nm in length.

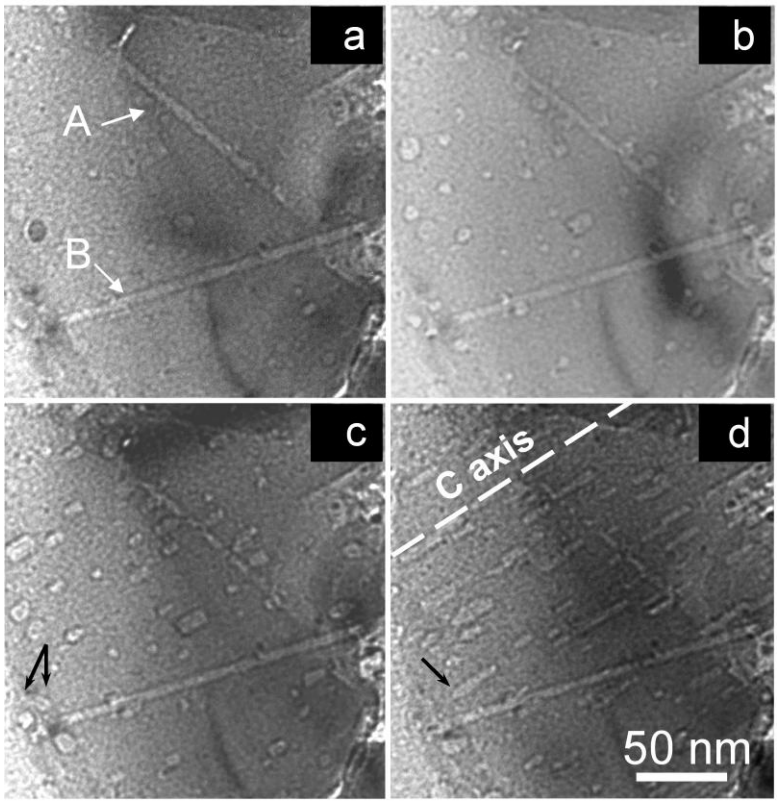

Figure 4.1 Low electron dose rate (6.0×10^{17} $e^-/cm^2.s$) irradiation at 700°C causes the fission tracks to fade rapidly at a dose of (a) 0, (b) 3.6×10^{19}, (c) 1.4×10^{20} and (d) 1.2×10^{21} e^-/cm^2. Electron beam exposure also leads bubbles to form and elongate along [0001] direction. The marks in (c) and (d) show one bubble coalescences with another and moves further away from original place.

The video recorded during the *in situ* observation reveals the dynamic formation of the elongated bubbles. The liquid-droplet-like motion clearly demonstrates the bubbles are gas-filled. The video shows the bubbles have a strong tendency to move along either positive or negative direction of *c-axis*. The two-way-motion of bubbles along *c-axis* can

therefore cause either coalescence of two bubbles into a bigger one or breakage of a bubble into two smaller ones in opposite directions. It should be mentioned that some bubbles move a long distance from their original place if the motion along one direction is significantly preferential to another. As is also marked in Figure 4.1 (c) and (d), the video clearly shows that one small bubble coalescences with another bubble and moves further.

In addition, as shown in Figure 4.1, further continuous electron beam exposure leads the fission tracks to fade at 700 ℃. However, the breakage of the fission track (A) that is closer to the [0001] direction is significantly slower than that of the track (B) almost perpendicular to the [0001] direction. The track (A) breaks up into several segments after 32 minutes irradiation, *i.e.* at a dose of 1.15×10^{21} e^-/cm^2. On the contrary, after 32 minutes irradiation, the track (B) is found to shrink only a little bit in the track diameter, without any significant breakup.

It is very important to mention that the elongation and preferential motion of track segments along [0001] direction have been also observed in thermal annealing experiments (Figure 3.7 in Chapter 3). The similarity of bubbles and fission tracks in the preferential motion either induced by electron irradiation or thermal treatment further confirm the hollow nature of fission tracks.

The elongation and the mobility of bubbles and fission tracks are resulted from the combined mechanisms. Simply speaking, the radiolytic induced annealing process

decreases the volume of the tracks or the bubbles by electron enhanced-emission of vacancies or gases from the hollow tracks to matrix. On the other hand, the radiolytic decomposition process increases the volume through the release of gaseous phases into the damaged tracks or bubbles. The exchange of gases or vacancies between tracks and matrix causes random or preferential motions of track segments. Thirdly, the pure morphological change is energy favorable to lower the total surface of the track, while would it keep the total volume of tracks unchanged according to ideal Rayleigh instability. At last, the orientation effects on bubble elongation and fission track annealing is attributed to the preferential diffusion along *c-axis* of hexagonal fluorapatite. The unbalanced process of growth and elimination of bubbles along *c-axis* under electron irradiation causes the preferential motion of bubbles.

4.4. Mechanisms

4.4.1. Radiolytic annealing

Figure 4.2 illustrates continuous electron beam exposure at a low dose rate (7.61×10^{17} $e^-/cm^2.s$) at room temperature causes the annealing of 1.54 GeV Xe ion tracks along [0001] direction of fluorapatite. The whole process of gradual track fading has been recorded in a video. The average track diameter as well as corresponding error has been measured and plotted.

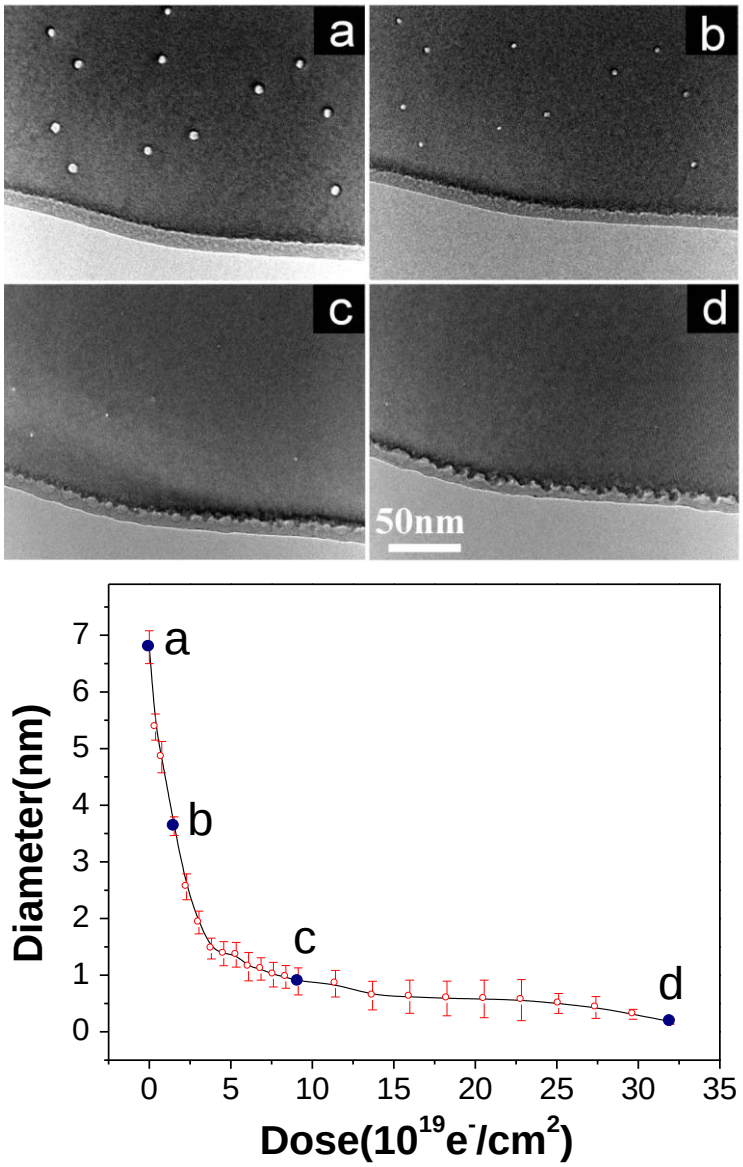

Figure 4.2. Top view TEM micrographs shows low dose rate (7.61×10^{17} $e^-/cm^2.s$) electron exposure at room temperature causes the fading of 1.54 GeV Xe ions tracks in fluorapatite at dose of (a) 0, (b) 1.5×10^{19}, (c) 9.1×10^{19}, (d) 3.2×10^{20} e^-/cm^2. The average diameter as a function of electron dose is plotted and the doses at which the pictures were taken are marked by a, b, c and d, respectively.

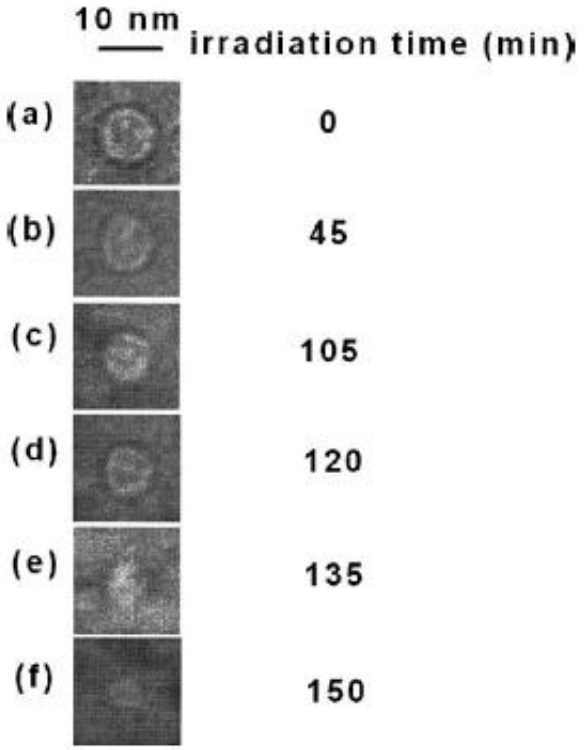

Figure 4.3 *In situ* TEM micrographs showing the shrinkage of a single nanocavity as induced by a 300 keV electron beam irradiation at room temperature(From Figure 1 in [17]).

It is clearly shown, once the irradiation commences the average diameter drops quickly from initial 6.8 nm to 3.6 nm at dose of 1.5×10^{19} e^-/cm^2, and then the fading rate decreases dramatically when the dose reaches to about 5×10^{19} e^-/cm^2. Similarly, the track density decreases faster at the early stage. The track density drops from initial 6.8×10^{10} tracks/cm^2 to 1.88 $\times10^{10}$ tracks/cm^2 at a dose of 9.1×10^{19} e^-/cm^2 at the earlier stage. However, some tracks cannot be totally eliminated even when the dose reaches to 3.2×10^{21} e^-/cm^2.

The vacancy emission process from the matrix likely attributes the annealing of fission tracks or swift ions tracks under continuous electron beam irradiation [17-18]. At high temperature, there are more spaces in the matrix to occupy vacancies emitting from the cavities since the significantly increase in the product of the equilibrium of vacancy concentration in the matrix and the vacancy diffusivity [18]. In the ion irradiation cases, the internal shrinkage of nano-cavities only occurs when the matrix surrounding the cavities becomes preferentially amorphized so that the amorphized region can take up the shrunk volume by dissolving a higher concentration of vacancies emitted from the cavities [17, 19]. As shown in Figure 4.3, the thermal or electron irradiation induced shrinkage of nanocavities was also reported in Si where the cavities are believed to act as sinks for Si interstitials [19-20]. More dangling bonds and higher compressive strain at negatively curved inner wall of cavities provide a larger driving force for getting interstitials from the surrounding matrix (which is equal to the emitting vacancies from cavities to the preferentially amorphized matrix) than those at flat surface or at positive curvature of nanoparticles [17, 19-20]. *In situ* observations by HRTEM show the gradual shrinkage of an individual hollow track in fluorapatite induced by 2.2 GeV Au ions under electron beam irradiation (Figure 4.4). Under HRTEM, the newly formed amorphized region has been observed around the hollow track core, which provides the spaces for the vacancies emitting from the hollow track to the amorphized region. The originally hollow track is almost covered by newly formed amorphizied matter at late stages.

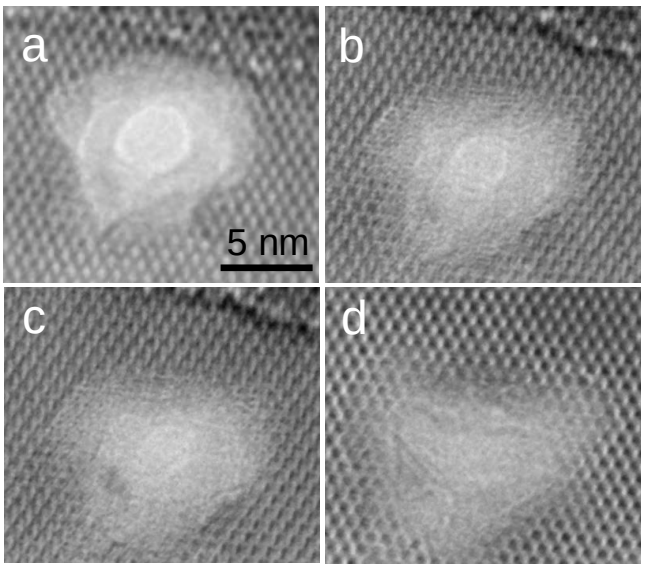

Figure 4.4 Shrinkage of a hollow track under electron beam. Top view HRTEM micrographs of a single track in fluorapatite produced with 2.2 GeV Au ion beam. Electron exposure at room temperature causes gradual track fading (images (a) through (d) are recorded within 2 minutes time intervals).

Meldrum et al. have calculated the temperature rise due to electron-beam irradiation on fluorapatite using Fisher's model [16, 21]. The calculated temperature rise varies between 13 and 69 ^{o}C when the current density is in the range of 0.3~1.6 nA/cm^2. The calculated values by Meldrum are considered as a maximum [16], therefore the actual temperature rise is estimated to be less than 26 ^{o}C at a typical current of 0.5 nA/cm^2. Note, fission tracks did not anneal at 700 ^{o}C for 10 hours (Figure 3.4), however an electron beam-irradiation at low dose rate results in the totally recovery of fission tracks in fluorapatite at room temperature (Figure 4.2). This means that the track annealing is not resulted from the electron-beam heating but the radiolysis process.

Instead of heating the sample, the electron irradiation significantly enhances the vacancy diffusion from hollow tracks to the matrix. The energy transferred from electron beam lowers the energy barrier for defect migration. The stopping power of 200 keV electron beam irradiation on apatite can be calculated as, 0.07 eV/Å. The energy that can be transferred to an F vacancy along *c-axis* is estimated to be 0.3 eV/atom, which is comparable to the normal migration energy [22]. The electron irradiation enhanced diffusion in turn results in the volume decrease of hollow tracks.

4.4.2. Radiolytic decomposition

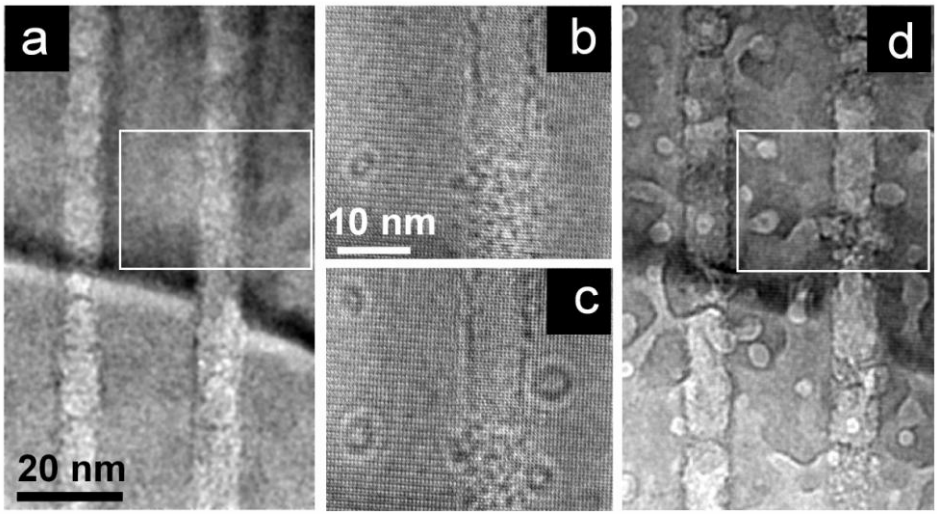

Figure 4.5 The micrographs show the sequence of high dose rate (1.9×10^{19} $e^-/cm^2.s$) electron irradiation of fluroapatite induced by 710 MeV Bi ions. Low magnification images of (a) and (d) reveal the starting and final conditions, respectively. High-resolution images of (b) and (c) are taken from white frame marked region, which show the gradual formation of bubbles from the matrix.

The radiolytic decomposition of fluorapatite under TEM is highly possible to release gaseous phases into vacuum, or into the vacancy-rich regions to form bubbles. The EELS studies by Zenser *et al.* have shown that the electron beam sensitive MgF_2 can be decomposed and the volatile F_2 may leave the specimen [23]. Meldrum *et al.* observed the electron irradiation on fluorapatite leads to the formation and the coagulation of bubbles, which suggests the bubbles are gas-filled [16].

Figure 4.5 shows a sequence of electron irradiation on 710 MeV Bi ion tracks in fluorapatite at a high dose rate (1.9×10^{19} $e^-/cm^2.s$) at room temperature. As is clearly revealed in Figure 4.5, a high dose rate electron irradiation causes the breakup of tracks, but also produces voids or bubbles around the tracks and in the surrounding matrix. The HRTEM images show dynamic process of the formation and growth of bubbles under electron irradiation at room temperature. Unlike at high temperature that the bubbles elongate along *c*-axis, the bubbles at room temperature keep a spherical shape at prolonged irradiation. This suggests that high temperature enhances the orientation effects on the preferential diffusion.

The EDS analysis by Meldrum *et al*. showed that the bubble induced by electron decomposition is enriched in phosphorous while is significantly deficient in calcium [16]. As discussed in Figure 2.11 of Chapter 2, the EDS experiment of chemical composition change under electron irradiation at room temperature has been carried in a fluorapatite single crystal under TEM. The *in situ* EDS results of compositional change of fluorapatite

shows that under electron beam irradiation, the volatile rich fluorapatite can be decomposed and the element F is more ready to release, followed by O and P. However, it should be realized that the highest concentration of elements in bubble might not be F because the concentration of F in original fluorapatite (Ca_{10} $(PO_4)_6F_2$) is lowest. Therefore, it is concluded that the gaseous phases due to radiolytic decomposition also release to the voids and the core of the damaged tracks then increase their volume. Morphological change

Rayleigh instability analysis has been applied to investigate the morphological change of apatite fission tracks under TEM at low temperature. Rayleigh instability is known as harmonic perturbation of a cylindrical solid rod or a void in solid results decay into a row of spherical droplets via surface diffusion during the annealing [24-25]. An infinite cylinder of original radius R is subjected to periodic perturbation in the radius, of wavelength λ and amplitude α (of initially infinitesimal α_0), which can be given by a decay law of,

$$\alpha = \alpha_0 \exp[\mu t]. \tag{4.1}$$

The amplification factor,

$$\mu = \frac{\delta_s D_s \gamma_s \Omega}{R^4 kT}[(\frac{2\pi R}{\lambda})^2 (1-(\frac{2\pi R}{\lambda})^2)], \tag{4.2}$$

where δ_s is surface thickness, D_s surface diffusivity, γ_s surface energy, and Ω atomic volume. If any longitudinal perturbation wavelength is bigger than the circumference

($\lambda > 2\pi R$), the cylinder is unstable, *i. e.* such perturbation increases in amplitude with time. The wavelength at which the perturbation reaches a highest decay rate and dominates the evolution can be therefore obtained by calculating the maximum value of the amplification factor,

$$\lambda_{Max} = \sqrt{2}(2\pi R) = 8.89R. \quad (4.3)$$

In order to observe the morphological change of fission tracks according to ideal Rayleigh instability, *i.e.*, $\lambda_{Max} \sim 8.89R$, it is important to keep the change of the total volume of the fission track as small as possible. Therefore, low temperature is chosen to inhibit vacancy diffusivity, by which the total volume might decrease in the radiolytic shrinkage process. On the other hand, the dose rate is kept at low as possible to prevent raidiolytic decomposition, by which the released bubbles into fission track might cause the increase of total volume of fission track.

Very regular morphological change of fission track in fluorapatite according to Rayleigh instability has been observed under low dose rate electron irradiation at liquid nitrogen temperature (Figure 4.6(a)). At the beginning of irradiation, the track width increases as shown in Stage 2 and the periodic fluctuations of track radius develops. This stage is followed by the segmentation of the fission track as the irradiation continues. The segments are approaching to a row of spherical droplets with periodic intervals, which can be well understood by Rayleigh instability. In an ideal condition of Rayleigh instability, the total volume keeps unchanged. However, the morphological change from a long cylinder to spherical droplets is energy favorable because the total surface

decreases gradually via surface diffusion. Therefore, the enhanced diffusivity of defects by electron beam irradiation is also favorable for a pure morphological change without any alteration of track volume. However, as is discussed above, the electron irradiation might either increase the volume of track by radiolytic decomposition or decrease the volume by radiolytic annealing, which leads to the fluctuation of track volume as the extent of annealing increases.

In order to precisely describe the volume change at each stage, the track diameters at an interval step of 1.32 nm have been measured in a magnified image as revealed in Figure 4.6(b) and (c). In this way, as plotted in Figure 4.6(d)., the average diameter and the total volume of the track at each stage are also calculated by assuming that the track is composed of many small cylinders with a height of 1.3 nm. The average track diameter increases 17.3% first from 5.2 nm at Stage 1 to 6.1 nm then decreases gradually to 5.4 nm at Stage 5 under further irradiation. Similarly, the total volume of the fission track is raised 38.4% from original 9223 nm^3 to 12769 nm^3 at Stage 2, and then drops to 11615 nm^3 at Stage 5. It is known that pure morphological change is unable to increase the volume of the track. The obvious volume increase at Stage 2 suggests the bubbles decomposed of fluorapatite under electron irradiation fill into the track and increase its volume. While the decrease of track volume at followed stages illustrates the radiolytic shrinkage process is dominated at the late stages.

It is needed to mention that in most of the cases, irregular segmentation can be observed in electron beam induced annealing in fluorapatite due to Brownian motion of track segments (Figure 3.6 in Chapter 3.). Any imbalance between the random motion of atoms on the inner surface of hollow tracks causes the Brownian motion of track segments [18].

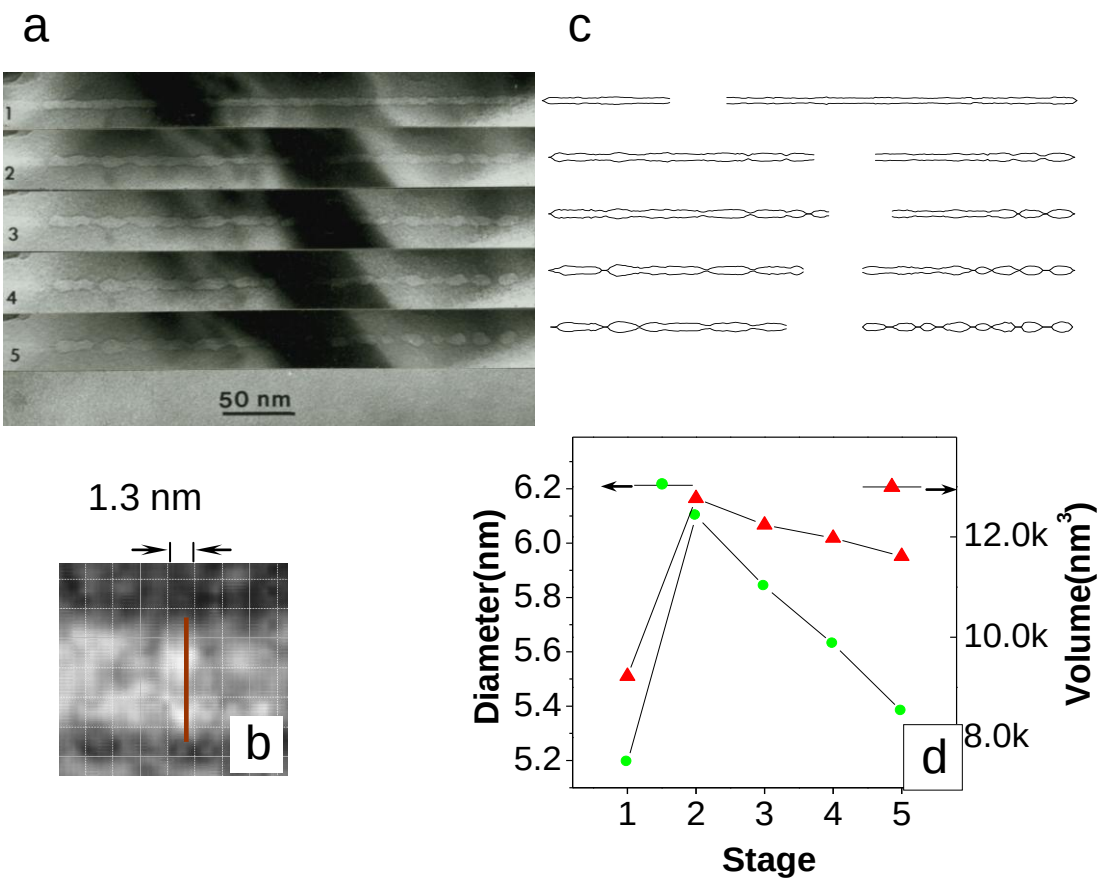

Figure 4.6 Sequence of segmentation of neutron-induced fission track in fluorapatite under low dose rate electron beam irradiation at low temperature. (a) TEM micrographs (provided by Prof. L.M. Wang), (b) An enlarged image showing the process of measuring the track diameter at an interval step of 1.3 nm, (c) A reconstructed digital track by measuring the diameter along the track at an interval step of 1.3 nm, (c) Average track diameter and total track volume at each stage.

4.4.3. Orientation effects

As discussed above, the orientation effect has been observed under electron beam irradiation at high temperature: bubbles are found forming and elongating to [0001] direction in fluorapatite, and the fading rate of fission tracks along *c-axis* is slower than that perpendicular to *c*-axis. In fission track dating experiments, the crystallographic effects due to thermal treatment have been also observed by optical microscopy [7] . Gleadow *et al.* believed the *c-axis* of apatite favors the transport of diffusing defects, that is, $V_c > V_a$ because the F and Ca triangles form open channels in this direction as shown in Figure 4.7 (a) [26-28] . The orientation effects have only observed on thermal annealing of fission tracks in apatite, and radiolytic annealing of tracks in apatite at high temperature. For example, the shape of bubbles formed on apatite under electron beam irradiation at room temperature is spherical while that in high temperature is elongated along *c*-axis. Therefore, the orientation effects might be more significant at high temperature.

Figure 4.7(b) illustrates the difference in fading rate of tracks parallel to *c-axis* and perpendicular to *c*-axis. When the track is perpendicular to *c*-axis, the track radius reduction is more than that in other directions because the vacancies emission from the hollow tracks to the matrix along *c-axis* is faster than other directions. It is known from Equation 4.2 that the amplification factor is inverse proportional to track radius while it is unrelated to the change of track length. Therefore, according to the exponential relation

of decay law as shown in Equation 4.1 and 2, the annealing of tracks perpendicular to *c-axis* is more rapid.

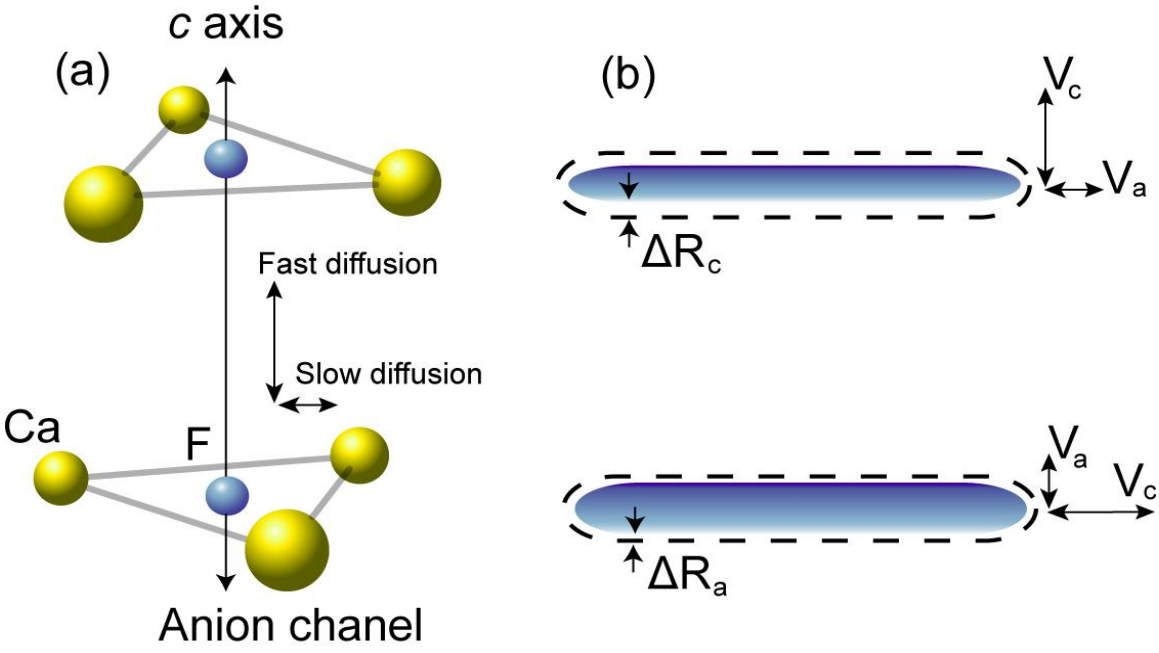

Figure 4.7 Orientation effects in electron beam induced fission track annealing. (a) The anion channel including calcium triangles parallel to the *c-axis* favors diffusion of species (modified after Calderin [26], Gleadow [28]). (b) More vacancies emission (more radius reduction ΔR_c) is therefore expected when tracks perpendicular to *c*-axis, which leads to more rapid track fading (μ_c) according to the decay law.

As is mentioned above, the bubbles are observed to move in crystalline fluorapatite matrix for a long distance under electron beam irradiation at high temperature. This complicated phenomenon can be well understood by our model based on the four mechanisms. The bubbles is formed and enlarged as a result of the decomposition process to supply gaseous phases into voids or tracks. On the other hand, the bubbles can be partially cut off by the radiolytic shrinkage process. If the supply and elimination of bubbles is balanced and there is no orientation effect, a morphological change according to ideal Rayleigh instability can be expected to lower total surface energy. However, when the samples heated in high temperature, the orientation effects take effects under

electron irradiation and cause the tracks to elongate along *c*-axis. When a bubble is preferentially growing and eliminating along one of the two directions along *c*-axis, the motion of the bubble is likely be observed. If each end of a big bubble move in opposite directions along *c-axis* due to the competition of track growth and shrinkage, the big bubble can be broke up into two smaller bubbles.

In conclusion, orientation effects induced by electron irradiation at high temperature have been investigated on the fission tracks and the bubbles in fluorapatite. The motion and elongation of bubbles are driven by the competition of the directional loss and gain of gas-filled cavity. Similarly, the faster diffusivity along *c-axis* causes a rapid reduction of track radius for the track perpendicular to *c*-axis, which in turn expedites the track fading according to the decay law of Rayleigh instability. The similarities of fission tracks and electron induced bubbles in the elongation along *c-axis* under radiolytic annealing at high temperature give a direct physical picture for understanding the crystallographic effect on fission track annealing. The similarities in the morphologies of fission tracks and bubbles also support that the fission tracks are actually empty.

1. R.L. Fleischer, *Fission tracks in solids - production mechanisms and natural origins.* Mater. Sci., 2004. **39**: p. 3901-3911.
2. L. Chadderton, *Nuclear tracks in solids: registration physics and the compound spike.* Radiat. Meas., 2003. **36**: p. 13-34.
3. P.F. Green, I.R. Duddy, G.M. Laslett, K.A. Hegarty, A.J.W. Gleadow and J.F. Lovering, *Thermal annealing of fission tracks in apatite 4. Quantitative modelling techniques and extension to geological timescales.* Chem. Geol., 1989. **79**: p. 155-182.
4. G.M. Laslett, P.F. Green, D. I.R. and G. A.J.W., *Thermal annealing of fission track in apatite, 2. A quantitative analysis.* Chem. Geol., 1987. **65**: p. 1-13.

5. W.D. Carlson, *Mechanisms and kinetics of apatite fission-track annealing.* Am. Mineral., 1990. **75**: p. 1120-1139.
6. R.A. Donelick, *Crystallographic orientation dependence of mean etchable fission track length in apatite: An empirical model and experimental observations.* Am. Mineral., 1991. **76**: p. 83-91.
7. R.A. Donelick, R.A. Ketcham and W.D. Carlson, *Variability of apatite fission-track annealing kinetics: II. Crystallographic orientation effects.* Am. Mineral., 1999. **84**: p. 1224-1234.
8. L.M. Wang and W.J. Weber. *HRTEM study of heavy ion irradiation damage in Ca2La8(SiO4)6O2*. in *51st Annual Meeting of the Microscopy Society of American*. 1993. San Francisco: San Francisco Press.
9. T.A. Paul and P.G. Fitzgerald, *Transmission electron microscopic investigation of fission tracks in fluorapatite.* Am. Mineral., 1992. **77**: p. 336-344.
10. T.A. Paul, *Transmission electron microscopy investigation of unetched fission tracks in fluorapatite-physical process of annealing.* Nucl. Tracks. Radiat. Meas., 1993. **21**: p. 507-511.
11. P.B. Price and R.M. Walker, *Observations of charged-particle tracks in solids.* J. Appl. Phys., 1962. **33**: p. 3400-3406.
12. L.M. Wang, W.X. Li, K. Sun, K.D. Li and R.C. Ewing, *The nature of fission track in fluorapatite: on its structure, formation and annealing behaviors.* To be submitted, 2009.
13. D.E. Alexander and R.C. Birtcher, *The effect of ion irradiation on inert gas bubble mobility.* J. Nucl. Mater., 1992. **191-194**: p. 1289-1294.
14. R.C. Birtcher, S.E. Donnelly, M. Song, K. Furuya, K. Mitsuishi and C.W. Allen, *Behavior of crystalline Xe nanoprecipitates during coalescence.* Phys. Rev. Lett., 1999. **83**: p. 1617.
15. R.C. Birtcher, M.A. Kirk, K. Furuya, G.R. Lumpkin and M.-O. Ruault, *In situ transmission electron microscopy investigation of radiation effects.* J. Mater. Res., 2005. **20**: p. 1654-1683.
16. A. Meldrum, L.M. Wang and R.C. Ewing, *Electron-irradiation-induced phase segregation in crystalline and amorphous apatite: A TEM study.* Am. Mineral., 1997. **82**(9-10): p. 858-869.
17. X. Zhu, *Shrikage of nanocavities in silicon during electron beam irradiaiton.* J. Appl. Phys., 2006. **100**: p. 034304.
18. D.R. Olander, *Fundamental Aspects of Nuclear Reactor Fuel Elements*. 1976, Springfield, Virginia: National Technical Information Service, U.S. Department of Commerce. 236-239, 490-491.
19. X.F. Zhu, J.S. Williams, M.J. Conway, M.C. Ridgway, F. Fortuna, M.O. Ruault and H. Bernas, *Direct observation of irradiation-induced nanocavity shrikage in Si.* Appl. Phys. Lett., 2001. **79**: p. 3416.
20. G. Ouyang, X. Tan, M.Q. Cai and G.W. Yang, *Surface energy and shrinkage of a nanocavity.* Appl. Phys. Lett., 2006. **89**: p. 183104.
21. S.B. Fisher, *On the tempeature rise in electron irradated foils.* Radiation Effects, 1970. **5**: p. 239-243.

22. K.D. Li, H.Y. Xiao and L.M. Wang, *Computer simulation study of defect formation and migration energy in calcium fluoride.* NIM B, 2008. **266**: p. 2698-2701.
23. L.P. Zenser and R. Gruehn, *Decomposition of MgF2 in the transmission electron microscope.* J. Solid State Chem., 2001. **157**: p. 30.
24. F.A. Nichols and W.W. Mullins, *Surface-(interface-) and volume-diffusion contributions to morphological changes driven by capillarity.* Trans. Met. Soc. AIME, 1965. **233**: p. 1840.
25. A.M. Glaeser, *Model studies of Rayleigh instabilities via microdesigned interfaces.* Interface Sci., 2001. **9**: p. 65-82.
26. L. Calderin, M.J. Stott and A. Rubio, *Electronic and crystallographic structure of apatites.* Phys. Rev. B, 2003. **67**: p. 134106.
27. J.M. Hughes, W.D. Carlson and K.D. Crowley, *Crystal structures of natural ternary apatites:Solid solution in the Ca5(PO4)3X system.* Am. Mineral., 1990: p. 295-304.
28. A.J.W. Gleadow, D.X. Belton, B.P. Kohn and R.W. Brown, *Fission track dating of phosphate minerals and the thermochronology of apatite*, in *Reviews in Mineralogy & Geochemistry*, M.J. Kohn, J. Rakovan, and J.M. Huges, Editors. 2002: Washington, DC. p. 579-630.

CHAPTER V

MODELING OF TRACK RADIUS IN FLUORAPATITE

5.1. Background

As shown in previous chapters, the hollow structure and annealing behaviors of fission tracks in fluorapatite have been investigated. The hollow structure of latent tracks is a key to an adequate physical description of fission track annealing in fluorapatite and subsequent modeling of track annealing.

The experimental investigations and modeling approaches will be conducted to clarify the contribution of radiation induced decomposition on the radius of hollow tracks in this research. Much work has been devoted to the interpretation of damage process under heavy ion radiation either by experimental studies using transmission electron microscopy, channeling-Rutherford-backscattering spectrometry, scanning force microscopy and small-angle X-ray (SAXS) [1-7]. The damage structure of tracks depends on target materials. The mass loss due to radiolytic decomposition during the high energy deposition would significantly influence the track structure. Tracks in many oxides and complex ceramics are demonstrated to be amorphous without radiolytic decomposition [5, 8]. The SAXS analysis in SiO_2, without mass loss considered in the

simulation, shows that the plastic deformation during the energy deposition of high energy ion pushes the mass from the core to the surrounding region to form a structure with low density core and high density shell [3]. In comparison, high energy ion irradiation is believed to produce a free volume inside volatile-rich polymers and other volatile rich solids, *e.g.,* CaF_2 and fluorapatite (Ca_{10} $(PO4)_6F_2$) [2, 4, 9-10]. Small angle X-Ray analyses of Pb ion tracks in LiF demonstrate the tracks are low-density porous structure, which is attributed to radiolytic decomposition of the crystal [11]. The irreversible decomposition of volatile rich fluorapatite due to the loss of gaseous atoms might lead to the production of hollow core [2, 11].

On the other hand, the understanding of the relation between track radius and the energy deposition is important to provide information required for a refined physical model of track annealing. It is well known that the data of etched fission tracks have long been mathematically fitted by the mathematical features without any consideration on the physical mechanism of annealing [12-13]. Etched tracks anneal much faster initially from each end of the track and subsequently slower toward center where the fission occurred. The smaller track radius at each end compared to the middle of the track results from the fission fragment decreasing its energy loss per depth unit from the center toward each end [14]. Through TRIM calculation, it is found that the effective track radius induced by fission fragments (with initial energy 50-100 MeV) has an approximate linear relation to $S_e^{1/2}$, the square root of electronic energy loss per depth. The stopping power as a function of target depth can be simply obtained by TRIM simulation [15]. One can calculate the track profile, if knowing the two relations: the $S_e^{1/2}$ relation between

stopping power and target depth, and the relation between stopping power and track radius.

There are two approaches to calculate latent track radius as a function of stopping power by applying thermal spike model. One describes the temperature evolution in the electronic and the atomic system by classical heat conduction while the two systems are coupled by electron-phonon coupling [8]. Using its strength as the only adjustable parameter this model requires considerable numerical computations. Another version bypasses the temperature evolution and concentrates on the late phase of track formation [16-17]. This semi-empirical method needs an experimentally verified correlation between the threshold for track formation and material parameters. In the modeling of the track radius, the temperature rise is assumed to be the only effect under energy deposition from energetic ions. However the decomposition of target material is neglected. In fact, there is an apparent discrepancy on energy consumption that only 10% stopping power is contributed to the temperature rise in the track area in the first version model [18], while 60-80% stopping power is deposited within the cylinder of track radius in the second version [8]. This difference in the energy consumption indicates a need for considering possible destination of energy deposition other than temperature rise.

In this chapter, the track radii near target surface created by various swift ions in fluorapatite are measured on TEM cross sectional images. A modified thermal spike model is applied to calculate the track radii of different ions in fluorapatite. The new approach of this calculation is to include the contribution of radiation induced-

decomposition into the production of the hollow track in volatile-rich fluorapatite. Similar to the second version model, only the dependence of final track radius on the stopping power is considered therefore the calculation of the thermal conduction and the recovery can be avoided. However, the electronic stopping power is divided into the nonproductive part and the productive part in our model. The former represents all the energy dissipated outside the final track radius, and the latter includes energy consumption not only in the temperature rise but also in the decomposition process within the final track radius. The calculation shows that the amount of energy consumed in the decomposition is significantly larger than that for temperature rise. Therefore it cannot be neglected in volatile rich target.

5.2. Track diameter near sample surface

Parallel tracks have been created by various swift ions along the [0001] direction of fluorapatite minerals from Durango. Cross section samples have been made to measure the track radius near the incident surface under TEM. Powder samples were prepared for HRTEM image of tracks passing through the whole sample thickness. HRTEM image shows that the 2.2 GeV Au ions irradiated tracks in fluorapatite are hollow, which suggests significant mass loss as a result of radiolytic decomposition of the volatile-rich material (Figure 5.1a). In comparison, no significant mass loss occurs within the core region of amorphous track in zircon, as shown in Figure 5.1b [19].

The energy of swift ions decreases gradually as the ions penetrating into target materials due to the energy loss. The electronic stopping power varies with the trajectory depth since it depends on both the energy of incident ions and the target materials (Figure 5.2). The most ideal way to experimentally investigate the track diameter as a function of stopping power is to prepare a cross section sample which shows the track diameter throughout the entire trajectory depth. However, it would be very difficult to prepare such a cross section sample due to the very thin nature of a TEM sample. It should be mentioned that the relation between track radius and stopping power has always been investigated under TEM by using crushed powder samples or plane view samples due to the difficulty in the preparation of cross section sample. However, as shown in Figure 5.2, the assumption that track radius does not change much with different stopping power is not correct.

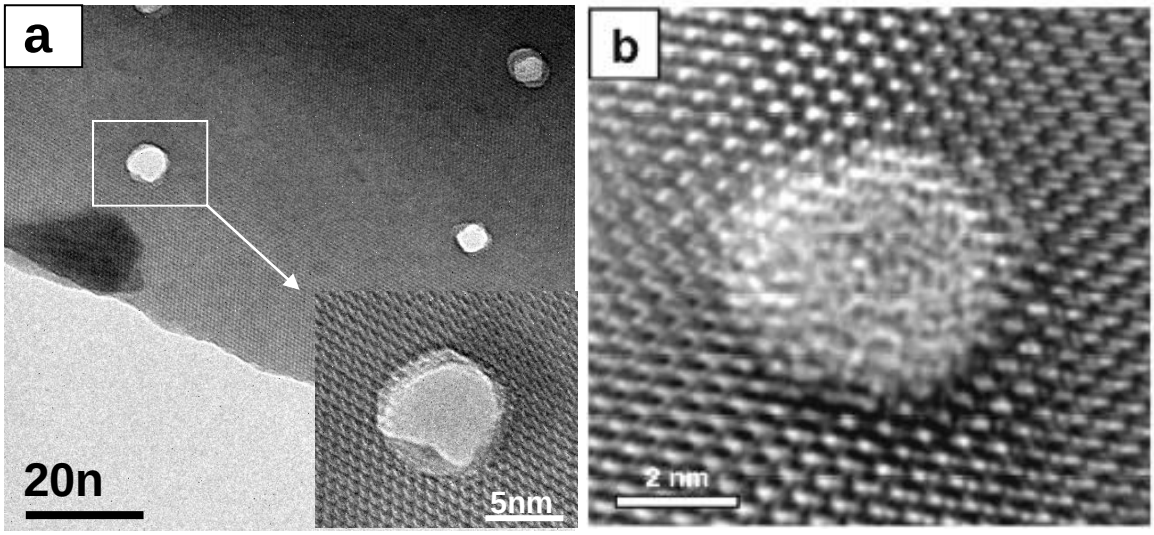

Figure 5.1 A comparison of hollow tracks (**a**) irradiated 2.2 GeV Au ions in fluorapatite and amorphous tracks (**b**) irradiated by 10 GeV Pb in zircon(From Lang *et al.* in [19]). The irreversible decomposition of volatile rich fluorapatite and subsequent mass loss during the energetic ion deposition causes the hollow track.

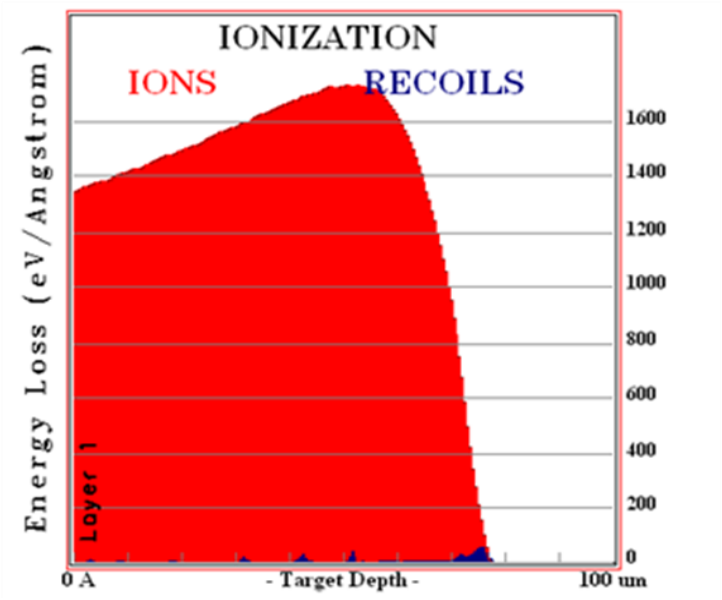

Figure 5.2 The SRIM simulation shows that the stopping power of 1.1 GeV Ru ions irradiated in fluorapatite, mainly contributed by electronic part, varies with the target depth.

In order to explore the dependence of track radius on stopping power, samples in cross section have been prepared to measure the track diameters near sample surface (x = 0), where the stopping power can be conveniently obtained by TRIM calculation [15]. Figure 5.3 shows parallel tracks of 710 MeV Bi bombarded apatite near surface (x = 0). The arrow shows the entering of ions. The cross section image indicates that the tracks near entering surface have little variation in diameter. The track diameters induced by different swift ions have been measured for first time using TEM cross section samples. The average track diameters near sample surface are plotted as a dependence with

corresponding stopping power for 710 MeV Bi, 2.2 GeV Au, 1.43 GeV Xe, 130 MeV Xe, 1.1 GeV Ru and 50 MeV Xe ions radiated fluorapatite, respectively(Figure 5.4). The measured track diameter decreases as the decreasing stopping power. The fitting of the experimental data based on a new decomposition model will be discussed in the next section.

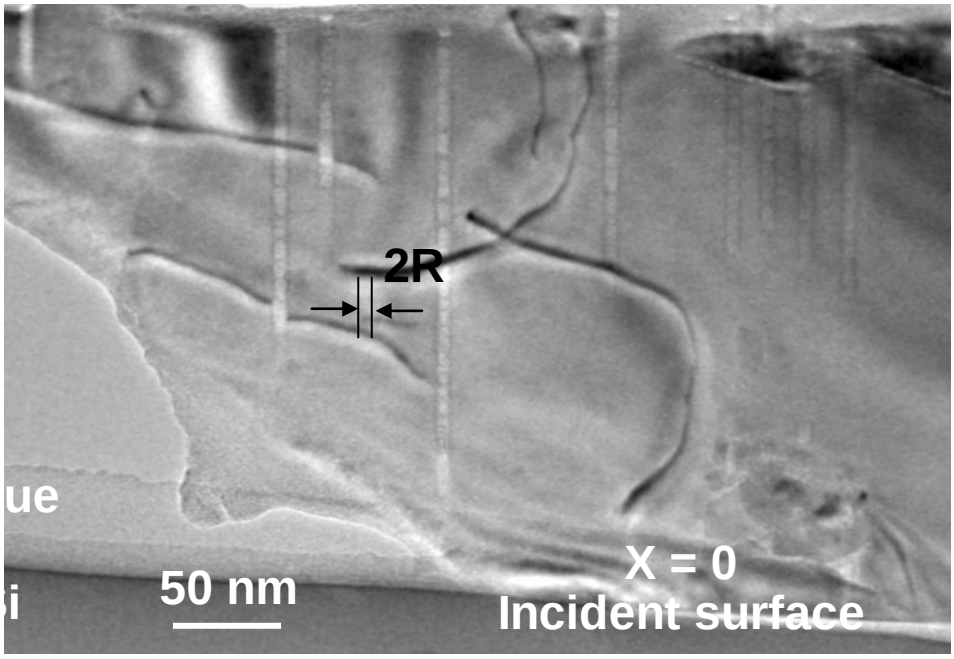

Figure 5.3 Cross section view of the tracks (near incident surface) created by710 MeV Bi ions irradiation in apatite.

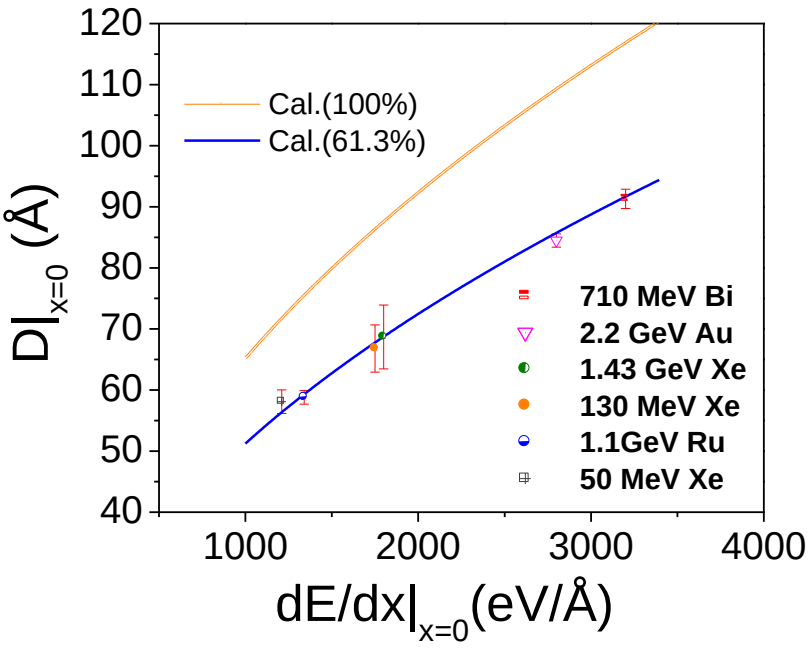

Figure 5.4 Dependence of track diameter on stopping power of various swift ions near entering surface (x=0). The data were fitted by the decomposition model with productive efficiency of 61.3%.

5.3. Calculation

5.3.1. Method

Track diameter as a function of stopping power has been calculated by a modified thermal spike model, which considers the contribution of radiation induced decomposition to the track morphology. As shown in Figure 5.5, the portion of the electronic stopping power S_e (or $-(dE/dx)_e$) deposited within track radius of r is defined as the productive stopping power, which is responsible for the production of damage track within the track radius. The nonproductive stopping power NS_e is the rest of

stopping power which is wasted outside track radius. The productive stopping power is used in two parts: TS_e for the temperature rise within r, and DS_e for the decomposition within track radius. Therefore, the efficiency of damaging power is $\eta = T + D = 1 - N$.

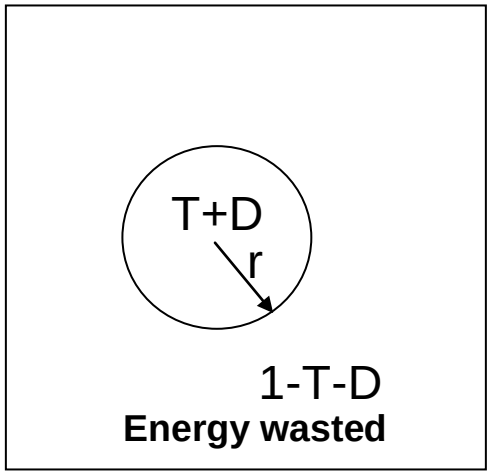

Figure 5.5 Electronic stopping power is used for the temperature rise (*T*) or the decomposition (*D*) of the target materials within the track radius, or wasted outside the track radius.

Since the core is very small (around several nm in radius) and in hot liquid state, the temperature rise ΔT is assumed to be homogenous within track radius. During the track production process,

$$\eta S_e = C_p \Delta T \frac{\pi r^2 .1}{N_A v} + (-\Delta H_f \frac{\pi r^2 .1}{N_A v}), \tag{5.1}$$

where v is unit volume [23], C_p heat capacity [24], N_A Avogadro's constant and $\Delta T = T_m - T_0$ where T_m melting temperature and T_0 room temperature.

The decomposition energy ($-\Delta H_f$) is taken from the formation energy at room temperature [23-24] in order to make sure that there is no overlap between temperature rise and decomposition. For the convenience of calculation, it is assumed that a portion of stopping power is first consumed for the decomposition of fluroapatite into four elements (*i.e.*, O_2, F_2, Ca, and P) at room temperature. Another portion is then used to raise the temperature of the four elements from room temperature to melting temperature. In this way, the heat capacity C_p can be estimated by:

$$C_p = \frac{\sum_{i=1}^{4} \int_{T_0}^{T_m} m_i C_p^i dT}{\int_{T_0}^{T_m} dT}. \qquad (5.2a)$$

Among them, m_i is the molecular factor of each element, that is, O_2:F_2:Ca: P=6:0.5:3:5; C_p^i is the heat capacity of each element. The value of heat capacity up to melting temperature is obtained by extrapolating the curve of heat capacity as a function of temperature up to 1500 K in the CRC Handbook [25]. The modified heat capacity based on Equation 2a is 94.27 cal/mol.K. Since the energy is used in breaking bonds, the value from the combined molecules is much lower than that of single crystal fluorapatite, 159.84 cal/mol.K. The latter can be obtained from the equation to estimate heat capacity of fluorapatite by:

$$C_p = 159.84 - 10.83T^{-1/2} - 17.838T^{-3}. \qquad (5.2b)$$

Table 5.1 The physical parameters for fluorapatite.

Parameters	Value
Unit volume($Å^3$/mole)	261.54 [23]
Formation energy(kcal/mol)	1630.787 [23]
Melting temperature(K)	1923
Heat capacity(cal/mol.k)	159.84 [24]
Density (g/cm^3)	3.12

The energy used for temperature rise or lattice vibration is the kinetic energy, while that for breaking up the bonds into elements is mainly potential energy. Therefore, the ratio of T/D is calculated as 0.094 by using the data in Table 1. This means most of the productive energy deposition is used to the decomposition of target fluorapatite.

5.3.2. Calculation of swift ion tracks

The two fitting lines in the Figure 5.4 show the modeling result of the track diameter as a function of stopping power of various swift ions near entering surface (x=0). The stopping power S_e at x = 0 is calculated by TRIM [15]. The S_e^{th}, a threshold below which no track is produced, is not considered in this calculation because the stopping power near entering surface for all the incident ions are always significantly higher than

corresponding threshold. If the efficiency of damaging power is 100% (η =1), the calculated curve (the yellow line) is higher than the values of experimental data. However, the experimental data can be fitted by the calculated curve (green line) with a productive efficiency of 61.3%. Based on the T/D ratio, then the fraction of stopping power for temperature rise can be obtained as T = 5.27%, that for the decomposition D = 56.03%, and that for the wasted energy N = 38.7%. They are consistent with the results in Szenes model as mentioned above: about 10% of the electronic energy is transferred to for temperature rise [18], and those in Meftah experiments, about 66% the energy is deposited within the track radius [5]. The 50~60% energy difference between the total energy and the energy used in temperature rise is highly possibly used in the radiation induced decomposition of volatile-rich fluorapatite.

5.3.3. Fission track profile

In the following, the track radius profile created by two fission fragments of neutron induced ^{235}U has been simulated by using the efficiency (61.3%) obtained above. The kinetic energy of fission fragments is ~ 170 MeV for neutron induced ^{235}U nuclear fission. One typical nuclear reaction is,

$$^{235}_{92}\mathrm{U} + {}^{1}_{0}\mathrm{n} \rightarrow {}^{134}_{54}\mathrm{Xe} + {}^{100}_{38}\mathrm{Sr} + 2\,{}^{1}_{0}\mathrm{n}. \qquad (5.3)$$

For heavy ion with high energy (10 ~100 MeV) the energy loss is mainly the electronic contribution, which has an approximate $E^{1/2}$ dependence,

$$-\frac{dE}{dx} = KE^{1/2}, \tag{5.4}$$

where K is a constant with a unit of eV/ Å$^{1/2}$. Change the variable $E^{1/2}$ to target depth x by integrating Equation 5.4 and obtain a linear equation:

$$-\frac{dE}{dx} = KE_0^{1/2} - \frac{K^2 x}{2}, \tag{5.5}$$

where E_0 is the initial energy for fission fragments. At first, the curve of stopping power as a function of target depth is calculated by TRIM code. The curve of stopping power as a function of target depth can be well fitted by the linear relation as shown in Equation 5.5. The calculated parameters for fission fragments Sr and Xe are shown in Table 5.2.

Knowing the efficiency of stopping power 61.3%, the profile of fission track in fluorapatite can be obtained,

$$r = [\eta(KE_0^{1/2} - \frac{K^2 x}{2})\frac{N_A v}{\pi(C_p \Delta T - \Delta H_f)}]^{1/2}. \tag{5.6}$$

$$-\frac{dE}{dx} = 1310 - \frac{0.1678^2}{2}x \qquad x \text{ in Å}$$

$$-\frac{dE}{dx} = 1470 - \frac{0.1724^2}{2}x$$

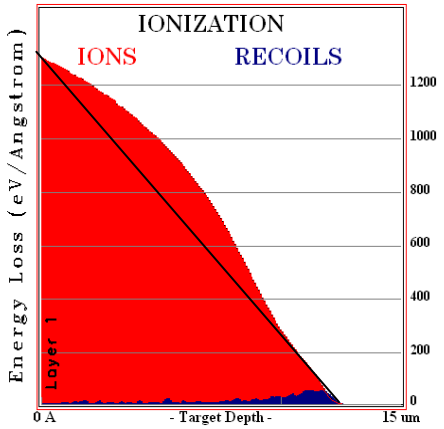

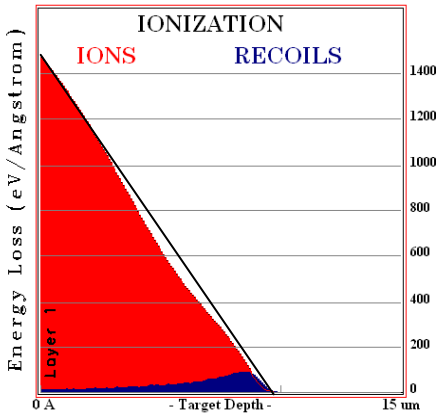

97.35 MeV Sr

72.65 MeV Xe

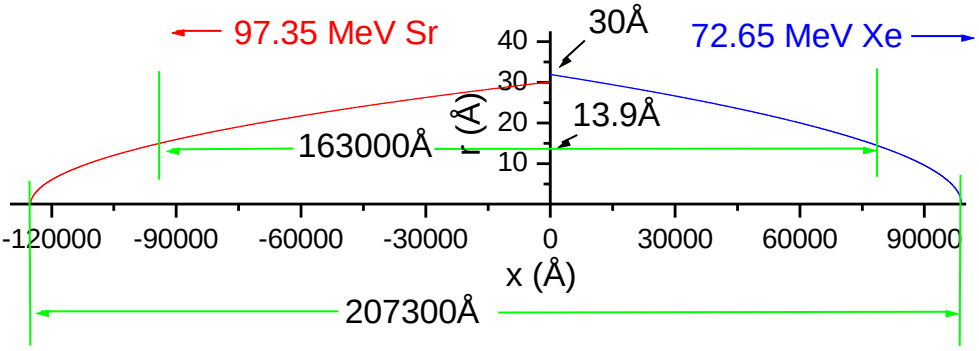

Figure 5.6 Fission track profile created by two fission fragments, Sr and Xe in opposite directions. The top shows the SRIM simulated stopping power as a function of target depth for fission fragments Sr and Xe, which have an approximate $E^{1/2}$ dependence. The total length/depth of the damaged trail is 20.7 μm. The etchable length is around 16.3 μm, which means the track radius smaller than 13.9 Å is inefficient to be etched.

Table 5.2 The parameters for the calculation of radii of tracks induced by a pair of fission fragments Sr and Xe in fluroapatite.

Parameters	$^{100}_{38}Sr$	$^{134}_{54}Xe$
E_0(MeV)	97.35	72.5
Range(μm)	12.5	9.90
S_e(x=0)(eV/ Å)	1310	1470
K ($eV^{1/2}$/ Å)	0.1448	0.1724
Radius(x=0) (Å)	28.5	30.1

Figure 5.6 shows the track radius profile along the target depth created by neutron induced ^{235}U fission fragments of 97.35 MeV Sr and 72.65 MeV Xe in opposite directions. The track radius r at the fission point (x = 0) is calculated as 28.5 Å for Sr and 30.1 Å for Xe, respectively. The difference of the two radii is 1.6 Å. Therefore, it is not expected to find a specific point where fission was taking place showing two tracks with significantly different radii under TEM. In addition, the total track depth (about 20.7 μm) is 4~5 orders bigger than the change of track radius. This explains the little change of track radius along its trajectory under TEM observations. The average length of etched tracks measured by optical microscope is around 16.3 μm, much shorter than that of unetched tracks. The difference in these two lengths can be explained by the track etchability when the track radius is smaller than a critical value, the track is inefficient to be etched [5]. As shown in Figure 5. 4, a line was drawn parallel to X-axis, cutting with

the track profile in two points in each end, and with the Y-axis in the middle. When the distance of the two points are 16.3 μm, one can obtain the critical value of minimal track radius for etchability is around 14 Å(*i.e.*, the intersection point with Y-axis), which is close 18 Å given by Meftah *et al.* [5].

In conclusion, irreversible decomposition of volatile-rich fluorapatite during highly energetic ion deposition is essential to create the hollow track core. Cross section samples irradiated by various ions and energies are made to measure the different track radii near the surface under TEM. The decomposition spike model has been explored to investigate track radius dependence on electronic stopping power, which can be readily used in other volatile-rich materials such as LiF, CaF_2 and polymers. However, it is highly necessary to prepare cross section samples showing the whole length of swift ion radiated tracks (up to 10~20 μm in apatite) for experimental measurements of track profile under TEM. The fission track profile obtained by the model is highly useful for the modeling of track annealing at atomic level.

1. T.A. Paul and P.G. Fitzgerald, *Transmission electron-microscopic investigation of fission tracks in fluorapatite.* Am. Mineral., 1992. **77**: p. 336-344.
2. S.A. Saleh and Y. Eyala, *Porous tracks along wakes of swift uranium ions in polyimide.* Appl. Phys. Lett., 2004. **85**: p. 2529.
3. P. Kluth, C.S. Schnohr, O.H. Pakarinen, F. Djurabekova, D.J. Sprouster, R. Giulian, M.C. Ridgway, A.P. Byrne, C. Trautmann, D.J. Cookson, K. Nordlund and M. Toulemonde, *Fine Structure in Swift Heavy Ion Tracks in Amorphous SiO2*. Phys. Rev. Lett., 2008. **101**: p. 175503.

4. G. Jaskierowicz, A. Dunlop and R. Jonckheere, *Track formation in fluorapatite irradiated with energetic cluster ions.* Nucl. Instrum. Methods Phys. Res., Sect. B, 2004. **222**: p. 213-227.
5. A. Meftah, F. Brisard, J.M. Costantini, M. Hage-Ali, J.P. Stoquert, F. Studer and M. Toulemonde, *Swift heavy ions in magnetic insulators: A damage cross section velocity effect.* Phys. Rev. B, 1993. **48**: p. 920.
6. R.M. Papaleo, R. Leal, C. Trautmann and E.M. Bringa, *Cratering by MeV-GeV ions as a function of angle of incidence.* NIM B, 2003. **206**: p. 7-12.
7. A. Adla, H. Fuess and C. Trautmann, *Characterization of heavy ion tracks in Polymers by Transmission Electron Microscopy.* J. Polymer Science, 2003. **41**: p. 2892.
8. A. Meftah, F. Brisard, J.M. Costantini, E. Dooryhee, M. Hage-Ali, M. Hervieu, J.P. Stoquert, F. Studer and M. Toulemonde, *Track formation in SiO2 quartz and the thermal-spike mechanism.* Phys. Rev. B, 1994. **49**: p. 12457.
9. Y. Eyal and K. Gassan, *Observation of latent heavy-ion tracks in polyimide by means of transmission electron microscopy.* Nucl. Instrum. Methods Phys. Res., Sect. B, 1999. **156**: p. 183-190.
10. J. Jensen, A. Dunlop and S. Della-Negra, *Tracks induced in CaF_2 by MeV cluster irradiation.* Nucl. Instrum. Methods Phys. Res., Sect. B, 1998. **141**: p. 753-762.
11. S.A. Saleh and Y. Eyal, *Porous track cores along wakes of swift Pb ions in LiF.* NIM B, 2005. **230**: p. 246-250.
12. P.F. Green, I.R. Duddy, A.J.W. Gleadow, T. P.R. and G.M. Laslett, *Thermal annealing of fission track in apatite, 1. A qualitative description.* Chem. Geol., 1986. **59**: p. 237-328.
13. W.D. Carlson, *Mechanisms and kinetics of apatite fission-track annealing.* Am. Mineral., 1990. **75**: p. 1120-1139.
14. P.F. Green, I.R. Duddy and G.M. Laslett, *Can fission track annealing in apatite be described by first-order kinetics?* Earth and Planetary Science letters, 1988. **87**: p. 216-228.
15. SRIM, *http://www.srim.org/SRIM/SRIM2006.htm*. 2006.
16. G. Szenes, *Analysis of tracks induced by cluster ions in CaF2.* Phys. Rev. B, 2000: p. 14267.
17. G. Szenes, *General features of latent track formation in magnetic insulators irradiated with swift heavy ions.* Phys. Rev. B, 1995. **51**: p. 8026.
18. G. Szenes, *A possible mechanism of formation of radiation defects in amorphous metals bombarded with high-energy heavy-ions.* Materials Science Forum, 1992. **97**: p. 647-652.
19. M. Lang, J. Lian, F.X. Zhang, B.W.H. Hendriks, C. Trautmann, R. Neumann and R.C. Ewing, *Fission tracks simulated by swift heavy ions at crustal pressures and temperatures* Earth and planetary science letters, 2008 **274**: p. 355-358.
20. T.A. Paul, *Transmission electron microscopy investigation of unetched fission tracks in fluorapatite-physical process of annealing.* Nucl. Tracks. Radiat. Meas., 1993. **21**: p. 507-511.
21. T.A. Paul and P.G. Fitzgerald, *Transmission electron microscopic investigation of fission tracks in fluorapatite.* Am. Mineral., 1992. **77**: p. 336-344.

22. S. Miro, D. Grebille, D. Chateigner, D. Pelloquin, J.P. Stoquert, J.J. Grob, J.M. Costantini and F. Studer, *X-ray diffraction study of damage induced by swift heavy ion irradiation in fluorapatite.* Nucl. Instrum. Methods Phys. Res., Sect. B, 2005. **227**: p. 306-318.
23. J.L. Fleche, *Thermodynamical functions for crystals with large unit cells such as zircon, coffinite, fluorapatite, and iodoapatite from ab initio calculations.* Phys. Rev. B, 2002. **65**: p. 245116.
24. C. Zhu and D.A. Sverjensky, *Partitioning of F-Cl-OH between minerals and hydrothermal fluids.* Geochim. Cosmochim. Acta, 1991. **55**: p. 1837.
25. D.R. Lide, *Thermochemistry, Electrochemistry, and Kinetics*, in *CRC Hand Book of Chemistry and Physics*. 2005, Taylor &Francis Group. p. 5-5.

CHAPTER VI

SUMMARY AND FUTURE WORK

6.1. Summary

The hollow nature of fission tracks has been confirmed by several lines of independent evidence. At high temperature, copper atoms from the TEM grid diffuse into hollow fission tracks through the open ends and form nanorods inside the tracks. The EELS thickness map of a through-thickness fission track shows the thickness signal of the fission track is as low as the background of the sample, indicating the fission track is hollow. The high resolution TEM images of 2.2 GeV Au ions irradiated tracks in fluorapatite clearly show that the core region is hollow without solid components within the core. The Airy pattern in FFT image resulting from circular aperture diffraction from a region centered in a track further confirms the hollow nature of the track.

In-situ and *ex-situ* thermal annealing of latent fission tracks in fluorapatite have been performed over a range of temperatures. The data clearly show that track annealing is a complex process with several underlying mechanisms. The hollow structure of latent tracks is key to providing an adequate physical description for fission track "fading" in fluorapatite at elevated temperatures. The damage recovery in a track is driven by Rayleigh instability and Brownian motion of empty (or gas-filled) segments, in addition

to the shrinkage of hollow tracks due to thermal emission of vacancies into the surrounding solid. This is significantly different from the annealing behaviors of amorphous tracks in zircon; the amorphous tracks became gradually fading and eventually disappeared without fragmentation. Based on micro-scale studies on chemically etched-tracks, it is generally assumed that fission tracks would completely anneal and disappear at ~360 ℃ within one hour. This is clearly not the case, as demonstrated by nanoscale observations of the annealing of latent fission tracks. Remnants of the tracks, in the form of isolated segments, are still present at 700 ℃ for annealing times in excess of 130 minutes. This suggests that the discontinuity of fission tracks due to thermal induced diffusion impedes the etching agent from reaching the other sections of hollow tracks with continued etching, thereby significantly reducing the effectiveness of chemical etching.

The electron-induced irradiation effects on morphological change of bubbles and fission tracks have been investigated by TEM. The fission tracks that have not annealed at 700 ^{o}C after 10 hours rapidly anneal under continuous electron beam exposure at 700 ^{o}C. However, the annealing of the track that is almost perpendicular to *c*-axis is significantly faster than that of a track nearly parallel to the *c*-axis. The growth, coalescence, motion and elongation along the *c*-axis of the electron irradiation induced bubbles have been observed *in situ* in fluorapatite at 700 ^{o}C. This study suggests that the combined influences of electron irradiation induced track shrinkage, decomposition, morphological change and orientation effects of the hexagonal apatite at high temperature attribute to the anisotropic behaviors of bubbles and fission tracks. The similarities of

electron-beam-induced bubbles and fission tracks in the stationary and dynamic characteristics provide additional evidence of the hollow nature of fission tracks in fluorapatite.

Irreversible decomposition of volatile-rich fluorapatite during the intense energy deposition is essential to creating the hollow tracks. Cross-section samples irradiated by various ions and energies have been used to measure the different track radii near the surface using TEM. The decomposition spike model has been explored to investigate track radius dependence on electronic stopping power, which can be readily used in other volatile-rich materials such as LiF, CaF_2 and polymers. The track anneals faster near each end than that in the middle where the fission occurred, because the track radius decreases from the middle to each end along the track. Therefore, the fission track profile obtained by the model should be useful for future physical modeling of track shortening at atomic level.

6.2. Future work

Intense work has long been focused on mathematically modeling the etched length of track annealing and applying these models to unraveling the thermal history of Earth' crust. However, very few physical models are available due to lack of atomic level investigation of fission tracks. This research reveals that many previous assumptions about track structure and annealing mechanisms are, in fact, not true. Fission tracks in

fluorapatite are hollow, but not amorphous as usually assumed. The shrinkage of the hollow fission track is not the result of defect elimination, but rather from thermal emission of vacancies from the track to the solid. The differences in the internal structure and its influence on the annealing behaviors between amorphous tracks in zircon and hollow tracks in fluorapatite have not been realized and studied before. All of these demonstrate the atomic level method is a very promising way to investigate the structure, annealing mechanisms and even track formation mechanisms. There are still many fundamental questions on the fission track to be addressed in the future research.

In order to confirm influence of the mass loss on the formation of hollow track, I would propose to measure the mass loss of thin sample (50~100 μm) of different target materials (zircon and fluorapatite) before and after creating through-thickness tracks by swift ion irradiation. EDS analysis has been performed to simulate the decomposition of volatile rich materials during track formation process by focusing electron beam on single crystal fluorapatite. Through the HAADF Z contrast analysis, it is demonstrated the mass loss within the track core based on the darker contrast from the core region. However, the speculation of the decomposition induced hollow track has not confirmed yet. The formation mechanisms in different materials (*e.g.* fluorapatite and zircon), especially the influence of mass loss on the formation of hollow tracks, are still unknown. The HRTEM images of swift ion tracks in apatite in this research clearly show the hollow nature, however, one might argue that the individual hollow tracks observed by HRTEM do not represent well all the tracks in the sample. Different from the individual tracks, the mass

loss measurements is able to provide overall pictures of track structure and the influence of decomposition on the structure.

I would propose to investigate *in situ* thermal annealing behaviors of amorphous tracks in high resolution mode in TEM heating holder, which will provide direct pictures of defect elimination for future physical modeling of track annealing. *In situ* thermal annealing experiments of both hollow tracks in fluorapatite and amorphous tracks in fluorapatite have been conducted at nano-scale level in this research. At high temperatures, fission tracks in fluorapatite are found to fragment into droplets along their trajectory. This is significantly different from the thermal annealing behaviors of amorphous tracks in zircon; amorphous tracks become fading and disappear gradually. However, the information of the defect distribution radically before annealing and the physical process of defect elimination during annealing are two critical factors to be known for the atomic level simulation of amorphous tracks. It would be convenient to investigate those in TEM high resolution mode in TEM heating holder.

I would also propose to carry out TEM investigations of the connections between track annealing and track formation. On the side on track annealing, the etched length measurements of tracks have demonstrated a faster track reduction for the tracks perpendicular to *c*-axis. The faster annealing in this direction has also been first observed in the *in situ* thermal annealing of hollow tracks at 700 ^{o}C in this research at nanoscale level. The preferentially diffusion of atoms along the open channel along *c*-axis results in the rapid reduction of tracks radius and subsequently faster annealing for the tracks

perpendicular to *c*-axis. On the other side on track formation, the energy deposition of fission fragments produces larger tracks (~9 nm) along *c*-axis, and smaller tracks (~5 nm) perpendicular to *c*-axis. During the track formation, the temperature with the core is estimated to be several thousand degrees. The materials within the track first turn into hot vapor and subsequently quench by cooling wave. It should be noted that the quenching process in the track formation is very similar to the thermal annealing process despite of at a much lower temperature and much longer time in the later case. It is speculated that a more rapid annealing in the direction perpendicular to *c*-axis might result in the smaller track size found in this direction during the fission track formation process. However, more experimental and theoretical efforts are needed to confirm this speculation. For example, cross section samples can be made to measure the radii of tracks irradiated by fission fragments (70~100 MeV) along different crystalline directions.

With improved understanding of track structure and physical mechanisms of annealing behaviors at atomic level, it will be possible to develop models that describe the shortening of etched tracks, rather than using simple mathematical fits to data sets. We have mentioned previously that the track anneals faster near its ends than that in the middle where the fission occurred due to the gradual decrease of track radius along the trajectory of two fission fragments. Therefore, we might figure out the track length shortening (dL/dt) dependence on temperature and time once the fission track profile ($L \propto R$) has been obtained, providing the annealing shrinkage can be described by simple equations ($dR/dt \propto R$). At this stage, I propose to model the annealing behavior of amorphous tracks at first due to much simpler annealing mechanisms than that of

hollow tracks. However, we should conduct experiments to obtain the track radius dependence of stopping power of amorphous tracks, say in zircon, and correspondingly the fission track profile in zircon.